A study on flight muscle system in coleoptera and fuel cell catalyst toward self-powered biological flapping machine

Vo Doan, Tat Thang

2016

A STUDY ON FLIGHT MUSCLE SYSTEM IN COLEOPTERA AND FUEL CELL CATALYST TOWARD SELF-POWERED BIOLOGICAL FLAPPING MACHINE

VO DOAN TAT THANG

SCHOOL OF MECHANICAL AND AEROSPACE ENGINEERING

A thesis submitted to the Nanyang Technological University
in partial fulfilment of the requirements for the degree of
Doctor of Philosophy

2016

Abstract

Miniature wireless device that has the capability of extracellular recording and electrical stimulation enables us to validate the hypothesis of insect maneuver in free flight. Such behavior might be different from what we had experienced for long time in tethered condition. In addition, it would allow solving the difficulty of defining the role of the small muscles in flight. In this report, the function of 3rd axillary sclerite (3Ax) muscle and subalar muscle in coleopteran will be evaluated to achieve the graded turn and braking control in free-flying insect. The coleopteran 3Ax muscle, which is thought to have the function of folding the wing, in fact, plays a key function in steering during flight. The electrical stimulation of 3Ax muscle in free-flying insect is able to induce the graded ipsilateral turns that was also confirmed in tethered condition. Along with 3Ax muscle, the subalar muscle is an important muscle that pulls the posterior part of the wing base to regulate the wing rotation during flight. The electrical stimulation of the muscle caused the increment of wing rotation angle and thus leaded to the increase in drag in free flight. A biological flapping machine can be developed by controlling these muscles in the living insect. Toward self-powering feature, fuel cell can be used as a secondary power source to charge the battery of the electronic board mounted on the living insect. The fuel cell performance can be improved by using electrocatalyst to increase the activity of the cathode. The B-doped Pd (Pd-B) nanoparticle catalyst was synthesized for the cathode by the remarkably facile stepwise electroless deposition method. The Pd-B nanoparticles exhibit superior catalytic activity to the synthesized pure Pd and the commercial Pd/C.

Acknowledgement

Table of Contents

Figure List

Table List

Abbreviation List

Abbreviation	Description
MAV	Micro air vehicle
DARPA	United States Defense Advanced Research Projects Agency
MEMS	Microelectromechanical Systems
WFM	Wing folding muscle
3Ax	Third axillary sclerite
DVM	Dorso-ventral muscle
DLM	Dorsal longitudinal muscle
BSM	Basalar muscle
SBM	Subalar muscle
REM	Remotor extensoris muscle
EMG	Electromyography
GINA	Guidance and inertial navigation assistant
PCB	Printed circuit board
ADC	Analog to digital converter
LED	Light emitting diode
RF	Radio frequency
SP	Mean stroke plane
F_l	Lateral force
F_h	Horizontal force
F_v	Vertical force
F_t	Total force
a_l	Lateral acceleration
a_h	Horizontal acceleration
a_v	Vertical acceleration
a_x	Acceleration in x direction
a_y	Acceleration in y direction
a_z	Acceleration in z direction
fps	Frames per second

ORR	Oxygen reduction reaction
PEMFC	Proton exchange membrane fuel cell
Pt	Platinum
Pd	Palladium
Pt/C	Platinum loaded carbon
Pd/C	Palladium loaded carbon
FESEM	Field electron microscopy
XRD	X-ray diffraction
XPS	X-ray
GC	Glassy carbon
RDE	Rotating disk electrode
AFC	Alkaline fuel cell
PAFC	Phosphoric acid fuel cell
MCFC	Molten carbonate fuel cell
SOFC	Solid oxide fuel cell
HOR	Hydrogen oxidation reaction
H_2O_2	Hydrogen peroxide
i_k	Kinetic current
i_d	Diffusion limit current
i_s	Kinetic current normalized by ECSA
i_m	Kinetic current normalized by catalyst load
K-L plot	Koutecky-Levich plot
ECSA	Electrochemically active surface area
DMAB	Dimethylaminoborane
N_2H_4	Hydrazine hydrate
$PdCl_2$	Palladium chloride
Pd-B	Palladium nanoparticles synthesized with DMAB
Pd-N_2H_4	Palladium nanoparticles synthesize with N2H4
LSV	Linear sweep voltammetry
CV	Cyclic voltammetry
j	Current density
E	Potential

Chapter 1 : Introduction

1.1 Micro Air Vehicle and Flying Insect-machine Hybrid System

The micro air vehicle (MAV) was initially described by the United States Defense Advanced Research Projects Agency (DARPA). Such device was aimed to have a mass less than 100 g with the maximum constrained size of 15 cm. MAVs are expected to be used for exploring the hazardous environment, search and rescue mission, as well as agriculture assisting [1-3]. Fixed and rotary-wing MAVs were shown to have an advantage over other types of MAVs due to the long term development of the traditional flying machine. However, scaling down the size led to the high mass fraction of the propulsion system that extremely reduced its payload capability. The study of biological fliers such as small bird and insect showed that the performance of these MAVs is much lower than that of those natural flyers in term of stability, maneuverability and the efficiency[4, 5]. The idea of mimicking the flapping motion of insects and birds to develop new type of MAV was then reconsidered as key figure for developing MAV. The first successfully free flight of the flapping wing MAV powered by battery called "Microbat" was introduced in 2000 by the researchers from Caltech and Aerovironment [6]. In 2002, James Delaurier and his students, from University of Toronto, developed the first radio control flapping MAV that was able to hover [1]. Robert J. Wood's team demonstrated the first take-off of "RoboBee" in 2007 and recently its hover and lateral flight maneuvers were introduced in tethered condition [5, 7, 8]. These achievements would lead to the promising development of the biological inspired flying machine at insect scale. Nevertheless, the high load of the power supply unit and the complex fabricating process are still the challengeable.

The idea of the insect-machine hybrid system, also known as insect-machine hybrid system, came out when the biologists attached the tiny electronic devices onto the insect

from the early of 90s for measuring the muscles potential of the insect in free flight [9, 10]. The development of the electronic technology enabled certain approaches for stimulating the insect in untethered condition in the recent decade. It makes the insect itself a promising candidate for controllable living MAV [11, 12]. While researchers are trying to develop machines that mimic the insect locomotion, insects themselves are already perfect for such task ask they are natural flyers, walker and even swimmer. Moreover, the insect-machine hybrid system does not required power for flapping but just the control signal to certain steering muscles that would reduce lot of weight of the power supply unit. For the reasons mentioned, insects can be considered for developing an ultra-low power MAV that has a perfect flight maneuver.

Despite its low power consumption, the current trademark batteries are not able to keep the insect-machine hybrid system operating for more than 15 minutes continuously and the battery needs to be charged manually and frequently. Alternatively, the rising of fuel cell has drawn promising advancements in replacing the current commercial battery or adding a secondary backup for charging the battery automatically. The fuel cell can be compact and portable that would be suitable for the beetle to carry. Moreover, the fuel cell can use glucose as fuel that would be an interesting advantage as the fuel can be extracted from insect liquid directly.

1.2 Motivation

Flying insect-machine hybrid system was mostly developed on moths and beetles in flight because of their size and loading capability for carrying the electronics devices. In this thesis, the insect-machine hybrid system uses beetle as the platform since beetle showed more advantage in loading capability and life cycle. While beetle can carry

about 30% of its weight and lasts for more than 3 months in mature stage, the moth can just survive for a few weeks and cannot carry heavy load [11, 12]. Insect flight maneuver is complicated as it involves in the activation of nerve system and multiple muscles with lots of unknown parameters. The stimulation of nerve system is too complex since it's hard to access the flight muscle nerve as well as to implant the electrodes. Meanwhile, the stimulation of flight muscles is much easier because all the muscles are approachable. However, flying insect-machine hybrid system is getting more and more intricate; it is not just initiation/cessation of flight or makes the beetle turn. It now requires very precise protocol in term of targeting of actuator and stimulation parameters that not only control beetle locomotion but also ensure no neuromuscular deficit occurs. The stimulation of target muscle might affect the nearby muscles and deficit of nerve or muscles that would violate the flight control and lead to unpredicted behavior of the beetle. There is a possibility that the insertion and removal of certain parts of the beetle might lead to abnormal maneuver in flight. In order to achieve the free flight stimulation of cyborg beetle, a protocol for stimulating the muscles must be considered more seriously.

The insect-machine hybrid system needs to have a high capacity battery to maintain the operation of the electronic backpack that is not capable with the current trademark batteries. Developing the miniature fuel cell with high current density would solve the problem when using along with the commercial battery as a secondary power source. It is necessary to use electrocatalyst to increase the reaction rate in cathode and anode in order to achieve high performance in fuel cell. This thesis will focus on developing the electrocatalyst for the cathode part of the fuel cell. Palladium (Pd) is chosen for the catalyst synthesis due to its comparable catalytic activity and high durability over

4

Platinum (Pt). Although many efforts to improve the performance of Pd catalysts have been demonstrated, the synthesis process is complicated and some time required hash conditions. Thus, there is a need of more facile method to produce the Pd catalyst for fuel cell which also has high electrocatalytic activity.

1.3 Objective and Scope

In spite of the long history of insect flight, the roles of individual flight muscles are still unclear because of the inability to stimulate the insect in free flight. The 3Ax muscle and subalar muscle are small flight muscles connect directly to the wing base of the beetle. The 3Ax muscle has been thought to have the function of folding the wing while the subalar muscle has been linked with the role of regulating wing rotation angle [13-16]. However, detail evaluations of wing kinetics and free flight behavior in beetle are needed to define the real effects of those muscles in flight. In addition, to develop a high performance fuel cell for self-powered insect-machine hybrid system requires a Pd electrocatalyst that have high catalytic activity and durability for constructing the cathode.

Therefore, my PhD thesis will focus on:

- Evaluating the role of individual flight muscles in untethered flight by implementation of the miniaturized electrical stimulation backpack and the 3D motion capture system.
- Evaluating the function of the 3Ax muscle that is used to induce left/ right turning.
- Evaluating the braking function of subalar muscle of the beetle in flight.
- Synthesis and evaluating the B-doped Pd nanoparticle electrocatalyst.

1.4 Significance

- Provide more understanding of insect flight and the role of individual muscles (3Ax and subalar muscles) in flight especially in untethered condition that would lead to many surprising results.

- The model of induced forces by electrical stimulation would help modeling the dynamics system of the insect.

- Facile and efficient method for synthesizing Pd nanoparticle electrocatalyst for fuel cell.

- Higher catalytic activity than commercial Pd catalyst.

1.5 Organization of the Thesis

Chapter 1 gives a brief introduction, motivation, objectives and scopes as well as the significances of the project. The organization of the report is also included.

Chapter 2 presents the literature review of the project. It includes the introduction of insect flight and the stimulation methods used to control the insect maneuver in flight as well as the fuel cell and electrocatalyst.

Chapter 3 describes the experiment procedure for insect flight.

Chapter 4 discusses and evaluates the function of 3Ax muscle in flight.

Chapter 5 discusses and evaluates the function of subalar muscle in flight.

Chapter 6 discusses and evaluates the Pd-B nanoparticles catalyst.

Chapter 7 presents the conclusion based on the result obtained and gives suggestion for the future work on insect-machine hybrid system.

Chapter 2 : Literature Review

2.1 Insect Flight

Although the earliest concepts for flight mechanism were inspired by bird and insect flapping motion, the appearance of fixed wing flight apparatus of Sir George Cayley in 1799 led to the development of flying machine to new direction that bypassed such complex motion. However, it could not stop biologists from investigating the animal flight and getting more attention after the remarkable appearance of the first ornithopter of Alexander Lippisch in the late of 1920s [3]. As a part of that trend, insect flight also showed a remarkable development from just study of insect flight function based on the anatomy to investigating the aerodynamics of insect flapping.

2.1.1: Anatomy of winged insect

The winged insect body is generally divided into the main segments: head, prothorax, pterothorax (mesothorax and metathorax), wings and abdomen (Figure 2.1).

Thoracic design and wing articulations

The pterothorax is the basement of insect flight machine that is made of the cuticular plates with distinct boundaries called sclerites (Figure 2.2a). Dorsally, the thoracic segment is bounded by notum (notal sclerite) and is divided into a posterior scutellum and an anterior scutum. The basalar and subalar sclerites articulate with the pleural wing process in anterior and posterior position; they all locate just beneath the wing base. The ventral limit is defined by sternum while the lateral boundaries are constructed by the two plural sclerites termed (pleuron/pleura). The pleuron is segmented into small parts as episternum and epismeron.

Wings are the key parts that reflect the capability and adaptation of flight in the evolution of insects. Their function is to generate the aerodynamic forces during the insect flight (Figure 2.2b). The insect wings are the thin membranes that are supported by the veins system. They are divided into zones during the evolution to enhance not only the rigidity but also the flexibility in deformation and folding. That enables the insect fold its wings at rest or changing the wing shape during flight as a part of flight maneuver.
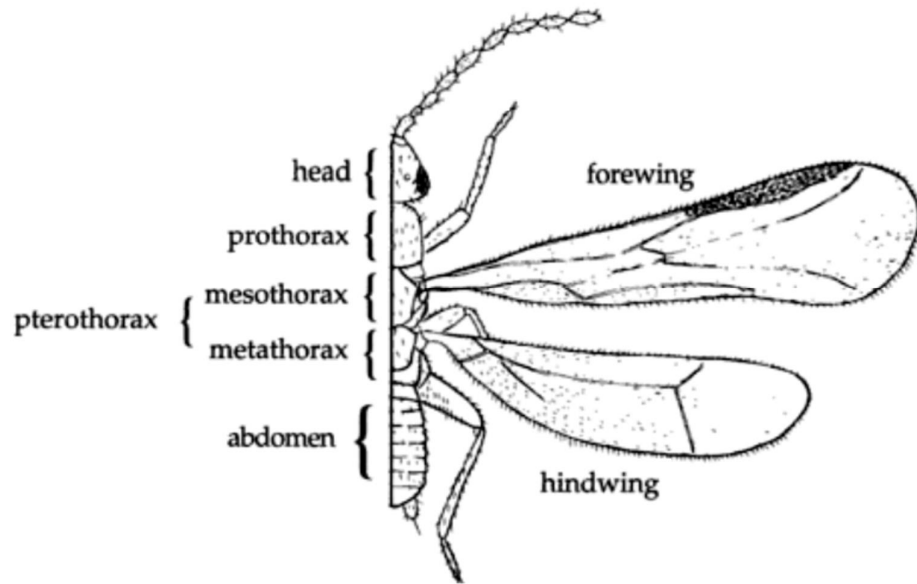
Figure 2.1. General insect segments (Zoraptera: Zorotypus brasilensis) [13]
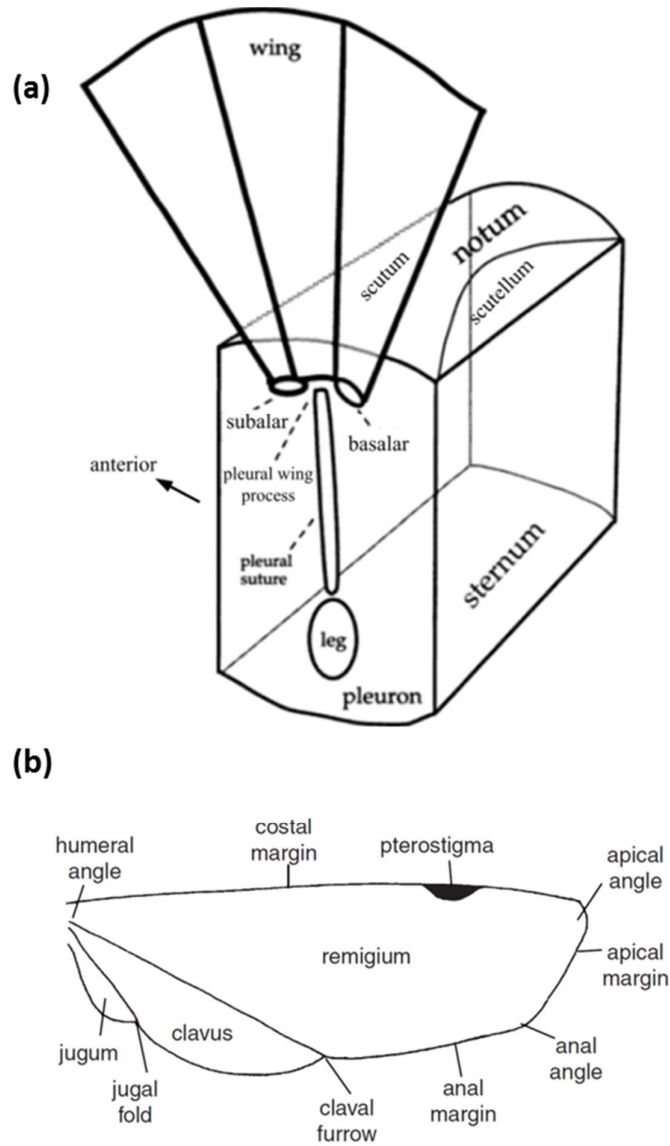
Figure 2.2. (a) General anatomy of pterothoracic segment [13]. (b) Insect wing and its regions (Diptera) [15].

The wing connects to the thorax by the membranous layers that hold the axillary sclerites, which are actuated by the flight muscles to produce the wing movement (Figure 2.3). The three common sclerites were named after Snodgrass [16]. The first sclerite forms a horizontal hinge and acticulates with the anterior notal process. The

second one has connection with both dorsal and ventral membranes and articulates with first sclerite and the pleural wing process. It also distally supports the base radius and main axis of the wing. The third axillary sclerite (3Ax) forms a vertical hinge which articulates with the second one and the posterior notal process as well as distally connects to the anal veins.
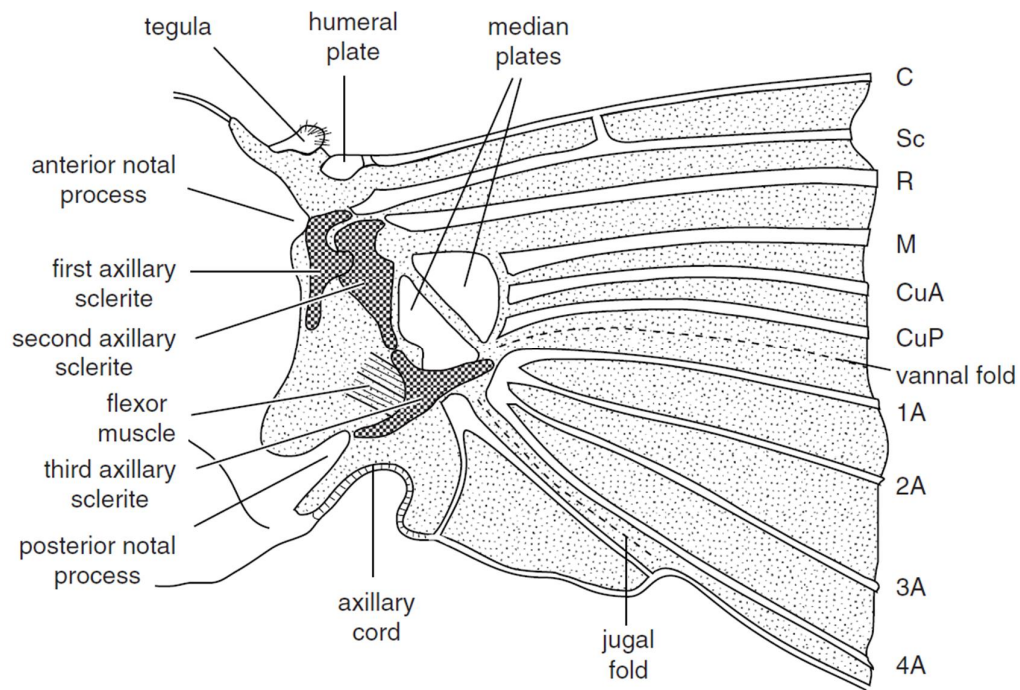
Figure 2.3. Articulation of the wing with thorax [15].

Flight muscles

Insect flight muscles are cataloged in two groups, namely direct flight muscles and indirect flight muscles which have different functions in the flight mechanism. While direct flight muscles directly connect to the wing base and directly cause effect on the wing movement, indirect muscles do not connect to the wing base but indirectly move the wing by contracting the thorax [13, 15-18].

11

Indirect flight muscles (Figure 2.4a) include the dorso-vental muscles (DVMs) and dorso-longitudinal muscles (DLMs) and are considered as the main power supplier for the flying mechanism. The dorso-ventral muscle arises vertically from sternum and connects to the notum; its contraction would depress the thorax vertically that helps elevate the wing. The dorso-longitudinal muscle runs along the body and links the anterior and posteria cuticles; its contraction distorts the thorax in longitudinal direction that makes the wing extend.

Direct flight muscles (Figure 2.4b) connect to the sclerites through the ligaments and a cup like cuticles called apodema. The basalar and subalar muscles arise from pleuron and coxa respectively and insert onto apodema of the basalar and subalar sclerites. These muscles are known using for depressing and twisting the wing. In addition, another muscle connects the third axillary through a tendon that would help folding the anal part of the wing and pull the wing backward.
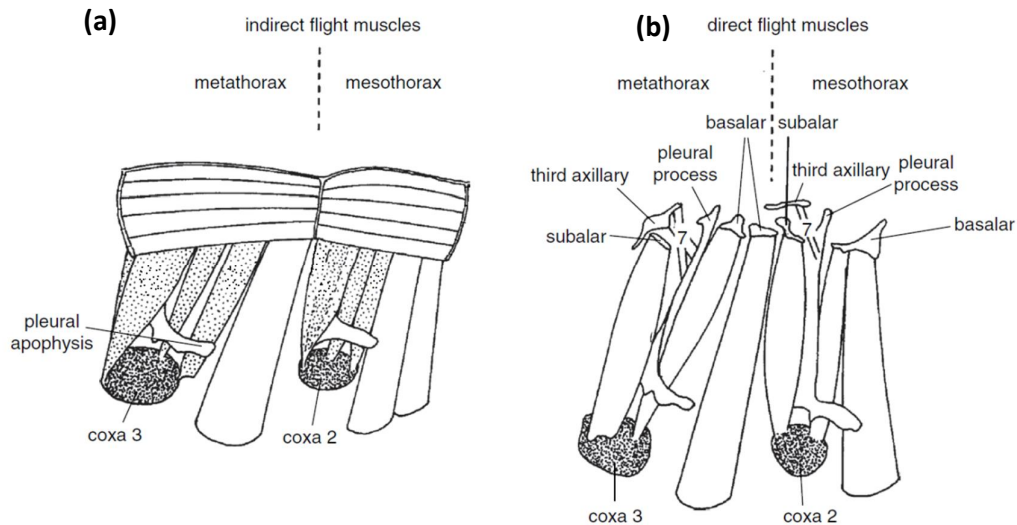
Figure 2.4. The flight muscles (locust) (a) Indirect flight muscles. (b) Direct flight muscles [15].

2.1.2: The production of flapping wing

As in the simple models, the wing flapping motion is produced by the upward and downward motion of the wings. While the contraction of DVM pulls the tergum and its articulation with the wing down to move the wing upward, the downward movement is more complicated since it is not unique throughout the insects. In some insects, the contraction of DLM pushes the wing articulation up that moves the wing down (Figure 2.5a-b). Other insects show that the downward movement of the wings can be made by the contraction of basalar and subalar muscles or the combination of DLM and those muscles (Figure 2.5c-d) [13-16].
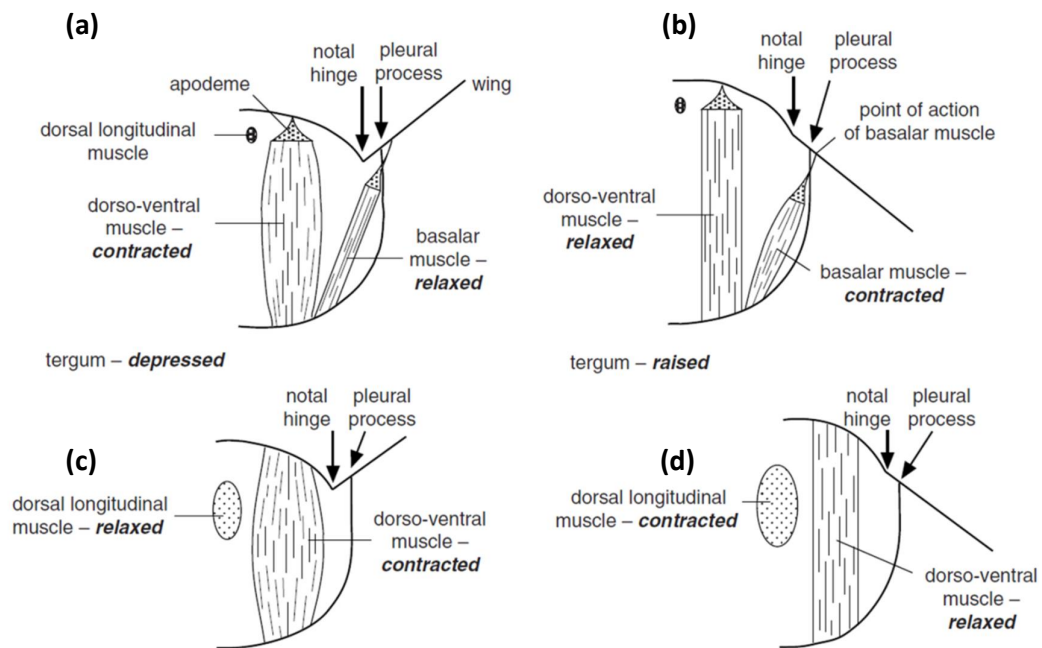
Figure 2.5. Simplified muscle configurations for wing movements.

(a) The indirect dorso-ventral muscles cause wing elevation; (b) direct muscles cause depression, such as in dragonfly (Odonota). (c) The upward movement of the wing is produced by the dorso-ventral muscle; (d) the downward movement is caused by the dorsal longitudinal muscle, such as in fly (Drosophila) [15].

2.1.3: Wing kinematics

The general wing kinematics parameters includes wing beat frequency, stroke plane angle, stroke amplitude and wing rotation. Wing beat frequency varies from animal to animal and negatively correlates with body mass. It would involve in regulating the aerodynamics power in some insects but the correlation is not always consistent. The change of thorax temperature can change the wing beat frequency that mostly affects the stroke amplitude in most insects but it has no effect in causing the asymmetry of the lateral forces.

The average plane that consists of wing movements relative to the body in each stroke cycle is termed stroke plane (Figure 2.6a). The stroke plane angle is defined as its incline angle relative to the longitudinal axis of the insect body. This angle remains more or less constant in most of the insects with low wing beat frequencies. While hovering insects show the horizontal stroke plane, that of non-hovering insects incline toward the vertical. The difference of the stroke plane angle in left and right wings may cause the lateral turn [13, 15, 19, 20].

Stroke amplitude is the angle defined by the lower and higher limit of the wing in stroke cycle within the stroke plane (Figure 2.6b). The stroke amplitude is the key function for regulating the aerodynamics power and the increasing of stroke amplitude produces higher power. The difference of stroke amplitude in both sides of the insects can be used for turning maneuver as the insect turns away from the higher stroke side [13, 15, 19-23].

During flapping, the wing imposes a sequence of rotations about its longitudinal axis (Figure 2.6c). The pronation is caused when the wing rotates as the leading

edge moves downward at the beginning of the stroke. The motion of turning the leading edge upward is called supination. The angle of attack is regulated by changing the pronation and supination of the wing that leads to change in aerodynamic forces. The angle of attack can be controlled actively by muscle activation or passively through inertial-elastic mechanism [13, 15, 19, 21].
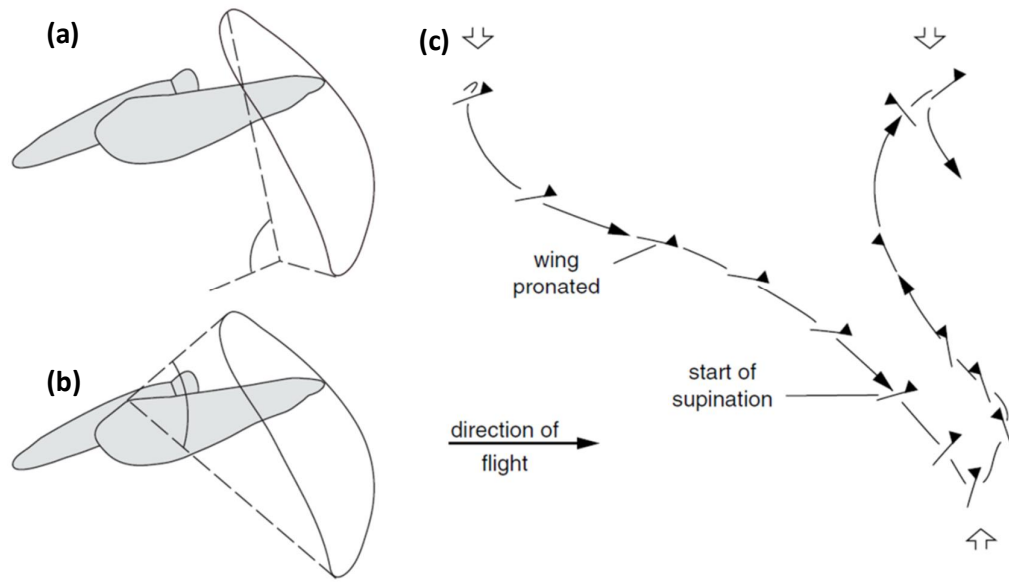
Figure 2.6. (a) Wing stroke plane angle. (b) Stroke amplitude. (c) Wing rotation during flapping [15].

2.1.4: Aerodynamics

Aerodynamics is one of the interesting topics of insect flight with various practical and simulation approach for measuring as well as predicting the aerodynamic forces generated during the flapping motion [13, 24-29]. It not only helps to improve the knowledge of flight maneuver of insect but also promotes the development of MAV and other flying machines.

When the insect flaps their wings, the air flows over the wings and separates at the leading edge. It then turns into a swirling vortex that bond to the wing surface (Figure 2.7). The leading edge vortex causes the pressure reduction on top of the wing that leads to an upward suction force known as vortex lift [13, 15, 28-33].

The aerodynamics forces of flapping wing can be modified when the wing rotates about its axis. The enhancement in aerodynamic forces is caused by the increase in angle of attack as in supination. This is the quasi-steady effect of wing rotation [15, 25, 30, 34].
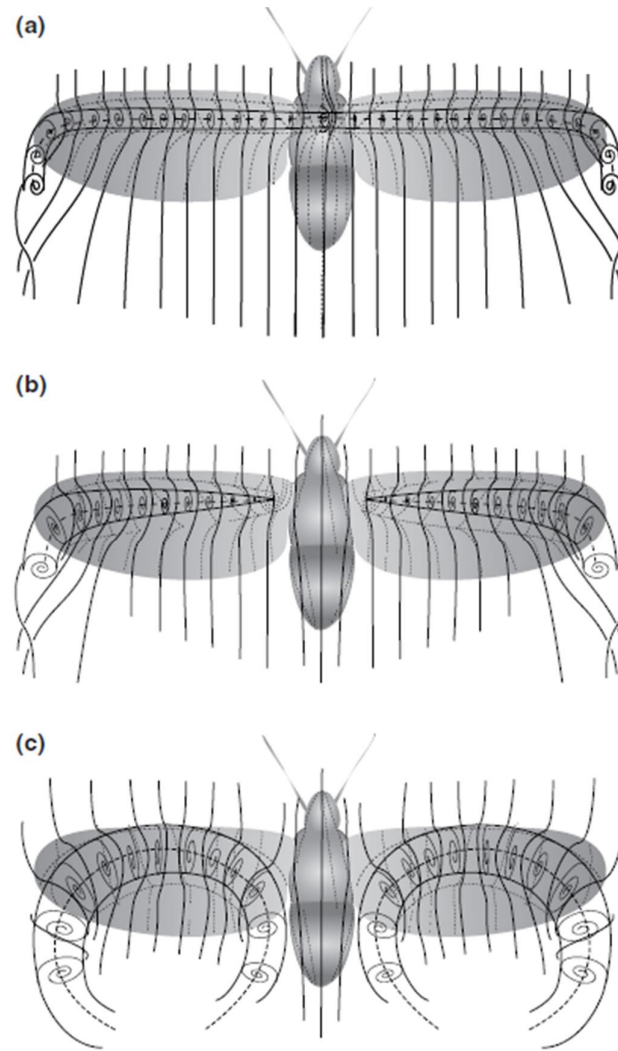
Figure 2.7. Different leading-edge vortex topologies. (a) Extending across the thorax (b) Attaching the wing base (c) Forming horseshoe-shape .

2.2: Control of Insect Flight

2.2.1: Visual stimulation

Optomotor stimulation is a traditional method that is widely used in insect behavior study (Figure 2.8) [18, 20, 23, 33, 35-45]. The insect was placed in a flight arena equipped with the optic flow patterns for recording its behavior and nerve and/or neuromuscular activity. When the visual pattern moves, it excites the insect

optomotor that generates and transmits the electrical potential to the other parts for doing certain functions. It is commonly used for learning of flight maneuver of tethered insect or the untethered small insect as flies.
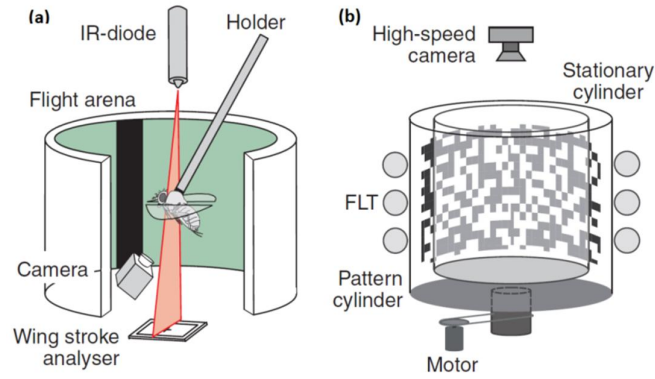
Figure 2.8. Flight arenas for visual stimulation of insect flight [38].

(a) Tethered flight arena for virtual-reality flight stimulator. The fly was fixed on the holder while an infrared light path projected the wings on a wing stroke analyser to measure the wing stroke amplitude. Another camera was used simultaneously for calibrating the measurement. By changing the stroke amplitudes, the fly was able to control the movement of the visual object. This motion also excited the optomotor of the insect that used as its feedback (b) Free flight arena for insect flight dynamics. The fly was let fly freely in the middle of the arena while the visual pattern was rotated by the gear motor. A high speed camera was put on top of the arena to record the optomotor responses of the fly in free flight.

2.2.2: Electrical stimulation of neurons

The electrical signal is applied on the nervous system of the insect like brain, optic lobs, central nervous system, and nerve branch to function the target parts for desired behavior. The popular applications of this method are initiating and stopping of flight by stimulating the optic lobs in beetle (Figure 2.9) and turning by

stimulating the nerve cord inside abdomen of moth (Figure 2.10). When an electrical signal was applied on the optic lobs of the beetle at high frequency, the central nervous system was excited and generated a command to initiate the flight. The beetle stopped flying when a long pulse was applied[46, 47]. In moth, the control of the abdomen movement in flight through a bundle of nerve located inside the abdomen. This motion was reported as having function of balancing the moth flight. The nerve bundle was stimulated partly to derive the desired movement so that it could make turn or pitch up and down [48]. However, the complexity of the nervous system makes it hard to do the control precisely and also faces the high risk of causing some deficits when damage undesired nerve.
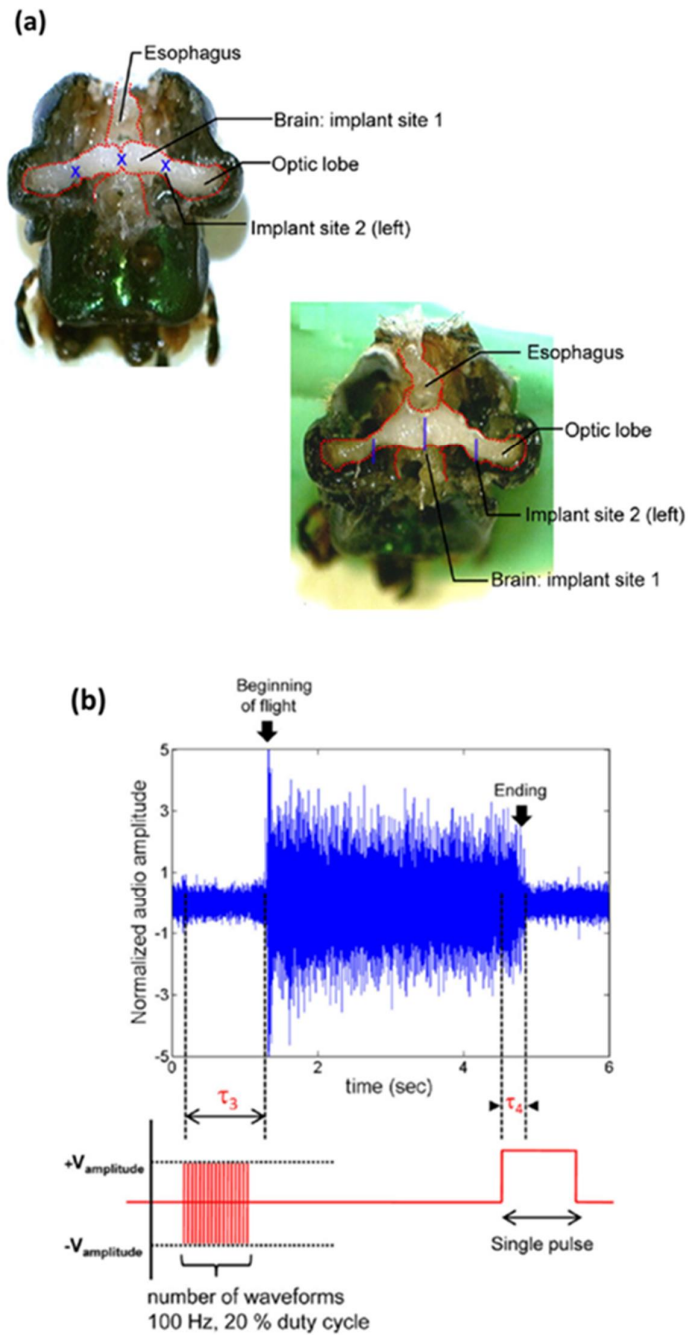
Figure 2.9. Optic lobe stimulation in beetle [46].

(a) The electrodes was implanted into the optic lobes (site 2) of the beetles and connected to a pulse train generator (b) Flight initiation and cessation. When the optic lobes was applied the train of 100Hz, the beetle initiate the flight while the single pulse stop the flight. The audio signal of wing beat was recorded and synchronized with the stimulus signal.
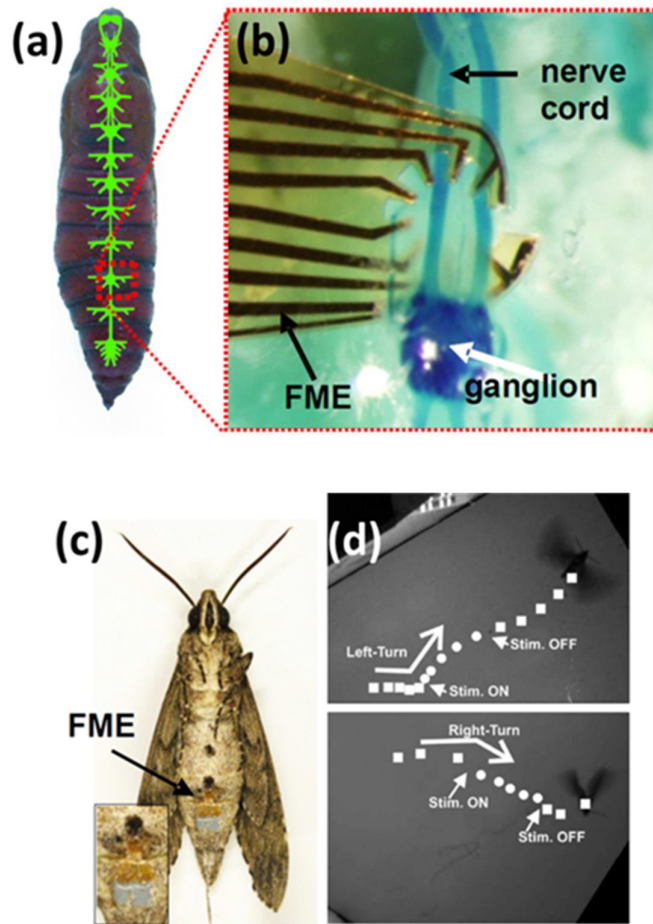
Figure 2.10. Abdomen nerve stimulation in moth [48].

(a) Pupae of moth and its nerve system. (b) Implantation of flexible ring electrode in to the abdomen nerve cord. (c) The cyborg moth with the electrode implanted. (d) Moth turn due to electrical stimulation of abdomen.

2.2.3: Electrical stimulation of muscles

Directly applying the electrical signal on the muscles imposes as a promising method to induce muscle contraction since its targets are well defined. This stimulation method is widely used in the flight muscle and antenna muscle of the insect. The stimulation of flight muscles directly affects kinematics of flapping wing that would help control the flight maneuver of the insect. While the

21

stimulation of indirect flight muscles could produce the flapping motion of the wing in moth (Figure 2.12), that of the beetle's basalar muscle could induce the turn (Figure 2.11) [46, 47, 49]. The stimulation of antenna muscles could control the movement of antenna that affected the mechanosensory system of moth and activated the obstacle avoiding mechanism. As a result, the moth changed its behavior due to such mechanism (Figure 2.12) [50]. Although direct electrical neuromuscular stimulation is considered as the high reliable method in insect stimulation, further study on the influence of electrical stimulation on the untargeted muscle and nerve is lacking.
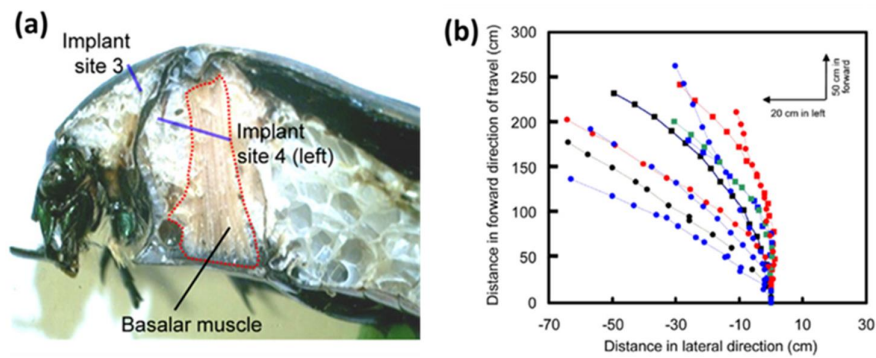
Figure 2.11. Stimulation of the basalar muscle in beetle [46].

(a) The electrodes were implanted into the prothorax (site 3) and the basalar muscle (site 4). The stimulation caused the contraction of the basalar muscle and thus made the beetle turn.

(b) Various flight trajectories shown in different colours of flying beetle when the right basalar muscle was stimulated.
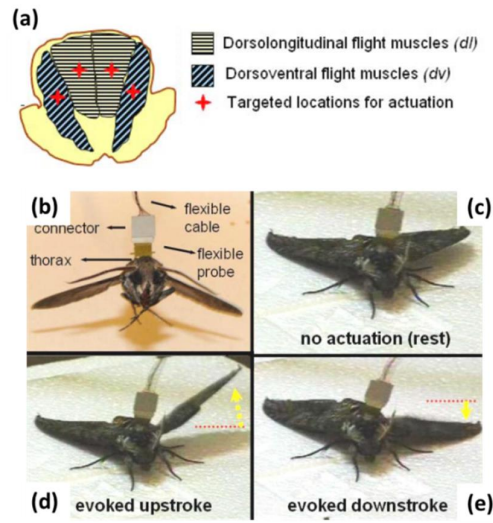
Figure 2.12. The electrical stimulation of DLM and DVM muscles in moth [49].

(a) Cross-section illustration of the thorax showed the positions of implanted electrodes in red crosses. (b) The electrodes were implanted into DVMs and DLMs of a living moth. (c-e) The wing motions were evoked by stimulating the flight muscles.
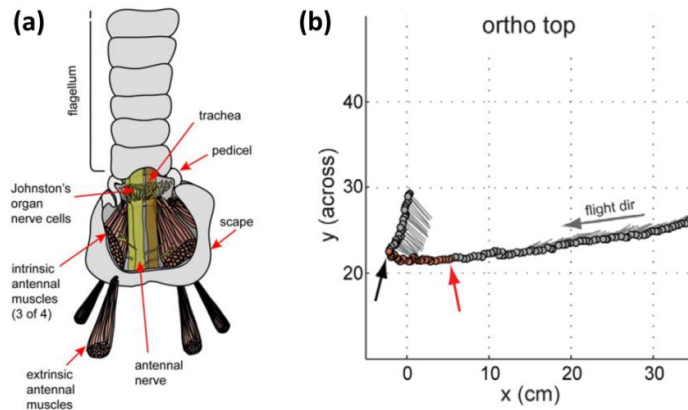
Figure 2.13. Electrical stimulation of extrinsic antennal muscle in moth [50].

(a) The stimulation of the extrinsic muscles make the antenna extends backward that lead to the change of the antenna base strain. This deflection stimulated the local mechanosensors of the moth and caused the change of flight behavior. (b) The trajectory of free flight moth showed its turning motion when extrinsic muscles were stimulated.

2.3: Tethered and Untethered Insect Flight

(a)

(b) 1.6 V_{pp}, 40 Hz to brain

UP **(b1)**   Down **(b2)**   UP **(b3)**
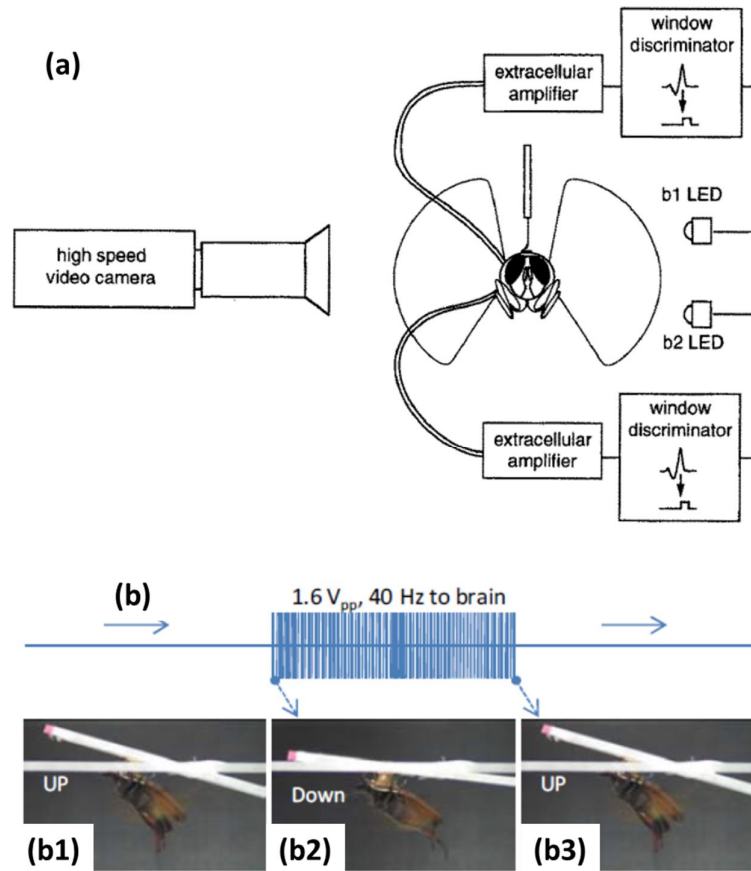
Figure 2.14. Tethered flight experiment.

(a) The experiment for recording of wing kinematics and muscle electromyogram in blowflies. The bipolar electrodes were implanted to the flight muscles whose spikes were amplified for triggering the b1 and b2 LEDs. The wing motion and the brightness of the LEDs were recorded by a high speed camera to associate the muscle activity and wing kinematics [20]. (b) The electrical stimulation of brain induced reduction in climbing rate of the beetle. The beetle was mounted on a gimbal and its behavior was recorded by a video camera from the lateral view to evaluate the change in pitch angle [51].

The insect flight in tethered condition is popular and has a long history from the beginning of this field. The insect was fixed on the holder or loosely wired when the recording and/or stimulation were carried out (Figure 2.14). The tethered condition mostly was used for studying about the insect flight mechanism when the flapping wing motion was recorded by the high speed cameras for the kinematics and aerodynamics analysis. The insect physiology was also developed by using these experiments along with recording or stimulating the nerve and muscle activity to define their roles during the flapping maneuver. Nonetheless, the flight maneuver must be more complex than just flapping and the tethered flight might bypass the effect of many important parameters [20, 47, 51].
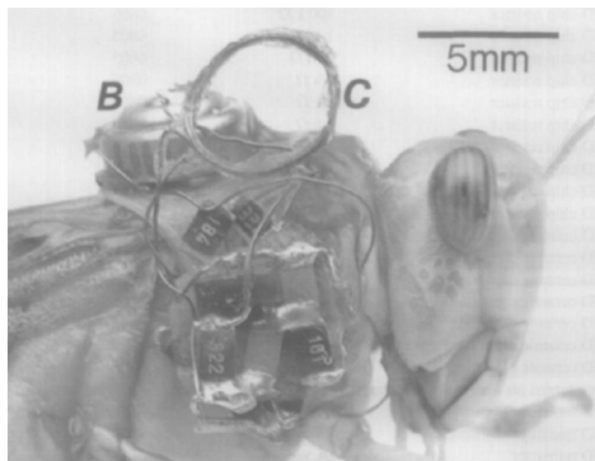
Figure 2.15. The transmitter made of surface mount electronic components was attached on the pronotum of the adult locust. The electrodes were implanted into subalar and basalar muscle to record their activities [9].

The inability of mountable devices leaded to the limitation of insect flight that bonded to the tethered condition for a very long period. Although the attempt to control the insect turning in free flight condition was introduced by using the visual

stimulation in an enclosed fly arena. But it's just applicable for learning insect flight dynamics and would regardless the roles of the individual muscles in flight. The development of electronic device enables the possibility of measuring the muscle potential and stimulating the nervous system or neuromuscular system in untethered condition. The muscle potential recording of the moth and locust in free flight was introduced from the early 1990s (Figure 2.15) [9, 10, 52, 53]. It opened a new era on the field of insect flight when the benefit of miniaturized electronic devices met the idea of insect-machine hybrid system. The achievement in control of insect flight in untethered condition in the recent decade was marked by the appearance of the insect-machine hybrid system developed from the living beetle and moth (Figure 2.16) [46, 48, 50, 54]. In these systems, the electrical stimulation was applied on the insect nerve or muscular system to trigger the desired motions of the insect such as flight initiation and turning. It was also predicted that the insect-machine hybrid system would lead to a vibrant development of this trend. However, further investigation of insect flight control in untethered condition was not carried out due to the technical limitation such as small payload capacity, heavy wireless system and lack of appropriate approach.
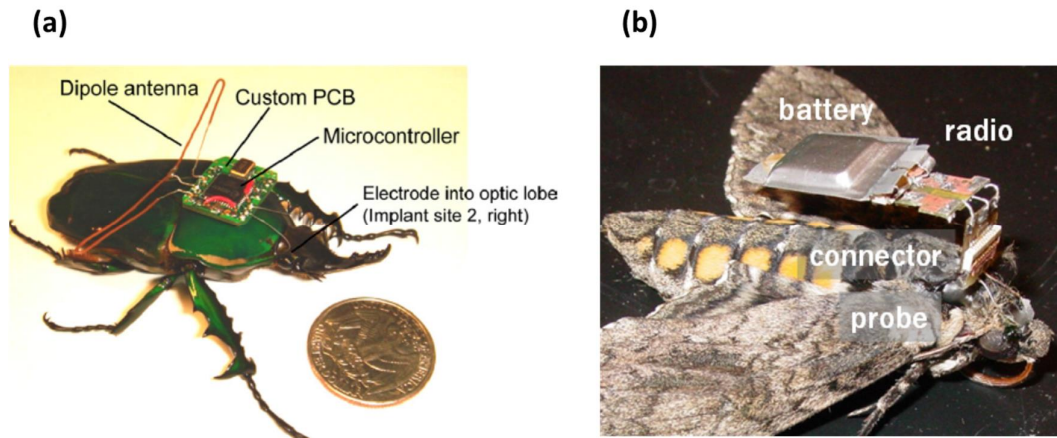
Figure 2.16. Insect-machine hybrid systems were made of living insects and electronic devices mounted on. (a) The wireless electronic board was attached on the pronotum of the living beetle to control the flight initiation/cessation of the insect via the electrodes implanted into the optic lobes [46]. (b) The radio-controlled stimulator was used to control the initiation/cessation of flight in moth by stimulating the brain [54].

2.4: **Fuel cell and nanoparticle catalysts**

2.4.1: **Fuel cell**

Fuel cell is an electrochemical device that produces electrical energy from chemical energy. Fuel cell draws much interest because of its high fuel efficiency, portability and less harmfulness [55]. Fuel cell is also flexible as it can operate on various fuels such as methanol, hydrogen, ethanol and other hydrocarbons. The oxidant for fuel cell is O_2 or air and it emits only H_2O when H_2 is consumed as fuel at the anode. Fuel cell is categorized based on the type of electrolyte as follow[55]:

1. Proton exchange membrane fuel cell (PEMFC)

2. Alkaline fuel cell (AFC)

3. Direct methanol fuel cell (DMFC)

4. Phosphoric acid fuel cell (PAFC)

5. Molten carbonate fuel cell (MCFC)

6. Solid oxide fuel cell (SOFC)

This project focuses on the PEMFC due to many advantages over other fuel cells, including [55]:

- Low operation temperature (less than 90^oC)

- High power density

- Compact

- Easy to handle

PEMFC includes cathode, anode and a proton conductive membrane. The membrane, typically Nafion, only allows hydrogen ions (protons) but not electrons

pass through (electrical insulated) (Figure 2.17). The hydrogen oxidation reaction (HOR) occurs at the anode to oxidized H_2 fuel to hydrogen ions and electrons (Equation 2.1). The electrons go through the circuit load producing the fuel cell current output while protons flow to the cathode through the membrane. At the cathode, the oxygen reduction reaction (ORR) occurs and emits water from hydrogen ions and the arriving electrons (Equation 2.2) [55, 56].

$$\rightarrow 2 \quad + 2 \qquad\qquad (2.1)$$

$$- \quad + 2 \quad + 2 \quad \rightarrow \qquad\qquad (2.2)$$
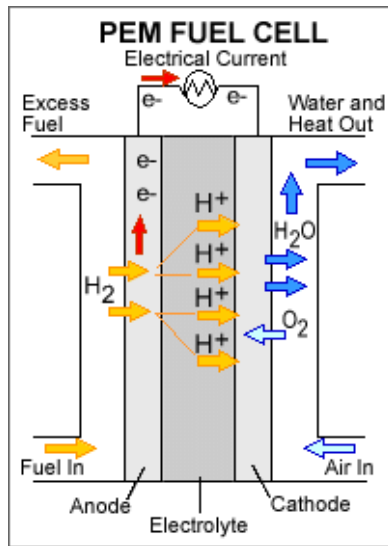
Figure 2.17. Schematic diagram of a PEMFC [55].

2.4.2: Oxygen reduction reaction (ORR)

In PEMFC, ORR is the key reaction occurs in the cathode. As shown in Table 2.1, there are two main pathways of ORR in aqueous solution, four electron (from O_2 to H_2O) reduction pathway or two electron (from O_2 to H_2O_2) pathway. Nonetheless,

29

one electron (from O_2 to O_2^-) reduction pathway can occur in non-aqueous aprotic solvents.

Table 2.1 Thermodynamic electrode potential for O_2 reduction[56].

Electrolyte	ORR reaction	Thermodynamic electrode potential at standard condition (V)
Acidic aqueous solution	+ 4 + 4 → 2 + 2 + 2 → + 2 + 2 → 2	1.229 0.70 1.76
Alkaline aqueous solution	+ + 4 → 4 + + 2 → + + + 2 → 3	0.401 -0.065 0.867
Non-aqueous aprotic solvents	+ → + →	a b

The four electron reduction pathway is preferred as it is more efficient than two electron reduction pathway. In addition, the two reaction pathway generates toxic hydrogen peroxide (H_2O_2) as the product while four electron reaction pathway only gives water as the product [56].

2.4.3: Evaluation of electrocatalysts

Electrocatalysts are used for speeding up the electrochemical reaction rate without being consumed. The slow kinetics of ORR due to strong oxygen double bond (498 kJ/ mol) can be boosted up by decreasing the activation energy by using the electrocatalysts to reduce the electrode potential [57]. For evaluating the performance of the electrocatalysts, the analysis of onset potential [58, 59] and current density at specific potential [60, 61] can be used.

The onset potential evaluation can be achieved by observing the potential at the starting point of the ORR where the current density increases. The better

electrocatalyst would have higher onset potential [58, 59]. Alternatively, the potential of the ORR polarization curve at half of the limiting current is termed half-wave potential and can be used to evaluate the electrocatalyst activity. The higher the half-way potential is, the more active the electrocatalyst is [62, 63]. However, the evaluation based on the onset potential and half-wave potential is not accurate as it does not consider the catalyst load on the electrode.

The evaluation of electrocatalysts based on kinetics current obtained from the Koutecky-Levich equation, the electrochemically active surface area (ECSA, calculated from full cyclic voltammetry) and the loading of the catalyst are more reliable. The mass activity, kinetic current normalized by the amount of catalyst loaded on the electrode, would be one of the key factors to evaluate the effectiveness of the electrocatalyst by giving the amount of current generated per each gram of catalyst [60, 61]. In addition, the specific activity, kinetic current normalized by ECSA, would be able to reflect the actual activity of the electrocatalysts when counting on the amount of active surface that the catalyst has [64, 65].

2.4.4: Platinum (Pt) and Palladium (Pd) nanoparticles as electrocatalysts

Platinum (Pt) and Palladium (Pd) are among the rarest metals in the Earth and considered as noble metals due to their high corrosive resistance and unreactive nature. They are commonly used as catalysts, jewelry and electrodes. Therefore, there are many efforts to seek for alternative materials as they are expensive.

Platinum is often used in fuel cell because of its high activity (specific and mass activities are 0.21 $mAcm^{-2}$ and 0.89 $mA\mu g^{-1}$, respectively, in Pt/C [66]) especially

in ORR despite its high cost. Thus, developing the alternative electrocatalysts has drawn high interest from many researchers in the field of electrochemistry. Efforts to reduce the amount of Pt have been demonstrated by using various support materials (Pt/C, Pt black) and fabricating Pt alloys (PtPd, PtCu) to give bimetallic compounds in order to develop alternative electrocatalysts with higher activity at lower cost [61, 65, 67, 68]. However, Pt has poor durability that might have high initial activity but drops significantly over time. Besides, Pt electrocatalyst is easily poisoned by the electrolyte, which is also a challenge.
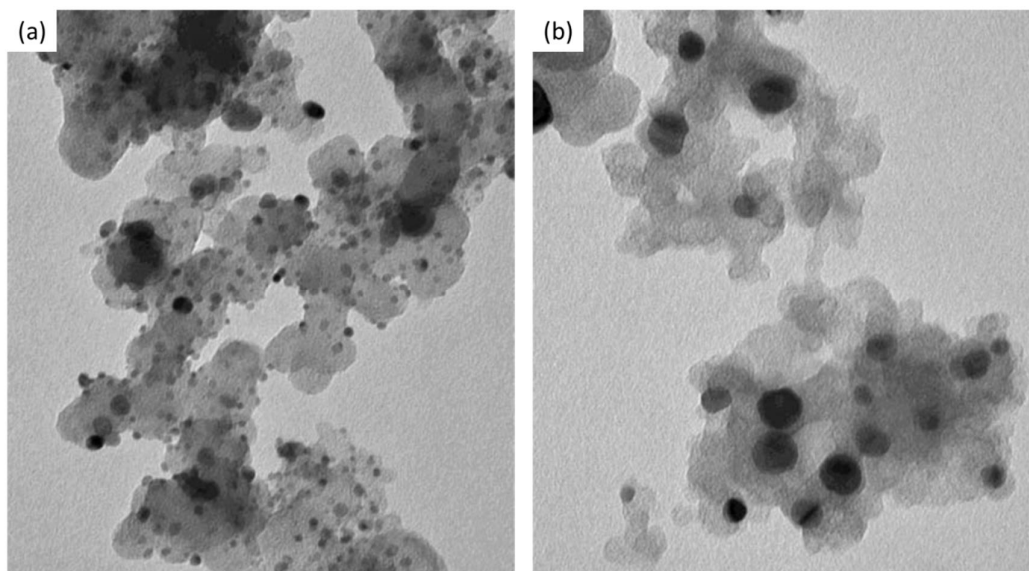
Figure 2.18. TEM images shows difference in size of Pd/C-300 (a) and Pd/C-600 (b) nanoparticles [69].

An approach is to replace Pt by using other metal that have similar or close properties and activity. Pd appeals to be a strong candidate as it is in the same Group 10 metal with Pt but has a more affordable cost. Besides the similar catalytic activity (specific and mass activity of 1.52 mAcm^{-2} and 0.84 mAμg^{-1}) with Pt, especially in ORR, Pd has significantly higher durability [60, 69, 70]. Furthermore,

recent studies on Pd electrocatalysts have shown significant improvement of catalytic performance by implementing various methods including manipulating the size [69], shape [71] and morphology [72, 73] of the Pd nanoparticles as well as fabricating bimetallic Pd nanoparticles [74] (Figures 2.18-19). Manipulating the size of the Pd nanoparticles can change their catalytic activity in ORR. Although there is case that specific and mass activity of Pd nanoparticles increase due to the size of the nanoparticles, more precise control of particle size is required for achieving optimal catalytic activity of Pd nanoparticles in ORR [69]. The Pd nanoparticles can be synthesized in different shapes, such as cubic, spherical [75] and nanorods [76] improving the O_2 adsorption onto the active facets of the catalyst and leading to the improvement in activity. In addition, Pd nanoparticles can be alloyed with titanium (Ti) [77] or iron (Fe) [78] to increase the catalytic activity in ORR. However, more improvement is required as these alloys are still expensive due to high Pd loading used. The catalytic activity of Pd nanoparticles in ORR would be affected by changing the particle morphology that is similar to that observed in other metals such as nickel (Ni), colbalt (Co) and gold (Au) [73, 79]. The amorphous variant of the metal can be achieved by introducing other elements such as nitrogen (N) and phosphorus (P) into the lattice to disrupt the crystal lattice structure that changes the metal from crystalline to amorphous [80]. The defects obtained in amorphous structure are known as preferred binding sites that can improve the catalytic activity [81, 82]. Nonetheless, the amorphous structure causes instability of the catalysts as it may revert back to the crystalline state.
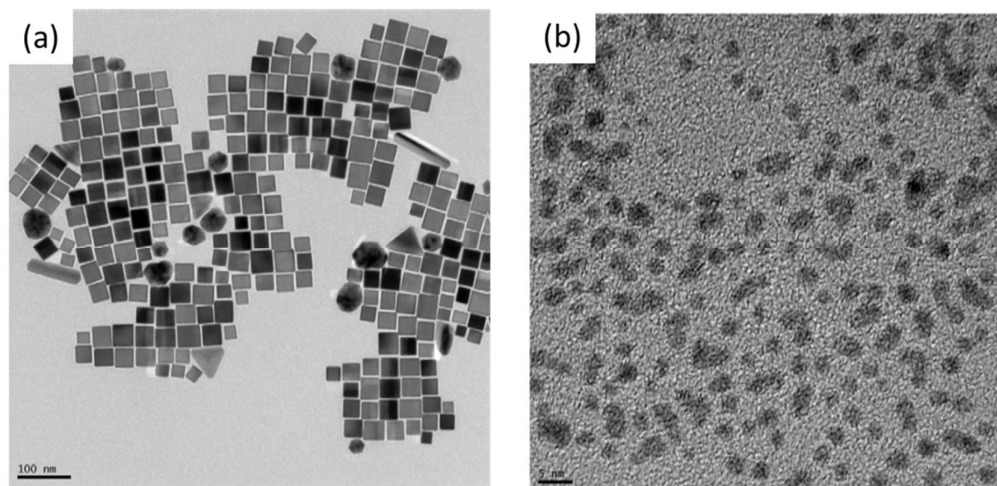
Figure 2.19. TEM images of cubic Pd nanoparticles (a) and spherical Pd nanoparticles (b) [71].

Therefore, this project will focus on developing a Pd nanoparticle electrocatalyst that not only has higher catalytic activity but also obtains higher durability as compared to the commercial Pd catalyst. The lattice structure of the Pd nanoparticles will be manipulated by doping other element without changing in crystalline state. By doing so, the catalytic performance of the Pd nanoparticles can increase and remain over time.

Chapter 3 : Experimental Procedure

3.1: Study Animal

Mecynorrhina torquata (6 cm in length, 8 g in weight) beetles were reared in separate boxes (20 cm × 15 cm × 15 cm) filled with woodpile. A cup of sugar jelly was fed to the beetle twice a week. The humidity and temperature of the rearing room were kept at 60% and 25°C, respectively.
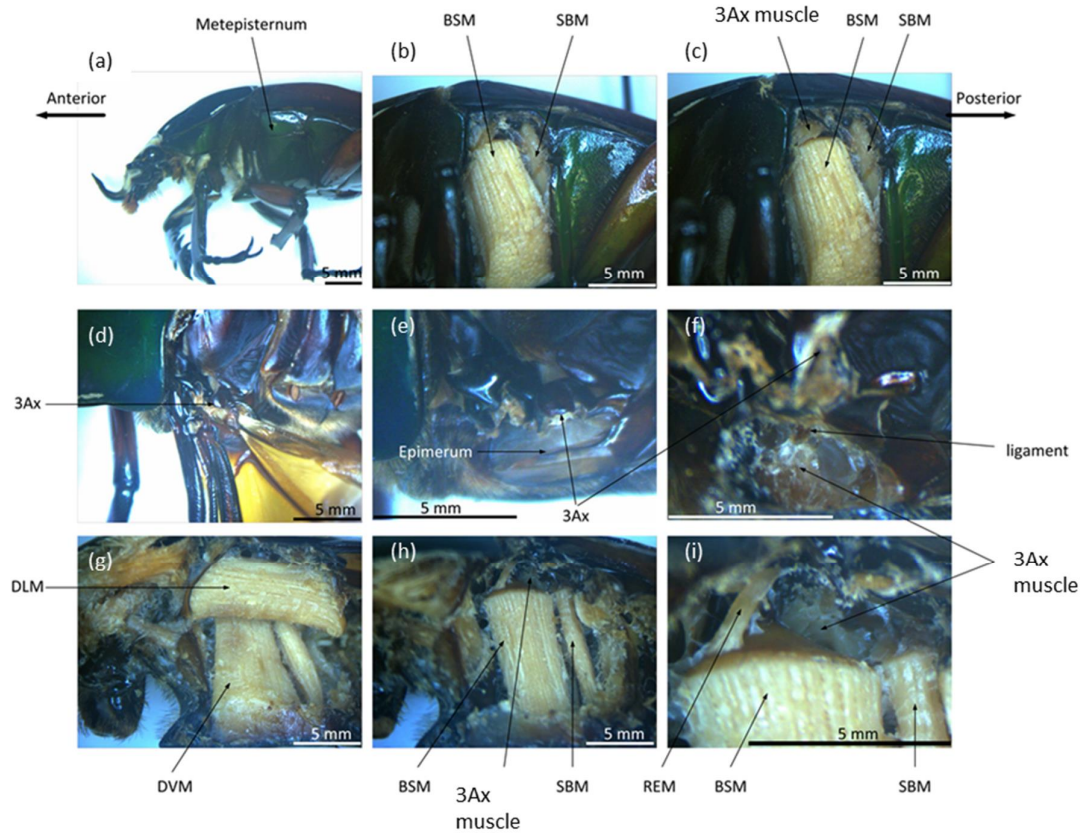
Figure 3.1. Anatomy of flight muscles in Mecynorrhina torquata. BSM- basalar muscle, SBM- subalar muscle, third axillary (3Ax) muscle, REM- remoter extensoris muscle, DVM- dorso-ventral muscle, DLM- dorsal longitudinal muscle.

The anatomy of beetle flight muscles has the same basic parts in general. However, the configuration of the muscle is distinct from other insects. The 3Ax muscle lies above and between basalar and subalar muscles (Figure 3.1). This muscle is commonly called "wing-folding muscle" since it is thought to have the main function of folding wing [14, 16]. The subalar muscle (SBM) runs from hind leg coxa to posterior part of wing base (Figure 3.1).

3.2:   Electrode Implantation

The beetle's legs were first immobilized by rubber band so that it could not disturb the implantation. An insect pin (#00, Indigo Instruments) was used for making a small hole on the cuticle above the muscle. The bare silver wire of one side of the PFA-coated silver wire (127 μm in bare diameter, 178 μm in coated diameter; A-M Systems) was exposed by flaming; the bare silver end was then inserted into the muscle to a depth of 3 mm through the small hole made. The electrode was subsequently fixed by applying the melted beeswax onto the cuticle.

For extracellular recording or electromyography (EMG) measurement, the other end of the electrode was exposed and inserted into the ADC input channel of the CC2431 Development Kit. The acquired data was transferred to the computer via a wireless communication through a GINA base station (Professor Kris Pister's laboratory at University of California, Berkeley). For the electrical stimulation in free flight, the electrodes were connected to the output terminal of a wireless backpack that attached on the pronotum of the beetle (see "Wireless backpack assembly").

3.3: Tethered Experiment

3.3.1: Tracking the trajectory of the wing tips

A 2-mm retro-reflective marker was glued at the inner edge of the bending zone of each wing of a tethered beetle and one marker was placed on the scutelum as reference point. The positions of these markers were tracked by using a three-dimensional motion capture system that comprised six T40s cameras (VICON) at 2000 frames per second (fps). The positional data was fed into a computer in real-time via an Ethernet connection and synchronized with the stimulation commands generated or the EMG signal recorded by BeetleCommanderv1.8e.

3.3.2: Presentation of Visual Stimuli

The visual stimuli were projected onto a white sheet attached to an acrylic panel (500mm×400mm×5mm) by a digital light processing projector. The stimuli comprised a left/right moving visual pattern of 20 mm black and white vertical stripes for inducing turning behavior or up/down moving pattern for inducing up/down movement of the beetle. The visual stimulus was generated by a custom-made software BeetleCommander v1.8e. The projector was fixed at a distance of 1 m to the acrylic panel so that the visual pattern fitted within the area of the panel. The implanted beetle which was prepared for the EMG recording was then put in the field of view of the VICON system. The visual stimuli system was set to place the beetle on the opposite side of the projector, with a fixed distance of 200mm between the panel and the beetle's eyes (Figure 3.2a).
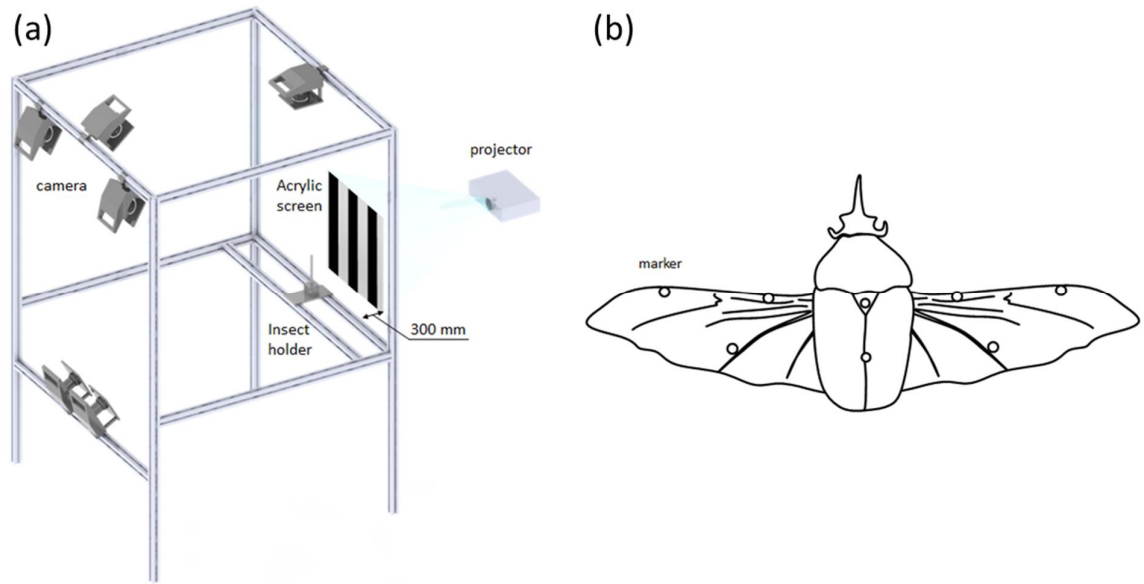
Figure 3.2. Tethered experiment setup for recording wing kinematics of beetle.

(a) Six near infrared cameras was mounted on the aluminum frame to cover a volume of 400 mm x 400 mm x 400 mm surrounding the beetle holder at a frame rate of 1500 fps. The beetle was fixed on the holder with the head toward the acrylic screen (placed around 250 mm from the beetle head) to see the moving pattern projected from the projector. For visual stimulation, the patterns are 20 mm black/ white horizontal stripes moving up and down at 50 Hz within the screen. During the electrical stimulation, the moving stripes were changed to still white background on the screen. **(b)** Each wing of the beetle was attached 3 retro reflective tape markers (2 x 2 mm) for reconstructing the wing kinematics and 2 makers on the body for reference. For the experiment that needed only wing amplitude, only one marker was attached on each wing.

3.3.3: Electrical stimulation

The electrical stimulation was chosen to activate the flight muscle in this study since it is simple and showed high possibility to avoid the deficit of neuromuscular system. A tethered beetle with implanted electrodes to facilitate electrical stimulation was placed in the field of view of the wing tip-tracking VICON camera system. An electrical stimulus (monophasic pulse train, 3.5V amplitude, 3 ms pulse width) was applied by the beetle's backpack that was controlled by the BeetleCommander via wireless communication with the user's computer through the GINA base station. The positional data of the wing tip markers (Figure 3.3b) (wing beat trajectories) were synchronized with the electrical stimulation.

Prior to the application of this method in the experiment, an experiment for checking its influence on the untargeted muscles was carried out. The beetle with stimulation electrodes implanted into the desired muscle and EMG recording electrodes implanted into nearby muscles. The EMG signals of the untargeted muscles were recorded during the stimulation of the desired muscle. If there was no EMG signal obtained from the other muscles, the stimulation method could be confirmed as reliable.

3.3.4: Wing stroke analysis

As shown in Figure 3.3, the mean stroke plane (SP) is formed by the wing base, the starting point of the downs-stroke and the starting point of the up-stroke. (X Y Z) is the global frame while (X' Y' Z') is the frame of the wing stroke plane with the origin at wing base (O). The transverse axis X' and the Z' axis is in the stroke plane that is perpendicular to the Y' axis. The elevation angle, ϕ, is defined as the angle

formed by the leading edge (OO') in the stroke plane relative to the transverse axis X'. The positive value indicates that the wing position is above the transverse axis and the negative value shows the other side of wing position. The deviation angle, θ, is defined as the angle of the leading edge (OO') relative to the stroke plane. If the leading edge is above the stroke plane, the deviation angle is positive else it is negative. (Project the leading edge (OO') to the stroke plane to have (OH) which is then projected to the transverse axis to form (OI). The elevation angle is (HOI) and the deviation angle is (O'OH). The wing rotation angle is the angle of the wing chord (the intersection of the wing with a plane that is perpendicular to the wing) relative to the normal axis Y' of the stroke plane. The wing rotation angle is positive when the wing chord inclines toward the negative direction of the Z' axis [20, 83]. The stroke amplitude (Φ) was defined as the difference between the stroke elevation angle at the beginning of the downstroke and that at the end of the downstroke. The values of the wing kinematics during the 100-ms period immediately before the electrical stimulus timing were averaged to yield the mean wing kinematics in normal flight. Similarly, the values of the wing kinematics during the 100-ms period from 200 ms after the electrical stimulus timing were averaged to yield the mean wing kinematics in stimulated flight. The wing kinematics change was calculated from the difference between the mean wing kinematics in normal and stimulated flights. The beetle was attached three markers for each wing for measuring full wing kinematics. However, for the experiment that just required wing amplitude only, one marker was attached on each wing.
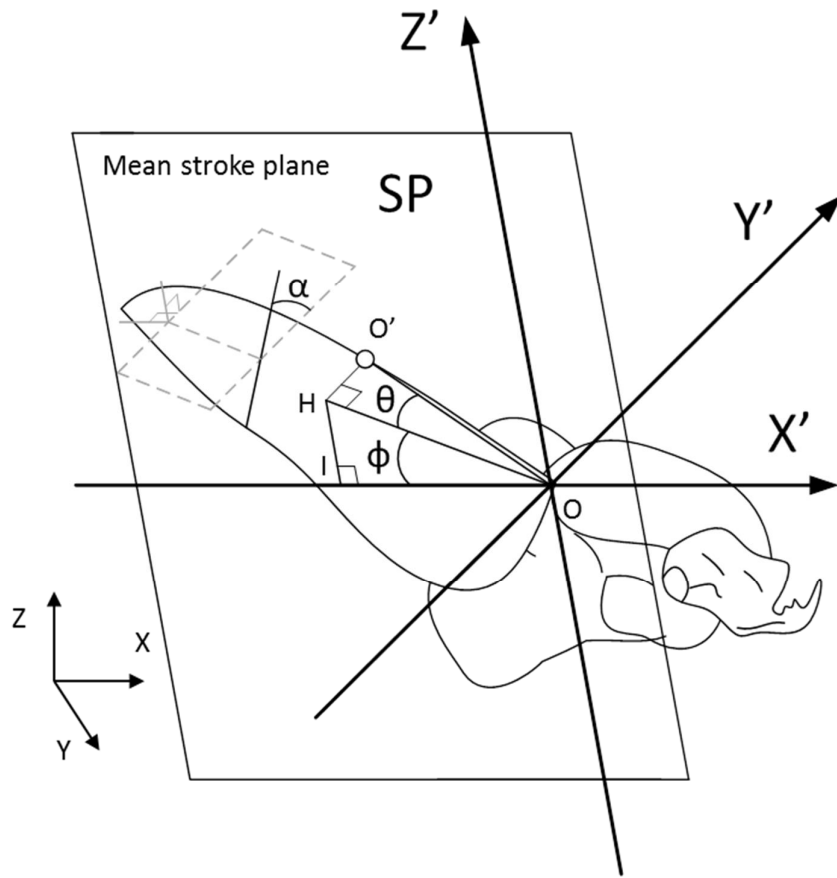
Figure 3.3. An illustration of the wing kinematics.

The three Euler angles of the wing (ϕ – elevation angle, θ – deviation angle and α – wing rotation angle) were defined as shown in the cartoon. The elevation angle is the wing stroke angle measured about the Y' axis in the mean stroke plane; the deviation angle is the out-of-plane angle the leading edge of the wing make with the stroke plane; the wing rotation angle is the angle of the wing chord make with the plane created by leading edge and the Y' axis; (X' Y' Z') is wing stroke plane frame; (x y z) is the global frame. The stroke amplitude (Φ) is defined as the difference between the wing beat elevations at the beginning of the downstroke and the end of the downstroke on the stroke plane.

3.3.5: Third axillary sclerite displacement

A high speed camera is used to record the displacement of 3Ax at 5000 fps. Thin silver wire stimulation electrodes were implanted into the 3Ax muscle (working) and mesothorax center (counter) of a beetle, while the other terminals of the electrodes were connected to a function generator (stimulator).The beetles were immobilized and placed on a wooden plate with the dorsal surface uppermost. The elytra were cut and removed. After that, the hind wings were unfolded and pinned with insect pins. The tendon between 3Ax and the wing base was split with micro-scissors to separate and release 3Ax from being pulled by the wing base. A high-speed camera was set vertically in an upright position so that the lens was close to the face of 3Ax. A surface-mounted technology LED, which was electrically connected to the function generator, was placed on 3Ax so that it could also be filmed with the high-speed camera. The LED blinked synchronously with the stimulus sent to the 3Ax muscle and worked as an indicator of the stimulus timings.

3.4: Free Flight Experiment

3.4.1: Destructive test of 3Ax muscle

The experiment was set up to observe if there was any loosing of steerage when the 3Ax muscle was inactivated by cutting the tendon connects to the 3Ax. An amount of cuticles was removed from metepisternum and epimerum so that we could access this tendon. However, the removal of cuticles might affect the beetle flight and thus required additional experiment for the study of its negligible influence on the flight before cutting the tendon.

The free flight test with removal of cuticles was carried out on 5 beetles. The intact beetles were released for 5 free flight trials (10 s for each trial) to test their capability and motivation in flight. If the beetles were able to finish all the trials, they were then used for free flight experiment. Next, the beetles were released for around 50 trials of free flight again after the removal of metepisternum and epimerum of both sides (Figure 3.1a, e, f). The trial was considered as "successful flight" if it could last more than 10 seconds without any abnormal behavior. Otherwise, it was classified as "failure flight".

Another 5 beetles were used for the destructive test as comparison and prevent the misleading to wrong behavior by exhausted beetles from the free flight test. After testing the flight capability as mentioned above, the tendons between 3Ax muscle and 3Ax were cut through a small window of left and right epimerum of the beetle (Figure 3.1f). The free flight test was then carried out with around 50 trials for each beetle. If the beetle could fly for more than 10 seconds and show no abnormal behavior in steering, the trial was considered as "successful flight", else "failure flight". In addition, a flapping test of around 50 trials for each beetle was carried out after the flight test to ensure that the all the beetles could flap well and the "failure flight" was not caused by flapping maneuver. The flapping trial was counted as "success flapping" if the beetle could flap continuously for more than 10 seconds. If not, it would be counted as "failure flapping".

3.4.2: Wireless backpack assembly

Figure 3.4 shows the photographs and the circuit diagram of the wireless electrical stimulator used for M. torquataare. The wireless system consisted of a base station and a wireless stimulator backpack which was developed based on Chipcon Texas Instruments CC2431 microcontrollers (2.4-GHz IEEE802.15.4 system on a chip). A custom printed circuit board [PCB; FR4, 500 mg] was designed and manufactured for the stimulator based on the circuit diagram. The stimulator was assembled by soldering the electronic components onto the PCB, including a microcontroller, capacitors, resistors, oscillator, terminal headers, and the antenna, as shown in Figure 3.4. The stimulator was subsequently programed to generate the electrical pulse train by loading the custom made software (BeetleBrainv0.99b). A rechargeable micro lithium ion battery (Fullriver, 8.5 mAh, 3.9 V, 350 mg) was used to power the stimulator. A retro-reflective tape (Silver-White, Reflexite) was wrapped around the battery so that it could be detected by the three-dimensional motion capture system (VICON) as a single marker. The positive and negative terminals of the battery were inserted to the power pins of the stimulator that connected to the DVDD and GND pins of the microcontroller, respectively.

Figure 3.4. Schematic diagram (a) and photographs (b) of the backpack (PCB + components = 690 mg, assembled backpack and battery = 1351 mg).

Two channels, including two output pins for each (P1_3 and P1_4, as well as P1_0 and P1_1), were used as stimulating signal generators that were connected to the electrodes via the female headers. The positive and negative terminals of the battery were inserted into the VDD and GND ports of the 10-pin header.

3.4.3: Remote radio control of a freely-flying insect

The flight commands were generated by the BeetleCommander, running on an operation computer, and sent to the back pack through the GINA base station that connected to the computer via a serial port. The BeetleCommander was configured with the electrical stimulus (3 ms pulse width, 3.5V nomophasic pulse train), number of pulses and stimulation frequency (10 – 100 Hz) at the stimulated sites. The CC2431's built-in 2.4-GHz IEEE 802.15.4-compliant RF transceiver transmitted the command signals, using direct sequence spread spectrum RF modulation for broadcasting on a single channel (1 A, 2.48 GHz). A command was sent by the base station to the backpack for 300 ms every 1 ms, as required. The stimulation commands were interpreted by BeetleBrain to modulate the appropriate pulse train of the backpack. The amplitude of the pulse train was regulated using pulse width modulation (PWM), which was a built-in function of the microcontroller. A Nintendo Wii Remote was used by an experimentalist for triggering the BeetleCommander via a Bluethooth transceiver plugged into the computer to issue the appropriate command (left/right and sleep/awake).

After mounting the backpack on the pronotum of the beetle and wiring the electrodes from muscles to the header of the backpack (Figure 3.4-5), the beetle was gently released to fly freely in a closed room using as flight arena (Figure 3.6). The flight arena was covered by white paper in all sides with an air gap to protect the beetle from injure when crashing. Eight T160 cameras and 12 T40s cameras from VICON were used to set a three dimensional motion capture system for tracking the insect flight inside the arena. The retro-reflective tape marker attached on the beetle (see "Wireless backpack assembly") was detected by the motion capture system and

constructed for three dimensional coordinates that were fed to the operation computer. The data was synchronized with the electrical stimulation signal by using BeetleCommander software installed on the computer. The software was also used to visualize the insect behavior by plotting the flight path of the insect. Different colors was used to indicated events of the electrical stimulation (i.e., the event of no stimulation was indicated by black segments, whereas the left and right stimulation events were indicated by green and red segments, respectively).

Figure 3.5. Experimental beetle with the stimulator backpack mounted on the pronotum. The stimulator backpack included a custom-designed printed circuit board (PCB) made of custom-programmed microprocessor unit, micro battery, a set of thin cables and connector are mounted (see also Figure 3.4). Four silver wires were tightly connected to the outputs jumper of the backpack. The other ends of the wires were implanted into 3Ax muscles as working electrodes and the mesothorax center as counter electrodes in both left and right side of the beetle.
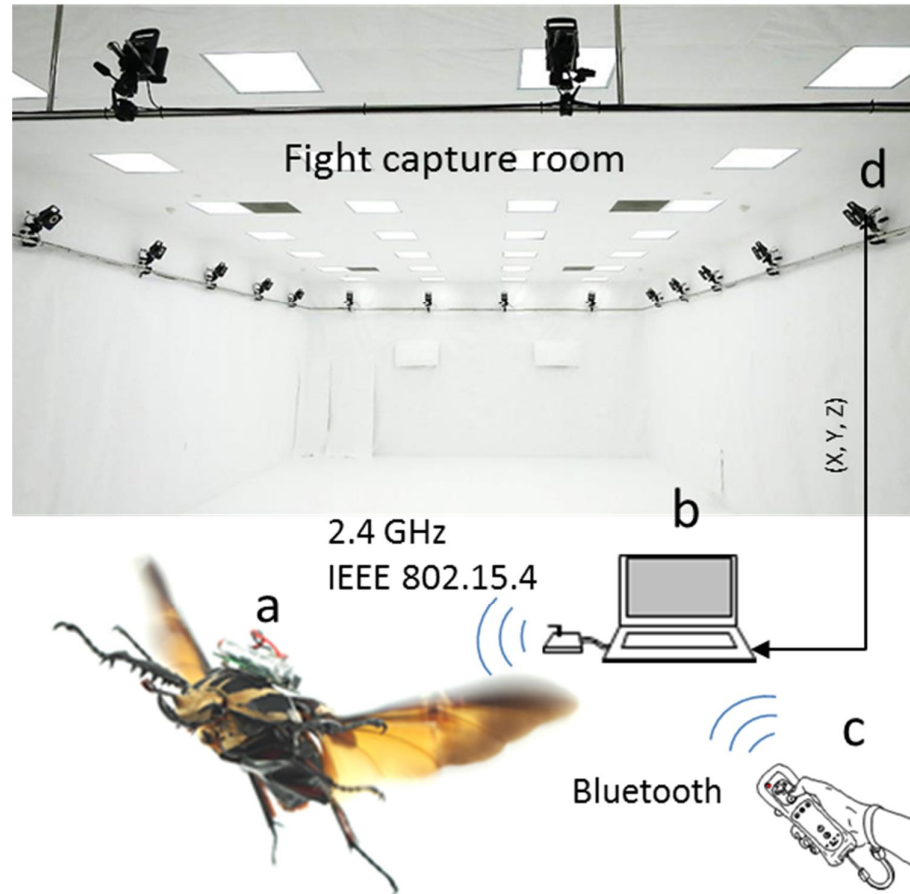
Figure 3.6. The free flight experiment setup.

The experiment was carried out in a flight arena of 12 m x 8 m x 4 m covered with a motion capture system of 20 near infrared cameras (VICON, T40s and T160) (A). The wireless backpack (electrical stimulator) was customized using the TI CC2431 microcontroller with the tiny I/O header for connecting the electrodes and battery. A battery wrapped with retro reflective tape was mounted on the top of the backpack to supply the power and work as a maker for motion tracking (B). After assembling, the beetle (a) received the command from the operation laptop (b) wirelessly via the base station plugged into the laptop when the user pressed the command button of the Wii remote (c). The backpack then applied the electrical stimulus to the target muscle. Meanwhile, the positions of the beetle were recorded by the motion capture system and sent to the operation laptop for synchronizing with the stimulation command.

3.4.4: Free-flight data analysis

All the free-flight trajectories were analyzed by extracting each of their one-second stimulated period (150 ms immediately before the stimulus timing and 850 ms after the onset of the stimulus), smoothing them using a polynomial function, calculating the x, y, z components of velocity and acceleration, and projecting them to horizontal and lateral direction of the flight path by a customized MATLAB program. The normalized vector perpendicular to the direction of flight and the tangential vector parallel to the direction of flight were calculated for each pair of points along the flight path [37, 83, 84]. The lateral acceleration a_l was calculated from the sum of the projected x and y accelerations, i.e., a_x and a_y, respectively, relative to the normal vector of flight at each point. The horizontal acceleration a_h was calculated from the sum of projected x and y acceleration relative to the tangential vector of the flight path at each point. The lateral force F_l was then calculated from the lateral acceleration a_l using the following equation:

$$\vec{F}_l = m\vec{a}_l = m\left(\vec{a}_x \cdot \vec{n} + \vec{a}_y \cdot \vec{n}\right) \tag{3.1}$$

where m is the mass of the beetle and n is the normal vector of the flight path point relative to the center of curvature.

Other forces were estimated in the same way as follows.

Horizontal force was calculated from the horizontal acceleration:

$$\vec{F}_h = m\vec{a}_h = m\left(\vec{a}_x \cdot \vec{h} + \vec{a}_y \cdot \vec{h}\right)$$

$$\tag{3.2}$$

Vertical force:

$$\vec{F}_v = m\vec{a}_v = m\vec{a}_z$$

Total force:

$$\vec{F}_t = \vec{F}_h + \vec{F}_l + \vec{F}_v .$$

The *"stimulation-induced"* force (ΔF) was defined as the difference between the force (F_0) immediately before the stimulus timing and the force (F_1) at 200 ms after the onset of the stimulus (Figure 3.7).

$$\Delta F = F_1 - F_0$$
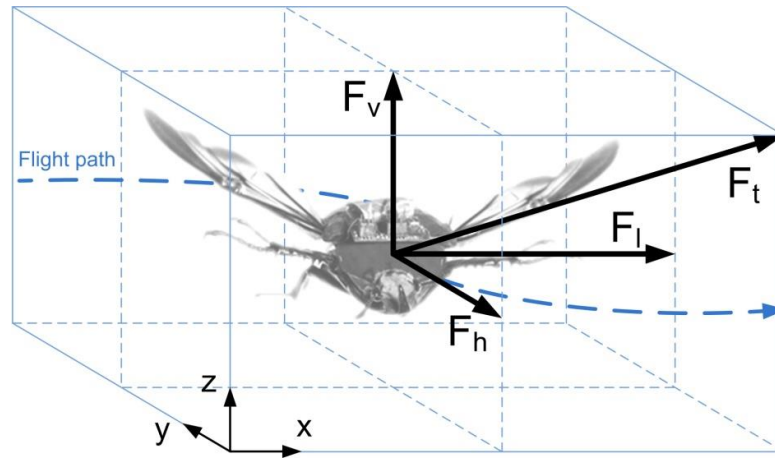
Figure 3.7. Estimated forces for the flying beetle.

The forces were calculated on the basis of the accelerations determined from the free-flight trajectories of the beetle. The lateral force (F_l) was along the transverse axis of the beetle. The sum of the thrust and drag forces was the horizontal force (F_h). The vertical force (F_v) was the sum of the lift and gravity forces. The total flight force was the summed vector of the lateral force, horizontal force, and vertical force.

Chapter 4 : The Function of 3Ax muscle in graded turn

4.1:   Introduction

The ability to stimulate the cells and record the cellular responses for behavior observation is required to evaluate the neuromuscular function in locomotion [85]. It has been a long-standing hurdle of the untethered stimulation for insect flight studies. The rise of miniature electronic devices has enabled ultra-small, radio-enabled electrical stimulators and recorders for freely moving insect [10, 46, 50, 54, 86-88]. The stimulation targets varied from brain for pattern generation [54], nerve cord for abdominal flexion [48], antennal muscles [50, 89], and the flight muscles for turning [46, 47, 90, 91]. However, no graded turning control has been demonstrated in freely flying insect, and the stimulation responses has high variation [46, 48, 50, 54]. Technological limitations have precluded hypotheses of function validation that required the exogenous stimulation in free flight. The muscle whose role involves in wing articulation was investigated to identify its actual function. The muscle that has graded response in turning would enable fine steering control by electrical stimulation that is not previously demonstrated. Such gradation might depend on the muscle firing phase relative to the wing stroke [as shown in b1 muscle of fly [18, 23] or the dorsal longitudinal and ventral muscles of moth [92]], or might be the result of tonic control by summation of twitch responses without phase-dependence that is able to produce various amount of force on the wing hinge [18, 19, 93].

4.2:   The Key Function of 3Ax Muscle in Flight Steering

In coleopteran, the third axillary sclerite (3Ax) muscle was named 3Ax muscle from 19th century based on the observation of the wing folding motion when it was activated. When the muscle contracts, it pulls the 3Ax inward that pulls the wing

54

into the folding posture [14, 16, 94, 95]. Although it was thought to be always activated during the wing folding process, the extracellular recording of 3Ax muscle showed no EMG spike appear in 30% of the tests (Figure 4.1). These results lead to the expectation of other function of 3Ax muscle since it might not exclusively be used for wing folding.
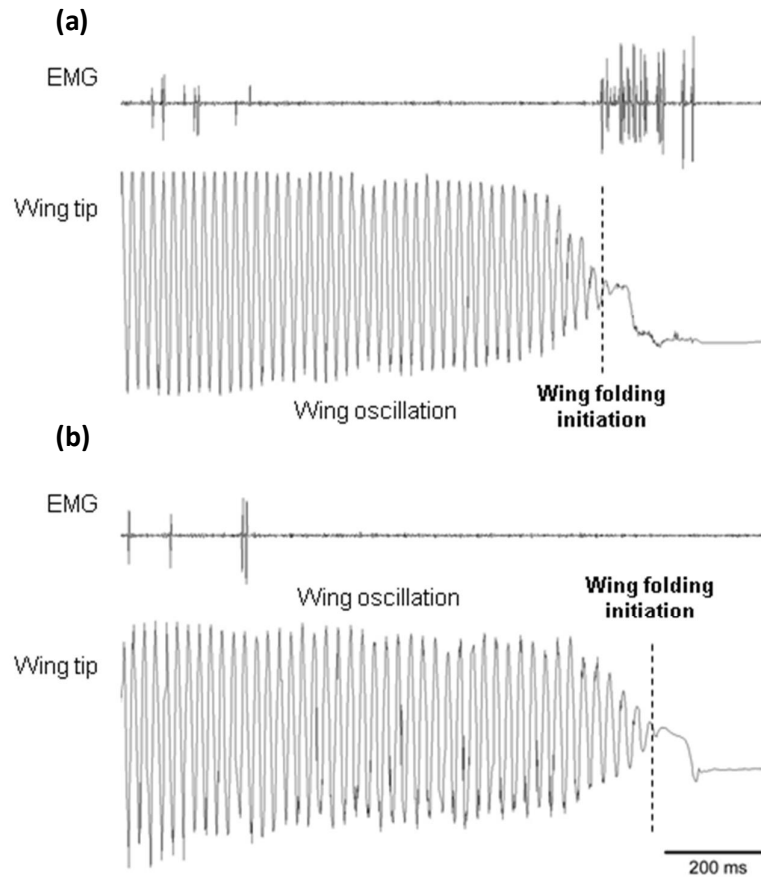
Figure 4.1. Electromyogram (EMG) of 3Ax muscle (3Ax muscle) measured during free flapping followed by wing retraction. The EMG spikes appeared during the wing folding process (a) but there were cases that 3Ax muscle was not activated (b). Oscillations in wing tip coordinates indicate flapping (N = 5 beetles, n = 216 trials).
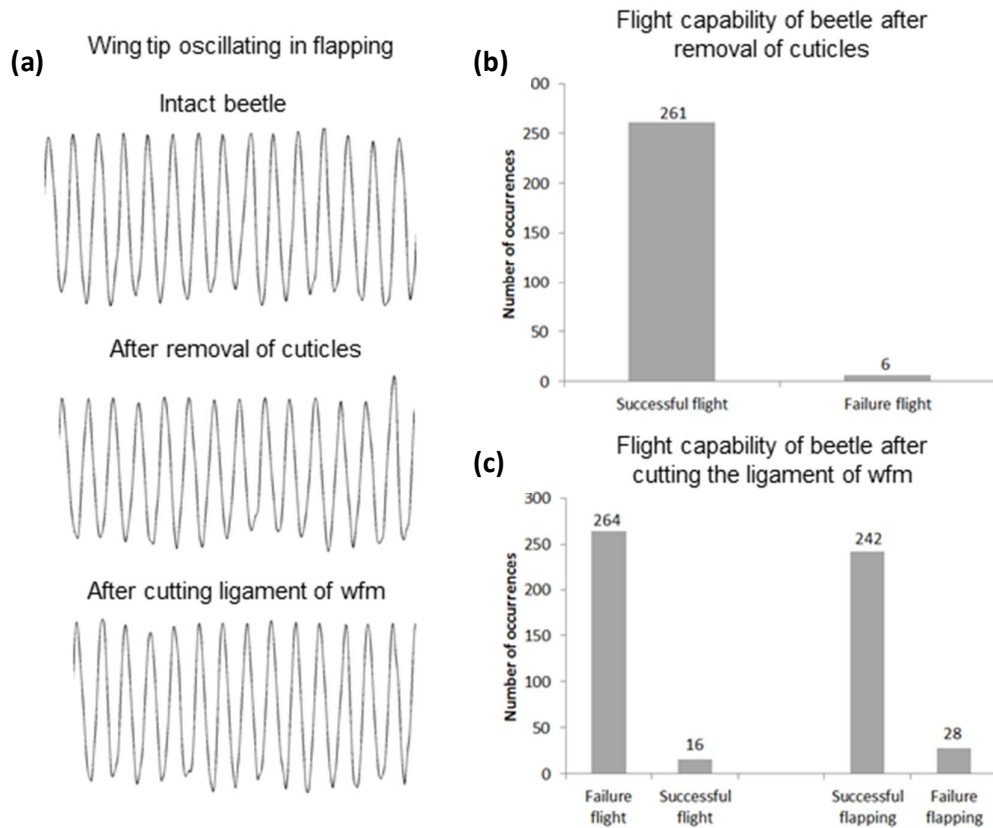
Figure 4.2. Inactivation of 3Ax muscle in free flight.

(a) The wing oscillation of the beetle after the removal of metepisternum and epimerum (second trace) and cut of 3Ax muscle tendon (third trace) did not show any difference from that of the intact beetle. (b) The removal of cuticle did not have any influence on the free flight (N = 5 beetles, n = 267 trials). (c) All the beetles lost their steerage after cutting the 3Ax muscle although they was able to flap their wings (N = 5 beetles, n = 280 trials).

The inactivation of the 3Ax muscle in free flight was carried out for observing how the flight maneuver was affected. At first, the removal of the cuticles did not affect the normal maneuver of the beetles since they all could flew as normally as the intact beetles with the rate of 261 "successful flight" to 267 trials (N = 5 beetles, n = 267 trials). However, cutting the tendon between 3Ax muscle and 3Ax caused steerage losing of all beetles in free flight although it did not cause any restriction of

wing folding/unfolding and flapping when 264 "failure flight" recorded from 280 trials (Figure 4.2) (N = 5 beetles, n = 280 trials). This failure maneuver shows that the 3Ax muscle has an important role in turning during flight.

4.3: The 3Ax muscle was activated on the ipsilateral turn with no preferred firing phase

The extracellular recording of 3Ax muscle during turn showed the association of 3Ax muscle with steering movements. The beetle turned left or right as the responses of optomotor to the application the moving optic flow patterns (black/white stripes). The 3Ax muscle of all the beetles (N = 17 beetles, n = 226 bursts) was activated consistently on the ipsilateral side of the optic flow and inactivated on the contralateral side (Figure 4.3a). 80.68% of the spikes were obtained when the patterns moved to the ipsilateral side, just 5.12 % of the spikes appeared during the contralateral flow and 14.9% of the spikes were seen when there was no optic flow applied. In addition, there might have some delay of optomotor responses when the optic flow ended since most of the spikes obtained without stimulation were in this period (Figure 4.3b). This result supports the hypothesis that the 3Ax muscle has an important role in steering and it is just activated during the ipsilateral turn. It is contradictory to the function of basalar muscle in previous studies when that muscle was activated in both left and right turn but change the firing rate due to turing direction [22, 96].

The histogram of EMG spikes mapped to the wing stroke cycle showed that the beetle activated the 3Ax muscle almost randomly during turn (Figure 4.3c) (in

contrast to the preferred firing phases of the 3Ax muscle in moths and locusts [19, 93, 97]). Although the data showed a preferred wingbeat phase of the spikes, the exact phase varies from beetle to beetle and there were some beetles with no preferred phase of spikes (Figure 4.4). The high variation in wingbeat phase timing of spikes seems to imply, at best, a weak phasic effect of 3Ax muscle activation. This suggests that the 3Ax muscle is activated by the summation of multiple contraction twitches that would gradate the wing base motion and help the beetle do fine steering in flight.
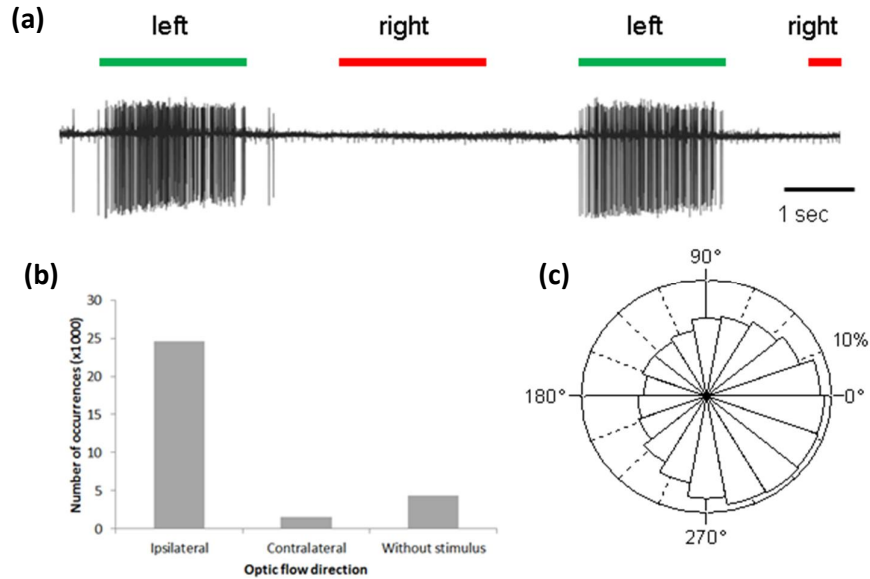
Figure 4.3. Electromyogram (EMG) of 3Ax muscle during turns.

(a) EMG of left 3Ax muscle induced by the visual stimulation measured during left and right turns. The beetle activated the 3Ax muscle while turning to the left. (b) Histogram of EMG spikes measured during the turning induction by the optic flow. (c) Histogram of extracellular recording spike timing of all the beetles mapped on the wing stroke phase (N = 17 beetles, n = 14476 spikes/ 226 bursts).
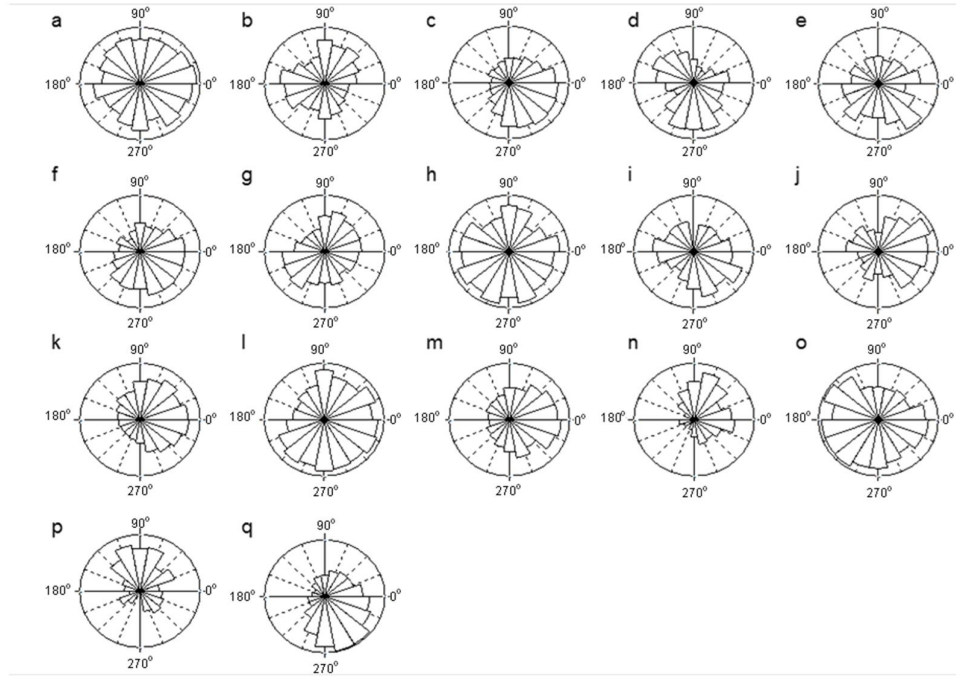
Figure 4.4. Histogram of extracellular recording spikes of 3Ax muscle mapped on wingbeat phase of various beetles (N = 17 beetles). These phases varied from beetles to beetles, had high variation and showed no preferred timing (a, b, d, g, h and i).

4.4:   The 3Ax muscle Acts in the Graded and Tonic Fashion

The electrical stimulation of 3Ax muscle in the tethered beetle pulled the 3Ax inward and its displacement was graded as a function of the stimulus frequency. The displacement of 3Ax was shown as discrete pattern for the frequencies less than 60 Hz, the smooth displacement obtained from 60 Hz was graded increasing while increase the frequency and it reached the high level at 80 Hz (Figure 4.5). This tonic property of 3Ax muscle confirms its capability of producing a graded contraction that fine tunes the turn.
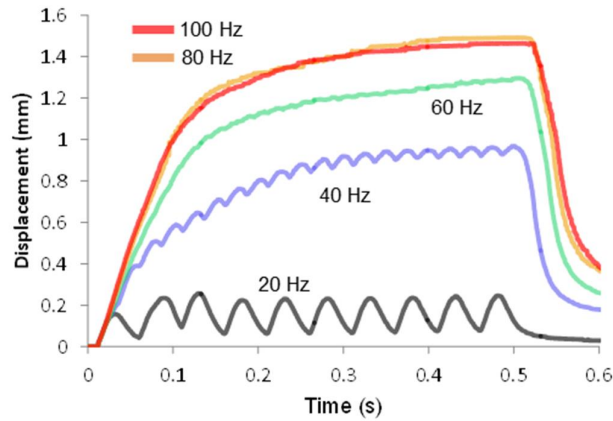
Figure 4.5. Displacement of the third axillary sclerite (3Ax) in response to electrical stimulation of the 3Ax muscle. The pulse trains of 500 ms were applied on the muscle with different stimulus rates (20, 40, 60, 80, and 100 Hz, N = 5 beetles, n = 60 trials).

The EMG recording of other muscles during the electrical stimulation confirms the feasibility of this stimulation technique on 3Ax muscle. No spike was obtained from other muscles when the 3Ax muscle was stimulated. In contrast, the spikes appeared clearly when the stimulation was applied on those muscles or their nerve (Figure 4.6).
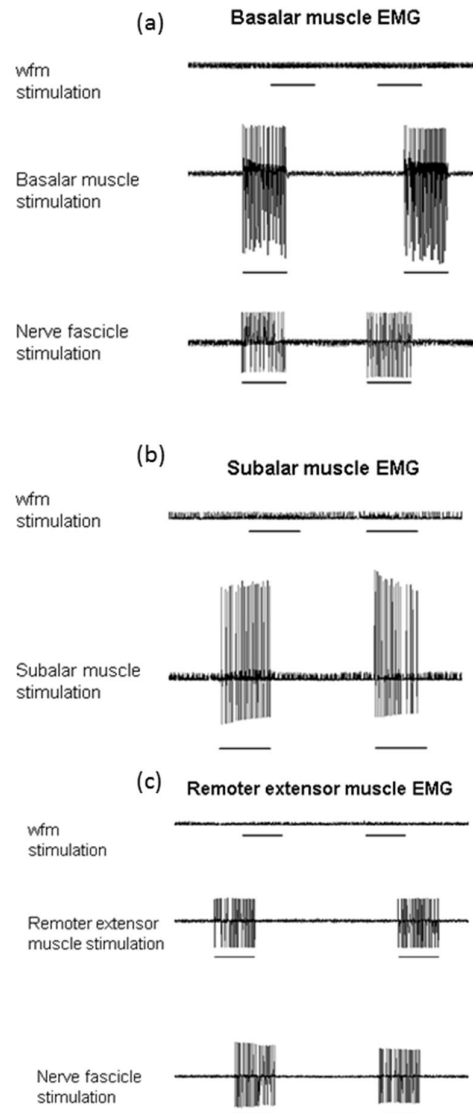
Figure 4.6. The effect of the electrical stimulation on the nearby muscles.

Extracellular recording of the basalar (a), remoter extensoris (b) and subalar muscles (c) during the electrical stimulus of 3Ax muscle. The top traces are EMG recording when 3Ax muscle was stimulated while the second and third traces respectively represent EMG recording when the muscle itself and its nerve were stimulated. The nerve stimulation of subalar muscle was not carried out since it required the removal of other muscles. The black bars beneath the EMG traces are 500 ms timing of electrical stimulation (N = 5 beetles, n = 400 tests).
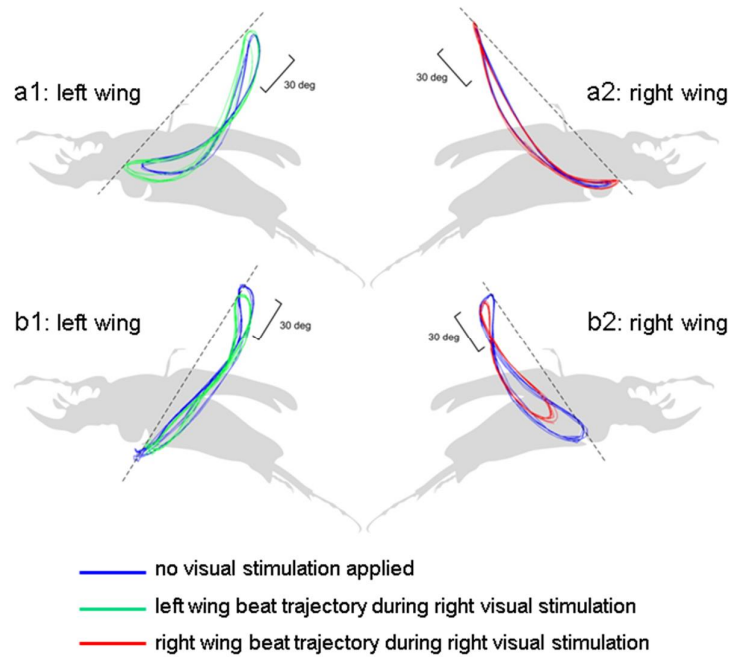
Figure 4.7. Lateral view of the wing tip trajectory of a beetle during visual stimulation. The black and white stripes moving rightward to induce fictive turn in beetle. The results show two possible mechanisms for turning in flight : (a) increasing the contralateral stroke amplitude in degrees (a1) while retaining the ipsilateral stroke (a2), and (b) retaining the contralateral stroke amplitude (b1) while reducing the ipsilateral stroke (b2). Without visual stimulation (blue), the wing amplitudes were retained on both sides. Right visual stimulation increased the left stroke amplitude (green, a1) while retaining the right stroke amplitude (red, a2). Right visual stimulation retained the left stroke amplitude (green, b1) while reducing the right stroke amplitude (red, b2). The dashed line denotes the wing stroke plane, whereas the scale bar represents the stroke amplitude in degrees.

When the optic flow patterns was applied, the beetle reduced the ipsilateral wing amplitude (and did not change in contralateral one) or did not change the ipsilateral wing amplitude (and increased in the contralateral one) (Figure 4.7), which was also mentioned in previous studies [22]. The reduction of wing amplitude is associated with the activation of 3Ax muscle in the ipsilateral side of the turn. Additional

analysis of wing beat trajectory during the electrical stimulation of 3Ax muscle showed that 3Ax muscle caused the reduction of ipsilateral wing amplitude whereas the contralateral stroke amplitude was retained or fluctuated by an insignificant amount. In addition, the stimulation of 3Ax muscle in tethered flight caused the reduction of wing stroke amplitude in a graded fashion that would cause the graded change of flight forces. The higher stimulation frequency led to a higher reduction of stroke amplitude (Figure 4.8).
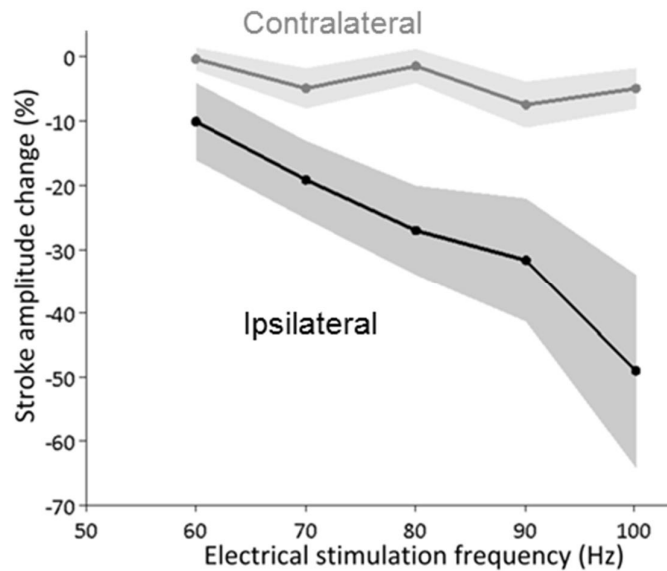
Figure 4.8. Reduction of the stroke amplitude on the ipsilateral side (black) and contralateral side (grey) in response to electrical stimulation of the 3Ax muscle at different frequencies. The shaped region denote 95% confidence interval (N = 5 beetles, n = 91 trials).

4.5: **Remote Electrical Stimulation of 3Ax muscle Enables Graded Left-Right Turn Control in Free Flight**

The stimulation of 3Ax muscle in free flight could produce graded turns as the result of the three key observations: 3Ax muscle fired only on the ipsilateral side; the spike timing and wing stroke phase have just a weak correlation; and the electrical stimulation of 3Ax muscle caused the graded reduction of wing amplitude that depends on frequency. The 3Ax muscle of the free-flight beetle was stimulated via a wireless backpack attached on the pronotum of the beetle. As a result, the beetle turned to the ipsilateral side of the stimulation as Figure 4.9 showed the beetle made right turn when the right 3Ax muscle was stimulated and left turn when we stimulated the left 3Ax muscle. Sequential stimulation of the left and right 3Ax muscle could produce the zigzag flight path (Figure 4.9a) while a large curve could be made by stimulating the 3Ax muscle in right side (Figure 4.9b). Moreover, the produced lateral force was graded as a function of the stimulus frequency. The stimulation frequencies lower than 60 Hz had less effect on turning and 100 Hz some time caused the abnormal maneuver due to the over reduction of wing amplitude. The most effective lateral force was induced when the stimulation frequencies in the range of 60 Hz to 90 Hz (Figure 4.10). Nevertheless, the beetles showed a distinct different in response to left and right stimulation. The right 3Ax muscle could give smooth and clearly graded response of the turning curve (Figure 4.10a), as well as induce more force with clearly graded fashion (Figure 4.10b). These results would suggest that these beetles preferred to turn right as it might have a "handedness" behavior like human [98-100].
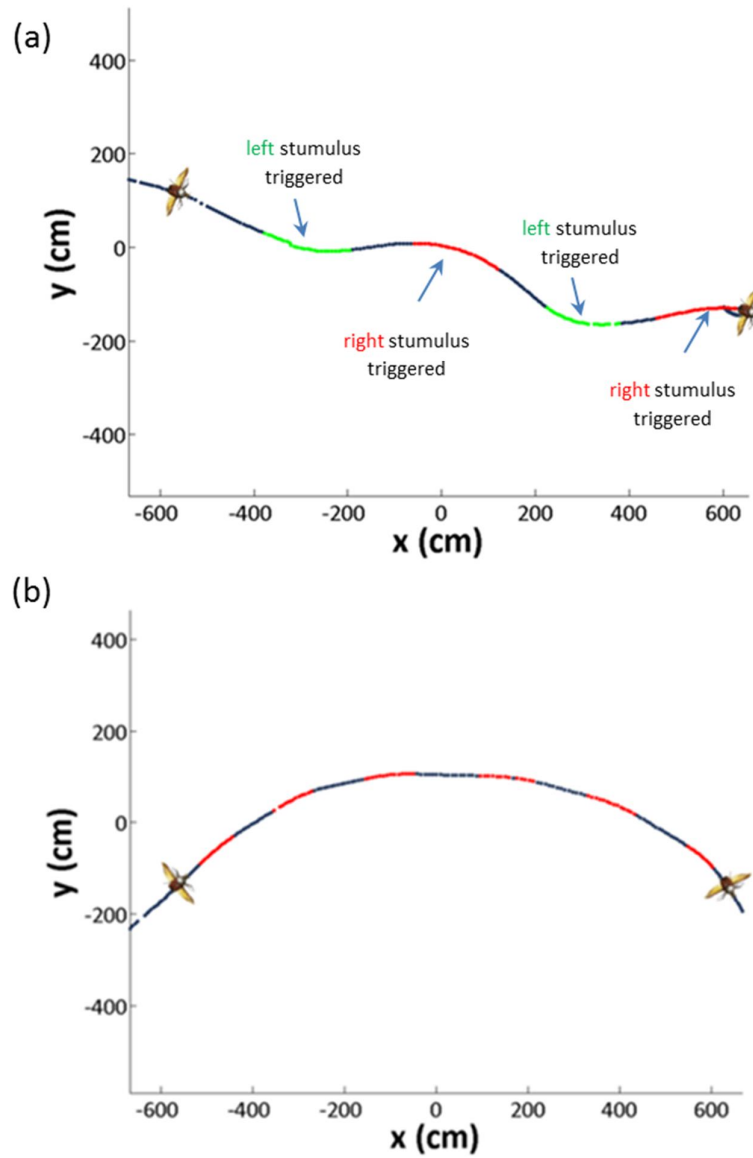
Figure 4.9. Electrical stimulation of 3Ax muscle in free flight.

(a) The left and right 3Ax muscles were stimulated in sequence to produce left and right turn, respectively. (b) The big curve obtained when only right 3Ax muscle was stimulated. The black trajectory segments indicate no stimulation periods; red and green trajectory segments indicate right and left stimulation periods, respectively.
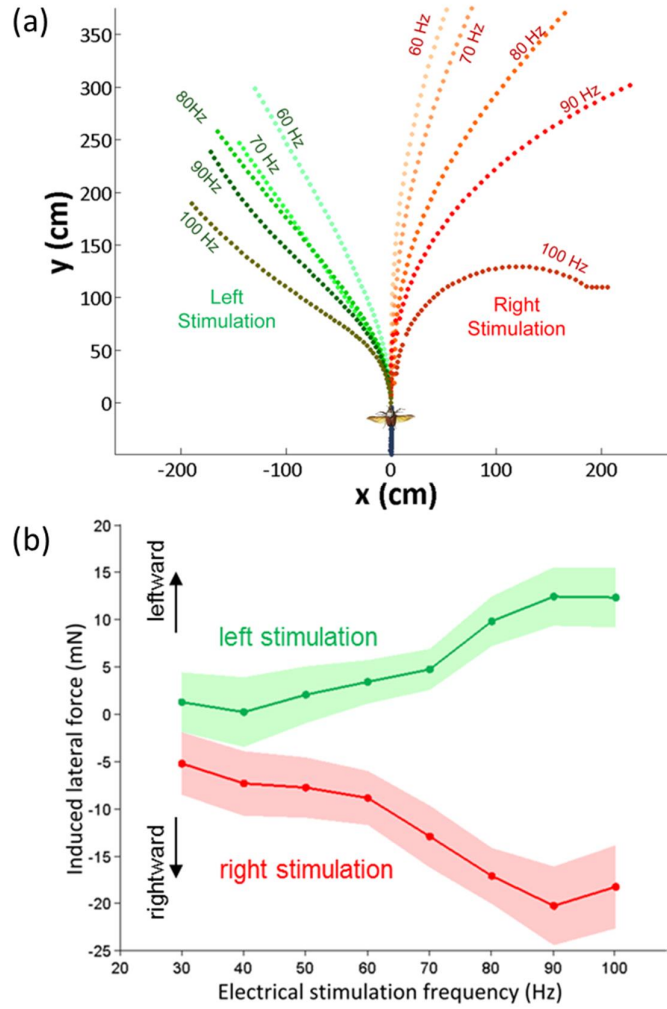
Figure 4.10. Graded response of beetle in free flight.

(a) Stacked stimulated flight paths of various frequencies (b) The electrical stimulation of 3Ax muscle induced lateral force (F_l) which graded as a function of stimulus frequency. The shaded regions denote 95% confidence interval. Positive value of F_l indicates that the force points toward the left and negative value obtained when the force points toward the right (N_{left} = 10 betles, n_{left} = 810 trials, N_{right} = 12 beetles, n_{right} = 758 trials).

4.6: Discussions and Conclusions

It is interesting to investigate the similarity in function between the coleopteran 3Ax muscle and that in other insects. The moths activate the 3Ax muscle during straight flight with certain phase shift as regarding the activation of the dorsal longitudinal muscle during flight maneuvers [93, 97]. In addition, the moth could maintained a certain degree of remotion and elucidated wing retraction by producing the tonic activation of this muscle [93, 97]. In locusts, 3Ax muscles are activated on both sides during straight flight and turns are correlated with both phase shifts from the baseline and changes in spike frequency [19]. On the contrary, in dipterans (notably *Calliphora* and *Eristalis*), the 3Ax has been associated with operating the gear change mechanism when flipping the alula asymmetrically to reduce aerodynamic force, resulting in ipsilateral turning [28, 40, 41, 101]. Besides, the I1 muscle of fly was activated in a weak phasic manner with change of firing rate and also associated with the reduction of stroke amplitude that would induce ipsilateral turn [23]. Although Coleoptera lacks of alula, the 3Ax muscle only tonically contracts on the side ipsilateral to a turn, which is similar to that of dipterans.

By mounting the wireless electrical stimulator onto the freely moving insect, the activation of 3Ax muscle produced left/ right turning of the beetle in free flight. The combination of free flight data and traditional tethered experiment helped to identify the role of 3Ax muscle in beetle. Further investigation of three dimensional wing kinematics induced by 3Ax muscle could explain the details of the muscle function.

Chapter 5 : The function of subalar muscle in braking

5.1: Introduction

Insect aerial maneuver has drawn the interest of scientists for hundred years starting with the studies on wing morphology and flight muscle anatomy to recording and stimulating the insect neuromuscular system. Although it has a long history, the insect flight study has just become more vibrant for two recent decades. It covers free flight experiments from measuring electromyography of different flight muscles [9, 10, 53, 86, 102-106] to controlling motor actions and behaviors of the insects in air using miniature wireless communication devices [46, 50, 54, 87, 107, 108]. While insect walking control is straight forward and shows not only simple directional control [102, 109, 110] but also the implementation of the close-loop system for the complex trajectory control [109, 111], the flight control is still limited to flight initiation, cessation [11, 46] and left-right turning [11, 46, 108, 112] which is not enough to understand the flight maneuver of the insect. Chapter 4 shows the implementation of the miniature wireless stimulator (backpack) in validating the function of the 3AX muscle [108] shown as a promising approach to explore the functions of the remaining flight muscles in order to reveal the function of the small muscle in flight.

Although subalar muscle is well known in insect, its roll in flight control is still a mystery as the muscle was presented in morphology study that drew some speculations based on the physical connection and articulation of the wing base. In this study, we will combine the wing kinematics recording in tethered condition to predict the function of the subalar muscle in beetle and the electrical stimulation of the muscle in free flight to verify that function. The muscle is really used to change the angle of attack that would increase the drag and thus cause the deceleration in free flight.

5.2:   The Function of Subalar Muscle

The subalar muscle in Coleopteran is inserted from the hind leg coxa to the apodema of subalar sclerite [94, 113, 114]. The subalar muscle is next to the basalar muscle and at the posterior of the thorax (Figure 3.1). As the subalar sclerite is located at the posterior of the wing base, it pulls the posterior part of the wing down when the muscle contracts. In locust, the subalar muscle is described to have the function of wing depressor and antagonized pronator [115]. While the subalar muscle of the hindwing is used solely for powering the downstroke, that of the forewing is used for control the level of pronating motion induced by basalar muscle [19, 115]. In moth, the subalar muscle is also used for depressing and supinating the wing which causes the increment of angle of attack of the wing and its drag [53, 93, 97, 116]. In fly, the subalar muscle was believed to have the function of extending and depressing the wing [117]. Meanwhile, the subalar muscle of beetle has been described to have the function of wing extension from since early of 19th century [94] and regulating the angle of attack of the wing [13, 114] even though it is asynchronous muscle. However, the function of subalar muscle was drawn based on the physical connection of the muscle and the arrangement of the subalar sclerite on the wing base without the relation of muscle activity and flight behavior even in tethered condition. Although the electromyogram of subalar muscle was recorded, it was used as wing beat cycle mark without further analysis in locust and moth because of its phasic property [19, 93, 97]. In this study, the correlation of subalar muscle activity and the wing kinematics is investigated in detail in tethered condition to reveal its function and verify the function in free flight experiment. The combination of tethered and free flight experiment would lead to interesting result of insect behavior.

5.3:   The Activation of Subalar Muscle under Visual Stimulation

The fictive upward motion in the beetle flight was associated with the increment of the wing rotation angle in both sides and the positive phase shift of the wing rotation angle (Figure 5.1). The subalar muscle continuously fires in beetle flight (Figure 5.2a). The firing rate during the upward stimulation was higher than that of downward and no stimulation (Figure 5.2b) (N=4, n=35 trials) ($p<0.05$). The activation of subalar muscle was evaluated by associating the electromyogram and the wing kinematics recorded during the visual up/down stimulation in tethered.

The up/down moving of the visual patterns caused consistent responses that make the beetle change the wing kinematics to track the optic flow (N=4, n=35 trials). A high speed motion tracking system (1500 fps) was used to record the wing motion while the beetle responded to the visual stimulus. The firing rate at the subalar muscle increased during the visually induced upward motion (Figure5.2b) (N=4, n=35trials) ($p<0.05$).
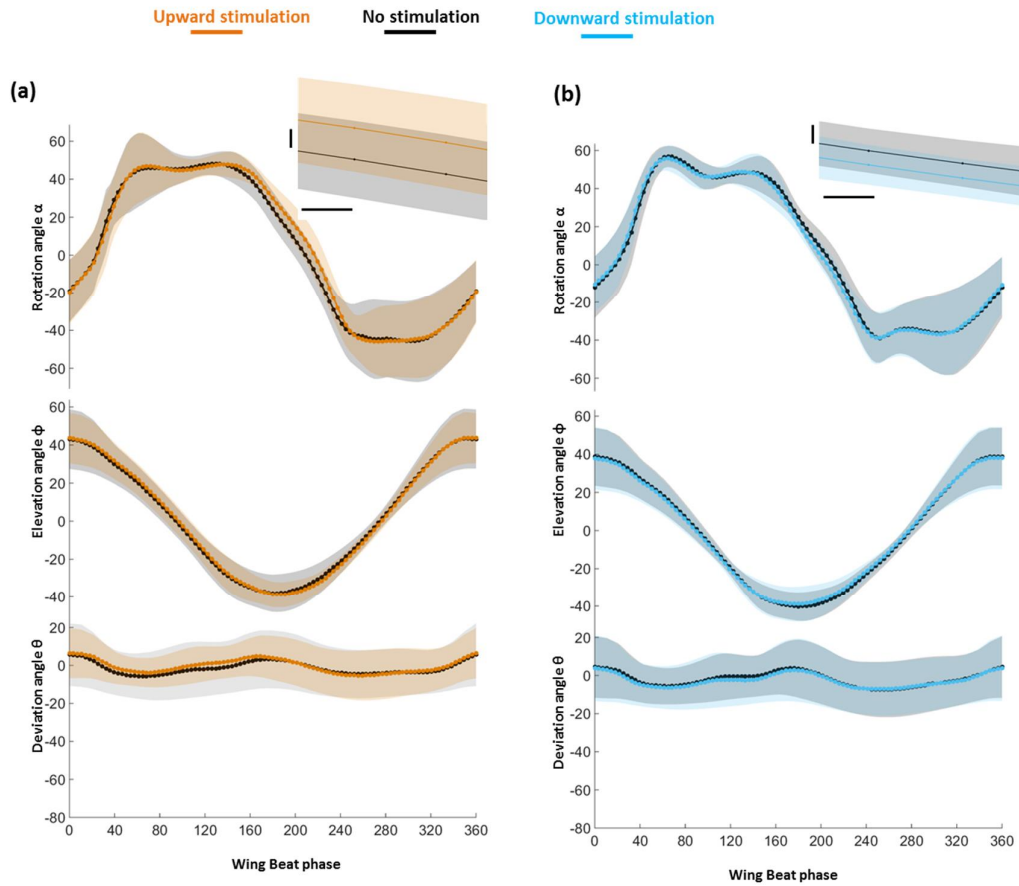
Figure 5.1. Response of beetle to the visual stimulation.

(a) The upward stimulation induced a positive phase shift with an increment of around 10 degrees ($p < 0.05$) in wing rotation angle from 0.4 to 0.6 of wing cycle (upper trace) while the elevation angle (middle trace) and deviation angle (lowest trace) remained ($p > 0.05$). **(b)** The beetle did not show any change of wing kinematics during the downward stimulation as there was no change in wing rotation angle (upper trace), elevation angle (middle trace) and deviation angle (lowest trace) ($p > 0.05$). The insert is the magnification of the wing rotation angle at the phase that shows highest change (N=4, n=35 trials). The scale bars for the wing angle and wing beat phase insert are 5 degree and 2.5 degree, respectively.

The correlation between firing timing at the subalar muscle and the wing beat phase (Figure 2b) is statistically not significant ($p > 0.1$). It suggests that there is slight preferred activation phase for the firing of the subalar muscle (N=4, n=35 trials). Such a tonic activation of the beetle subalar muscle is in contrast to the phasic subalar muscle in moths [53, 93] and locusts [19, 115] and b1 muscle in flies [20, 23], but similar to 3Ax muscle in beetle [108], III1 and I1 muscle in fly [23].

The contraction of subalar muscle pulls the subalar sclerite, which is located at the posterior part of the wing base, and thus it depresses the trailing edge of the wing and increases the wing rotation angle [94, 114]. In fact, during the upward visual stimulation, which resulted in the enhanced activation of the subalar muscle (Figure 5.2b upper trace), the rotational angle increased, and vice versa (Figure 5.1a and b upper traces) (N=4, n=35 trials) ($p < 0.05$). This alteration in the wing rotation angle during flight should increase the drag and the lift of the wing [118] that lead to the decrease and increase in the accelerations in the horizontal and in the vertical directions, respectively.
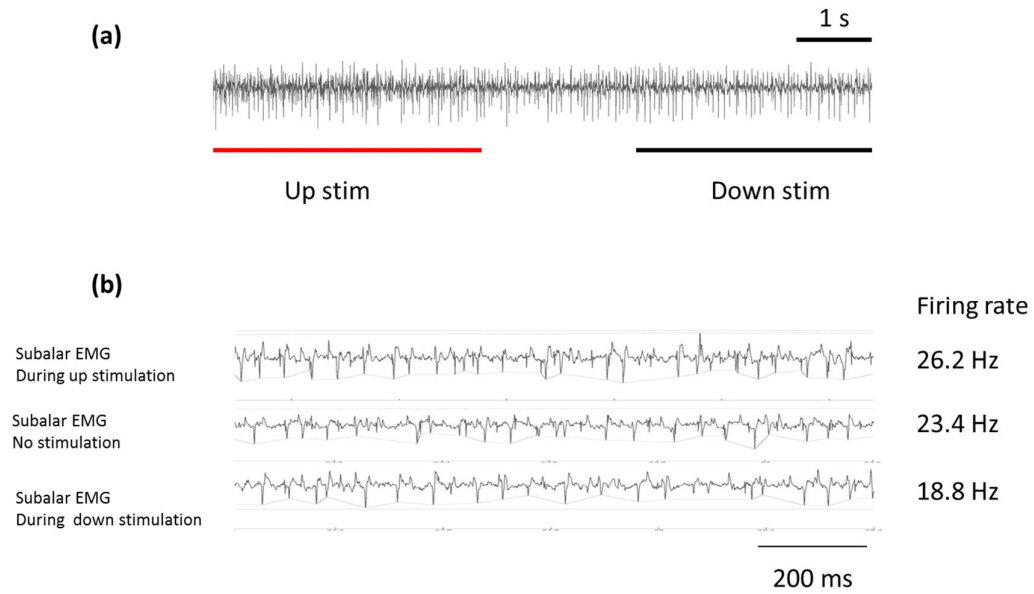
Figure 5.2. Electromyography of the beetle during the visual stimulation.

(a) The subalar muscle always fired during the beetle flight. **(b)** It showed highest activity during the upward stimulation with the firing rate of 26.2 Hz and decreased to 23.4 Hz and 18.8 Hz (p<0.05)during the no stimulation period and down ward stimulation respectively (N=4, n=35 trials).
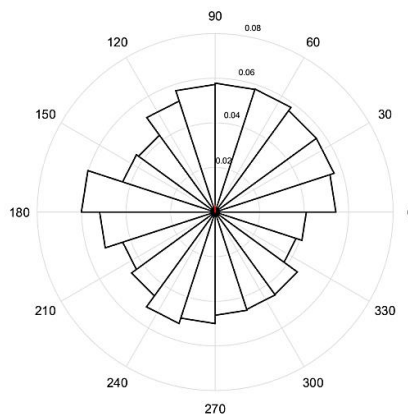
Figure 5.3. Electromyogram spikes distribution was mapped on the wing beat phase (N=4, n=35 trials).

5.4:   The Response of Wing Kinematics due to Electrical Stimulation of Subalar Muscle

The electrical stimulation of the subalar muscle shows that the wing rotation angle inclined during the stimulation with the effective range from 70 Hz with no clear frequency-dependency observed (Figure 5.4). The electrical stimulation also caused the increment 5 degrees in wing rotation angle with the effective range from 70 Hz to 100Hz ($p < 0.05$) (N=4, n=160 trials) that is associated with the low variation of EMG firing rate increment during upward stimulation (Figure 5.2). Based on the increment of wing rotation angle during the visual stimulation and electrical stimulation, it can be seen that subalar muscle is used for changing the wing rotation angle in flight. Moreover, the subalar muscle is expected to adjust the wing rotation angle for quick response without fine tune by increasing the firing rate as there is no clear correlation of muscle firing rate with the amount of wing rotation angle increasing (Figure 5.2b). The increment of wing rotation angle induced additional drag that decelerated the beetle flight.
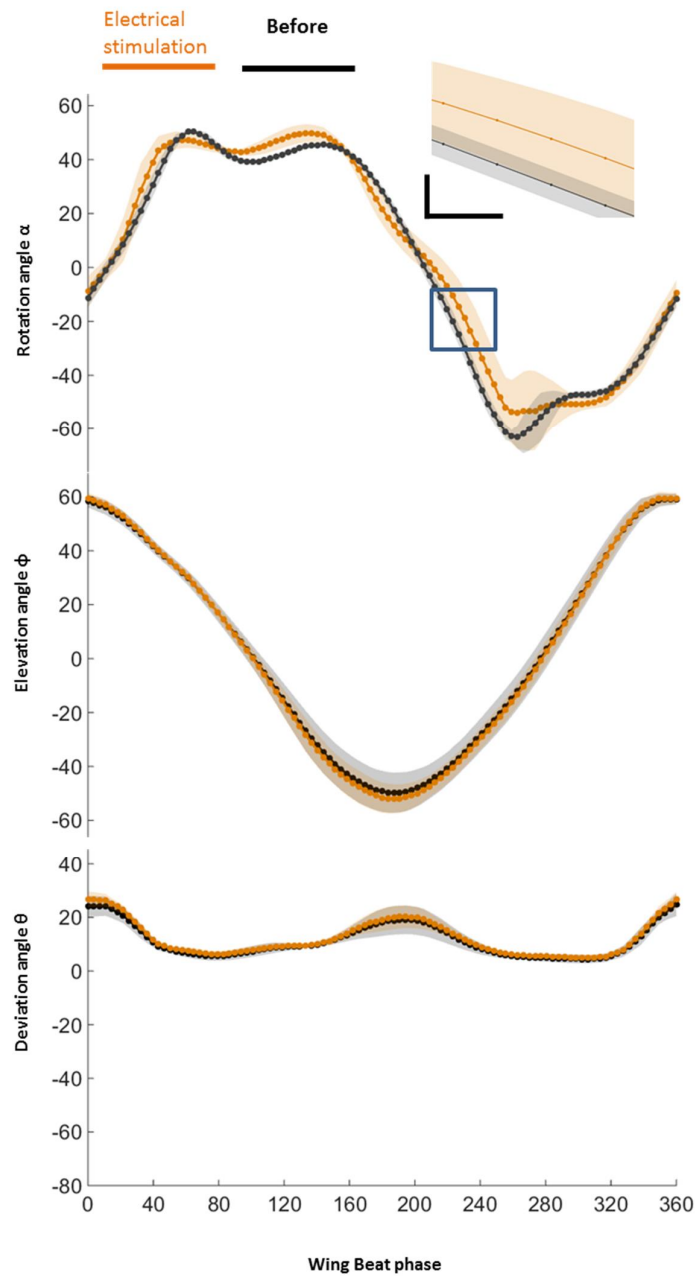
Figure 5.4. Response of beetle to the electrical stimulation. The beetle showed a slight phase shift during the first 0.2 of wing cycle and a clear positive phase shift with the increment of 5 degrees (p<0.05) in wing rotation angle from 0.4 to 0.7 wing cycle (N=4, n=168 trials). The scale bars for the wing angle and wing beat phase insert are 10 degree and 5 degree, respectively

5.5:   The Response of Beetle due to Electrical Stimlation of Subalar Muscle in Free Flight

The stimulation of subalar muscles induced additional drag to the beetle with an effective stimulation range started from 70 Hz (Figure 5.5a) (N=14, n=2800 trials) with slight frequency dependency as the induced horizontal force did not shift clearly but just fluctuated around -10mN ($p < 0.01$). In addition, the stimulation of subalar muscle leads to a relatively small enhancement in the lift as the induced vertical force was around 5mN ($p < 0.05$) from 70 Hz to 80Hz dropped to 1 mN at 90 Hz and 100 Hz ($p > 0.05$) (Figure 5.5b). Besides, the stimulation of subalar muscle did not affect the turning in the beetle flight as the induced lateral force is around zero ($p > 0.05$) (Figure 5.5c), which should be because the both left and right subalar muscles were stimulated equally. In addition, the stimulation of subalar muscle did not affect the nearby muscles as shown in Figure 5.6.
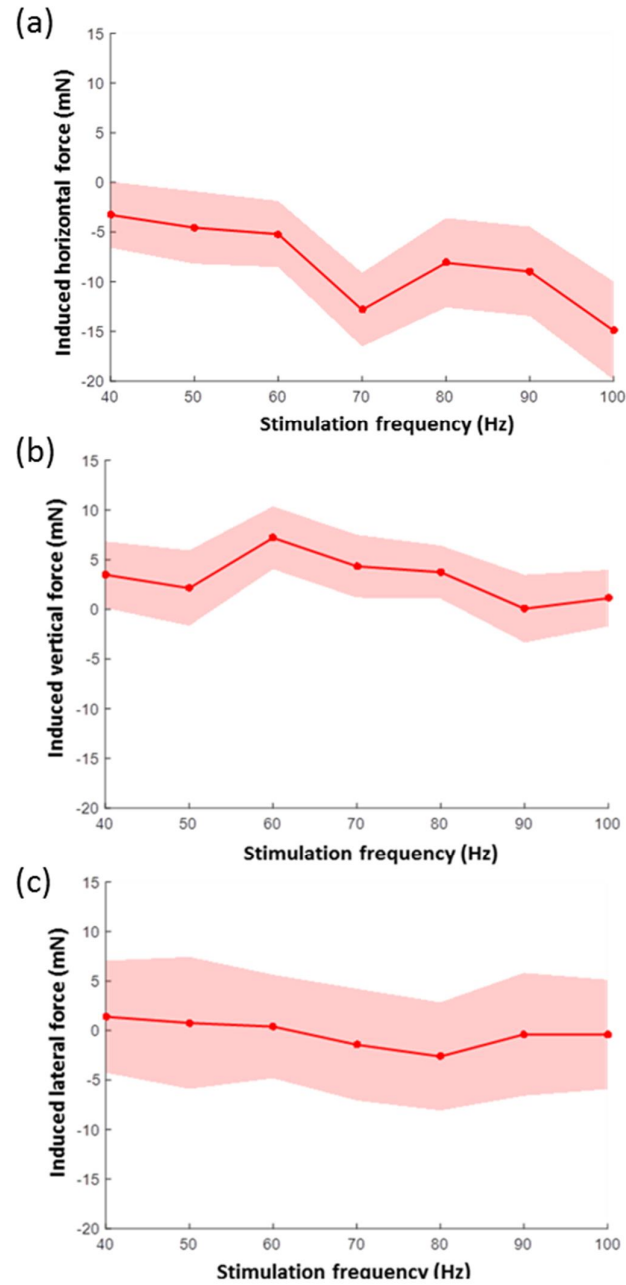
Figure 5.5. Free flight behavior of the beetle due to electrical stimulation. **(a)** The horizontal force of the beetle decreased around 5 mN from 40 Hz to 60 Hz and fluctuated around 10 mN from 70 Hz. **(b)** The induced vertical force was kept positive during the stimulation. **(c)** The induced lateral force of the beetle fluctuated around 0 mN. The shaded region indicated 95% confidence interval.

EMG of Basalar Muscle

EMG of 3rd Ax Muscle

EMG of Remote
Extensoris Muscle
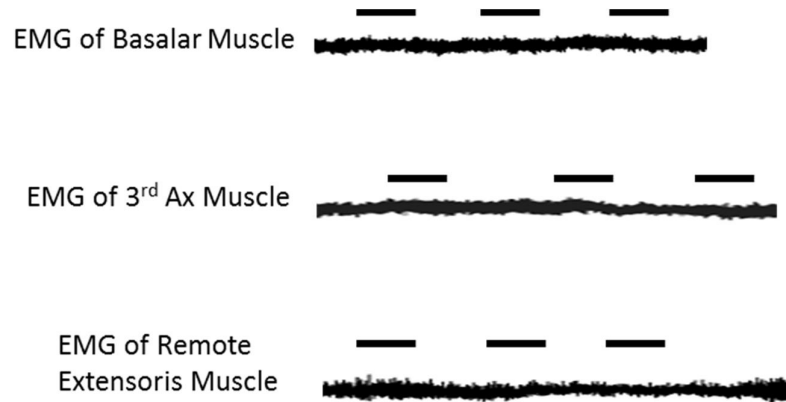
Figure 5.6. EMG of nearby muscles during the electrical stimulation of subalar muscle. No EMG spike was observed in the nearby muscles while stimulating subalar muscles (N = 3, n=60 trials). The solid bars indicate the stimulation periods.

5.6: Discussions and Conclusions

The combination of wireless stimulation in free flight and the traditional tethered experiment of insect behavior study enables the investigation of the real function of insect flight muscle and reveals the mystery of insect complex flight mechanism. This is the first time that subalar muscle is investigated in detail from the tethered to free flight. The subalar muscle has the function of alternating the wing rotation angle, which leads to the increment of the drag and thus decelerates the flight speed. The achievement in braking control of the beetle in free flight opens a new realm for insect flight control targeting more complex flight maneuver such as hovering. However, such behavior might evolve multiple muscles [119-121], which is a challenge for controlling the maneuver of the insect. Further investigation in the effect of multiple muscles would be carried out and their activation timing would provide clearer picture of insect flight mechanism. As the system is not able to eliminate the insect own intention to control its muscular system, the feedback of EMG for activation state of the muscle would help to

improve the insect maneuver control [122, 123]. The appropriate stimulation parameters

and protocol can be provided to compensate for the insect self-control.

Chapter 6 : B-doped Pd catalyst for oxygen reduction reaction

6.1: Introduction

The oxygen reduction reaction (ORR) plays an important role in fuel cell as oxygen is a common fuel for cathodic reduction. However, the very strong O=O bond make ORR non-facile [124-129]. Although many efforts have been expended on cathode material, developing highly active oxygen electrode catalyst at low cost is still a challenge. The so-called *volcano curve* established by Nørskov and co-workers shows the relation of the oxygen reduction activity of different metals and alloys to the binding energy of atomic oxygen [127-131]. Based on these curved, the pure metals Pt and Pd exhibit superior catalytic activities for oxygen reduction, which can be further improved by alloying them with other elements to weaken the oxygen binding strength. This notion has been confirmed by the enhanced ORR activity of Pt_3M alloys (M = Ni, Co, Fe, V, Ti, Sc, Y) in which the *d*-band centre of Pt atoms is lower than that of pure Pt [128-131]. Pt-alternative catalysts have also been researched to maintain the high ORR activity while reducing the cost [76, 132-136]. The activities of Pd-alloy (Pd-Co and Pd-Fe) catalysts are comparable with that of Pt [132, 133, 136]. Despite a recent report on P-doped Pd in the amorphous structure for ORR, much less work has been devoted to doping non-metallic elements into Pd.

In this project, B-doped Pd catalyst is developed by stepwise electroless deposition process. In this method, the electrode is sequentially dipped into two different solutions, the first containing a reducing agent (dimethylaminoborane (DMAB)) and the second containing a metal salt (metal ion source, $PdCl_2$). During the second dipping, Pd nanoparticles are electrochemically deposited onto the electrode surface. The Pd nanoparticles become doped with B atoms released by the decomposition of DMAB (here, the B-doped Pd is denoted as Pd-B).

The Pd-B nanoparticles were synthesized directly to the electrode surface by stepwise electroless deposition that is remarkably fast and facile. Each deposition cycle lasts approximately 30 s and carried out in ambient conditions while the traditional methods are complicated and need hash conditions (high temperature, vacuum). No additive is required to extend the shelf life of the nanoparticles or control the dispersion of the nanoparticles as compared to the casting method that need to synthesize and cast the nanoparticles separately. This eliminates the risk of blocking electron transfers and mass transports that affect the catalytic activity of the Pd nanoparticles when using additives [137-139]. In addition, this stepwise electroless deposition produces less chemical waste. The deposited nanoparticles on the electrode surface are the only product from the reaction that consumes the metal. That is much better than the traditional procedures which generate quite high amount of waste. Moreover, the electroless deposition is superior in loading the nanoparticles as it allows the nanoparticles deposit onto the complex structure. Unlike the traditional methods, where the nanoparticles are usually casted onto the electrode surface or mixed with a carbon paste and spread onto the substrate that can only have simple design, electroless deposition have a capability of depositing the particles onto complex structure that enables the use of more unique substrates.

The Pd-B catalyst was compared with a pure Pd catalyst (no doping) synthesized by same method using hydrazine (N_2H_4) as reducing agent (the synthesized pure Pd is denoted as Pd-N_2H_4) and a commercial Pd-loaded carbon (denoted as Pd/C) for evaluating the effect of B-doping on Pd nanoparticles. The B-doping was confirmed by X-ray diffraction patterns of the catalysts while enhancement in electro catalytic was verified by electrochemical measurement. The B-doping promotes the catalytic activity

of the Pd nanoparticles as the synthesized Pd-B exhibits superior catalytic activity to the Pd-N_2H_4 and Pd/C.

6.2: Experimental Procedure

6.2.1: Stepwise electroless deposition of Pd nanoparticles catalyst

B-doped Pd nanoparticles were synthesized by adopting DMAB, a reducing agent, to our earlier developed stepwise electroless deposition process[140] as described below. 1.5 mL of 0.2 M DMAB and 2 mM $PdCl_2$ solutions were prepared and stored in separate test tubes about 15 minutes before the synthesis. Prior to the deposition process, the surface of a glassy carbon electrode (GC) designed for a rotating disk electrode (RDE) (diameter = 3 mm; Bioanalytical Systems, Inc.) was polished with alumina slurry (0.05 μm), rinsed and ultrasonically cleaned in DI water for 5 minutes. The electrode was then air-blown to dry its surface and mounted to the holder of a custom designed robot, which automatically conducts the subsequent deposition procedures (stepwise electroless deposition process) according to a user-defined time sequence. In this study, the sequence was set up as in Figure 6.1: (1) the electrode was dipped in the DMAB solution for 10 s, (2) the electrode was air-blown to remove any remaining solution, (3) the electrode was dipped in the $PdCl_2$ solution for 10 s (the DMAB reduces the Pd ions to Pd metals, which are deposited on the GC surface), (4) the electrode was dipped in DI water to terminate the Pd deposition and (5) the electrode was dried by air-blowing. To ensure sufficient Pd-B nanoparticles for the electrochemical evaluation, this sequence was iterated nine times. The GC-RDE catalyst coated with Pd-B nanoparticles was subsequently tested by linear sweep voltammetry (LSV) at different rotational speeds (400–2500 rpm), cyclic voltammetry (CV) and

chronoamperometry, as described later. The pure Pd nanoparticles (Pd-N$_2$H$_4$) were synthesized and examined by the exactly same procedure as the B-doped Pd nanoparticles but with a different reducing agent, N$_2$H$_4$ instead of DMAB.
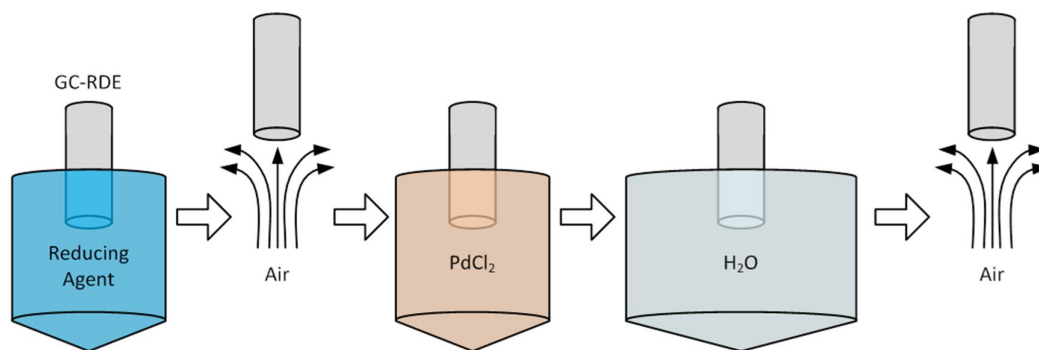
Figure 6.1. Stepwise electroless deposition for Pd nanoparticle synthesis.

6.2.2: Preparation of commercial catalysts Pd/C

The commercial Pd/C (10% Pd, Sigma–Aldrich) catalyst was prepared as reported elsewhere[140, 141]. Briefly, a dispersion of Pd/C in ethanol (0.1 mg$_{Pd}$ / ml) was ultra-sonicated in a beaker and a defined amount (7.5 μL) was cast onto the GC-RDE surface, giving a Pd load of 0.75 μg.

6.2.3: Physical characterization

Field emission scanning electron microscopy images were obtained from a JEOL7600 microscope operated at 5 kV. X-ray diffraction characterization was performed by a PANalytical Empyrean diffractometer equipped with a Cu-Kα radiation source (λ = 1.54060 Å). XPS was obtained at pass energies of 160 eV and 40 eV for wide and detailed scanning, respectively, using a Kratos Axis Ultra spectrometer equipped with monochromatic Al Kα (1486.6 eV).

6.2.4: Electrochemical measurements

All electrochemical measurements were conducted in a 3 cell setup by a potentiostat (Princeton Applied Research VersaSTAT3-200) using an Ag/AgCl (saturated KCl) reference electrode, Pt wire as the counter electrode and desired catalyst coated on the GC-RDE as working electrode. All the Linear sweep voltammetry (LSV) was conducted in O_2-saturated 0.1 M KOH solution at a scan rate of 10 mVs^{-1} and a rotational speed of 400, 900, 1600, 2500 rpm, in a direction of 0.166 V to 0.966 V vs RHE. The cyclic voltammetry (CV) was conducted in N_2-saturated 0.1 M KOH solution at a scan rate of 50 mVs^{-1} with no rotation. The CV was recorded in a range of 0.041 V to 1.266 V vs RHE and repeated for 10 cycles for each sample. The chronoamperometry was conducted in O_2-saturated 0.1 M KOH solution at a potential of -0.3 V vs. Ag/AgCl and a rotational speed of 200 rpm, for 30000 seconds.

6.2.5: Preparation of Inductively Coupled Plasma-Mass Spectrometry (ICP-MS)

After the electrochemical tests, the Pd load on the GC-RDE (Pd-B and Pd-N_2H_4) was determined by air-blowing the GC-RDE surface and casting it with 5 μL of HNO_3 (Sigma-Aldrich) for 5 mins. Next, 4 μL of HNO_3 was extracted and dropped into a plastic tube containing DI water (to a total volume of 500 μL). The sample was then analyzed by ICP-MS (Aligent 7700) with a third-generation He collision–reaction cell that minimizes any interferences. Whether the loaded Pd had completely dissolved into the HNO_3 was then determined by LSV measurements. If true, the LSV curve measured after the HNO_3 treatment would match that of the bare GC.

6.3:   Physical Property of B-doped Pd Nanoparticles

The stepwise electroless deposition process formed well dispersed Pd-B nanoparticles on the GC electrode surface (Figure 6.1). B was actually co-deposited on the Pd nanoparticles during the electroless deposition, as evidenced by the ICP-MS data of the obtained Pd-B nanoparticles with B content = 11.8 ± 0.7 at% and Pd content = 88.2 ± 0.7 at%. The Pd-B nanoparticles are crystalline as the sharp XRD profile shown in Figure 6.2.

100 nm
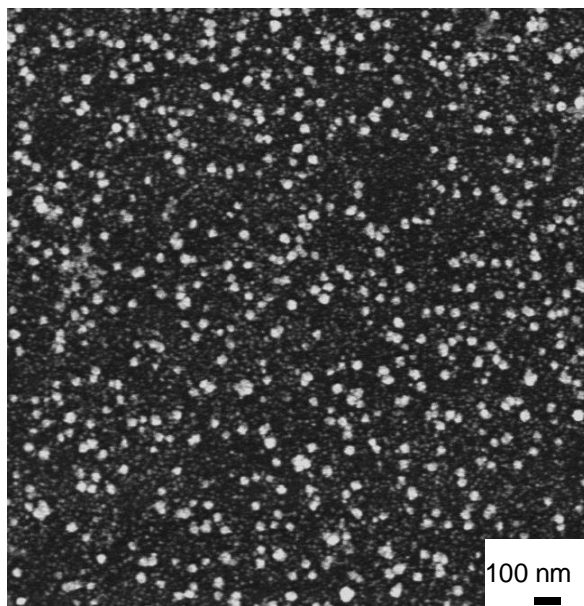
Figure 6.2. Field emission scanning electron microscopy image of Pd-B nanoparticles.

The XRD profile in Figure 6.3 supports the fact that the co-deposited B is indeed embedded in the Pd lattice. Every peak in the Pd-B profile shifts to a lower angle than in the Pd-N_2H_4, Pd/C and pure Pd bulk profiles, suggesting that the Pd lattice has expanded due to the B doping. In addition, the XPS profile shows that Pd-B has low binding energy than pure Pd that would reduce the binding strength of the ORR intermediates and thus increase the reaction rate (Figure 6.4).
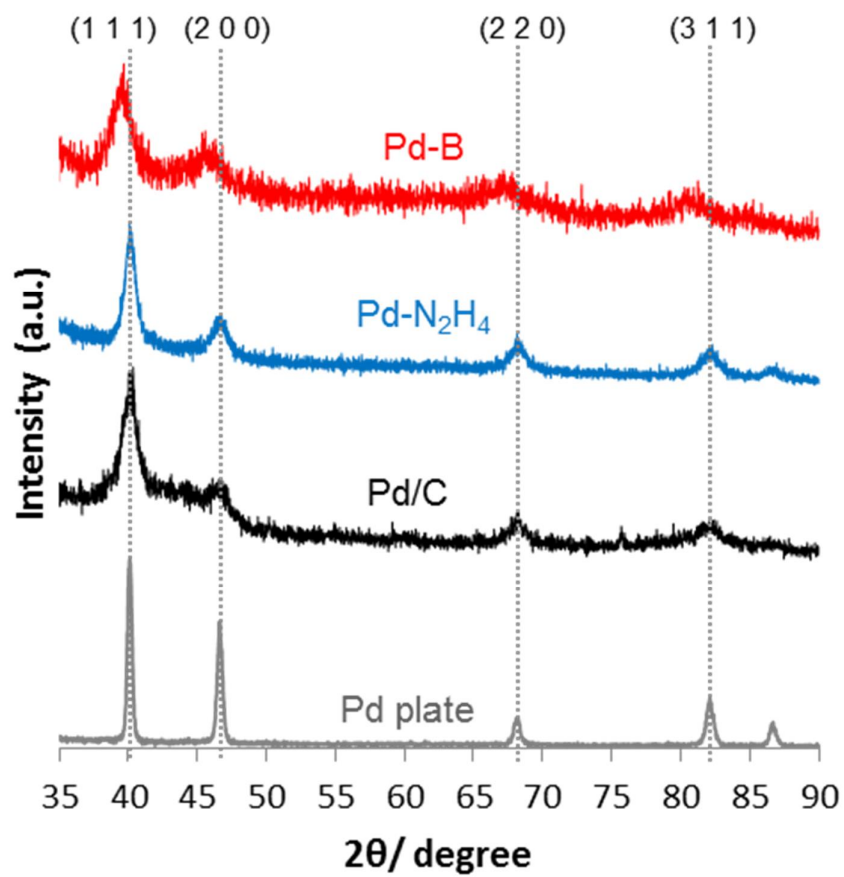
Figure 6.3. X-ray diffraction (XRD) patterns of Pd-B, Pd-N$_2$H$_4$, commercial Pd/C and Pd plate.
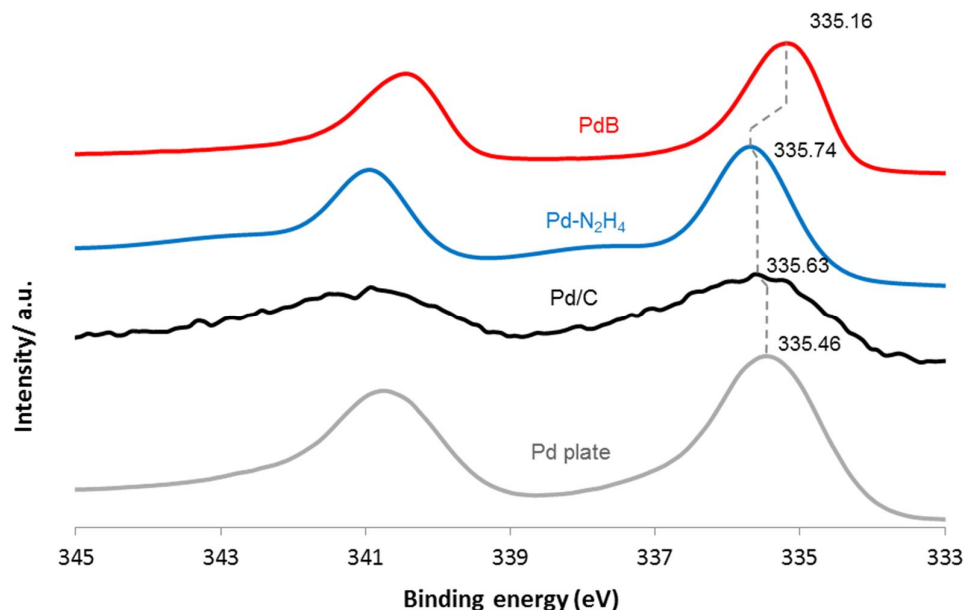
Figure 6.4. X-ray photoelectron spectra (XPS) of Pd-B, Pd-N₂H₄, commercial Pd/C and Pd plate. The calibration for XPS was carried out using C1s binding energy at 284.5 eV [142-144].

6.4: Electrochemical Performance of B-doped Pd Nanoparticles

6.4.1: ORR polarization curves

The synthesized Pd-B nanoparticles catalyst exhibits higher catalytic activity than that of Pd-N₂H₄ and Pd/C as indicated by the positive shift in the ORR polarization curve (Figure 6.5). Such positive shift indicates the increment in the onset potential of the ORR that leads to the earlier rate occurrence. The half-wave potential of the Pd-B catalyst was then compared to the commercial Pd/C and pure Pd synthesized for more detail of the increment in catalytic activity. The superior catalytic activity of Pd-B is confirmed as its positive half-wave potential (0.86 V) is the highest among Pd-N₂H₄ (0.83V) and Pd/C (0.83 V) (Figure 6.5).
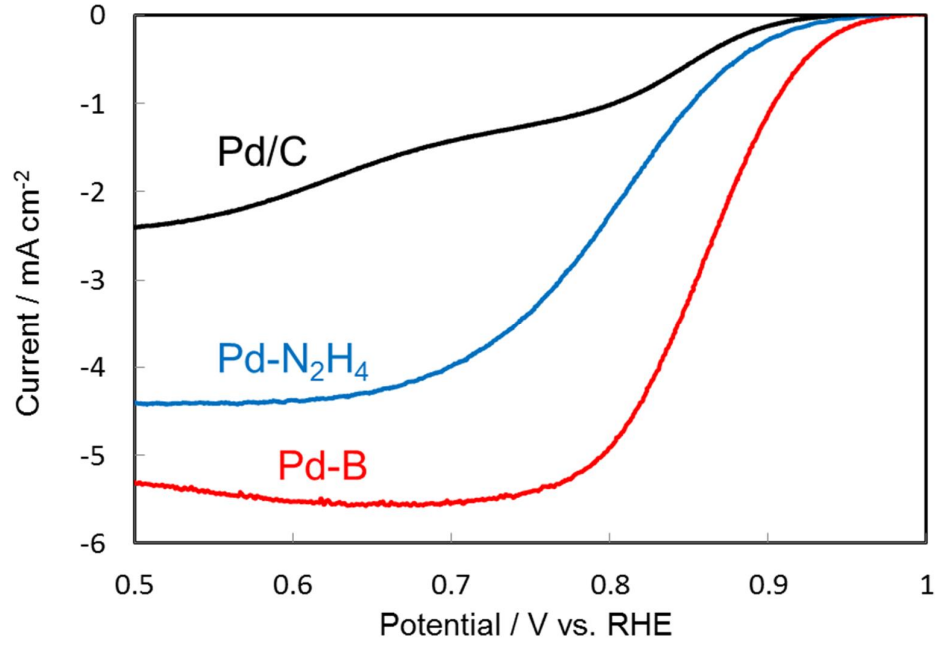
Figure 6.5. ORR polarization curves of Pd-B, Pd-N2H4, and Pd/C. The RDE was measured in 0.1 M O_2-saturated KOH solution at a scan rate of 10 mV s^{-1}. Rotation al speed: 1600 rpm [60, 69, 140].

6.4.2: Specific activity (i_s) and mass activity (i_m)

Although Pd-B has higher half-wave potential than Pd-N$_2$H$_4$ and Pd/C, more accurate assessments based on specific and mass activities (kinetic current (i_k) normalized by ECSA and Pd load, respectively) are required to reflect the catalytic activities of those catalysts. Thus, i_s and i_m of the Pd-B, Pd-N$_2$H$_4$ and Pd/C catalysts are calculated for further analysis.

The kinetic current (i_k) is obtained from the Koutecky–Levich (K-L) equation [145]:

$$- \quad - \quad - \quad - \quad \frac{\quad}{\quad} \tag{1}$$

where ω is the electrode rotational rate (rad/s) and B is the Levich constant, calculated as follows:

$$= 0.62 \quad \text{—} \quad \text{—} \qquad (2)$$

where n is the number of electrons transferred per O_2 molecule, F is the Faraday constant, S is the electrode surface area, c_o and D denote the concentration and diffusion coefficient, respectively, of the dissolved O_2 in the solution and $\quad$ is the kinematic viscosity of the solution. All the constants are listed in Table 6.1.

Table 6.1. Standard values for constants used in K-L equation[146]

Constant	Value
F	96485 $Cmol^{-1}$
S	0.0707 cm^{-2}
Co	1.2 x 10^{-6} $molcm^{-3}$
D	1.9 x 10^{-5} $cm^2 s^{-1}$
	0.01 $cm^2 s^{-1}$

The K-L plots of the catalysts are plotted based on the ORR polarization curves at different rotating speeds which shown in Figures 6.6. The K-L plots were plotted at 0.5 V where the limited current (i_d) is present (maximum and stable current density) (Figures 6.7). The i_d can be defined based on the gradient of the K-L plot (1/B) and the desired rotation speed (1600 rpm). The i value at 0.85 V can be obtained directly from the polarization curve at 1600 rpm. The i_k value can be calculated based on the known i_d and i based from Equation 1.

The ECSA can be obtained from the reduction charge value calculated from the full CV curves of the catalyst in N_2 saturated solution. The reduction charge in Pd is calculated from 0.5 V to 0.9 V which is the know region for the reduction of PdO to Pd as shown

in Figures 6.8. The actual reduction charge (Region 1) is calculated by subtracting the double capacitance discharge (Region 2). Thus, The ECSA of Pd catalyst can be calculated by normalizing the actual reduction charge by the reduction charge of PdO (known to be 405 μC cm^{-2}). Figure 6.6 shows the full CV of the Pd-B, Pd-N_2H_4 and Pd/C catalysts.

The specific activity (i_s) of each catalyst was calculated by normalizing the ik value by the ECSA obtained. As summarized in Table 6.2, the commercial Pd/C has the lowest i_s (1.58 mA cm-2) followed by Pd-N_2H_4 (2.87 mA cm^{-2}). The B-doped Pd particles has the highest i_s value (4.13 mA cm^{-2}) which is over 1.4 times and 2.5 times higher than those of Pd-N_2H_4 and Pd/C, respectively.

The mass activity was defined as the kinetic current normalized by the Pd load and also summarized in Table 6.2. The commercial Pd/C also has the lowest im (0.17 mA μg^{-1}) that is lower than the synthesized pure Pd (1.33 mA μg^{-1}). The highest im was found in Pd-B (2.38 mA μg^{-1}) which is 1.7 times and 14 times higher than those of Pd-N_2H_4 and Pd/C, respectively. Considering the market price of Pd, Pd-B catalyst is more than 14 times less costly compared with the commercial Pd/C. Moreover, the pure Pd (Pd-N_2H_4) synthesized by the proposed stepwise electroless deposition has 1.8 times higher in specific activity and 7.8 times higher in mass activity than the commercial Pd/C. This makes the proposed deposition method a strong candidate to replace the current commercial Pd material for electrocatalyst development.
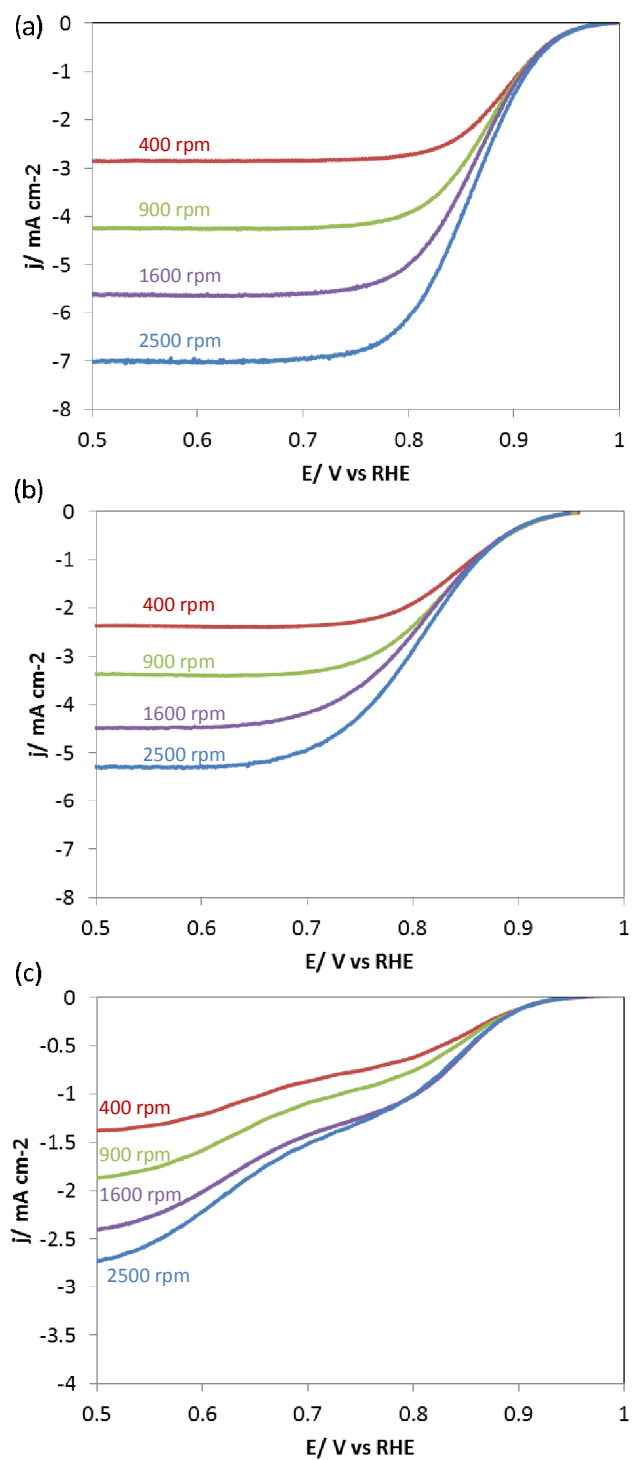
Figure 6.6. ORR polarization curves for Pd-B (a), Pd-N$_2$H$_4$ (b) and Pd/C (c). The ORR measurement was conducted at 400, 900, 1600 and 2500 rpm with scan rate of 10 mVs^{-1}.
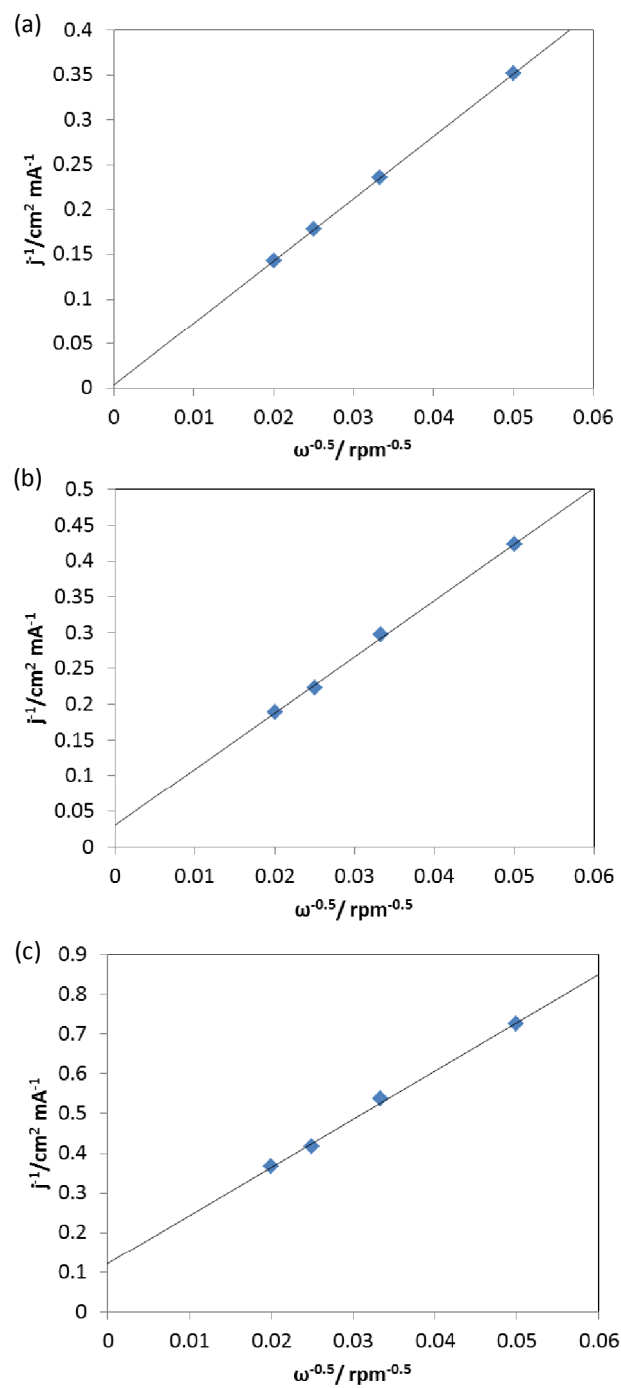
Figure 6.7. K-L plot for Pd-B (a), Pd-N2H4 (b) and Pd/C (c) at 0.6 V.

96
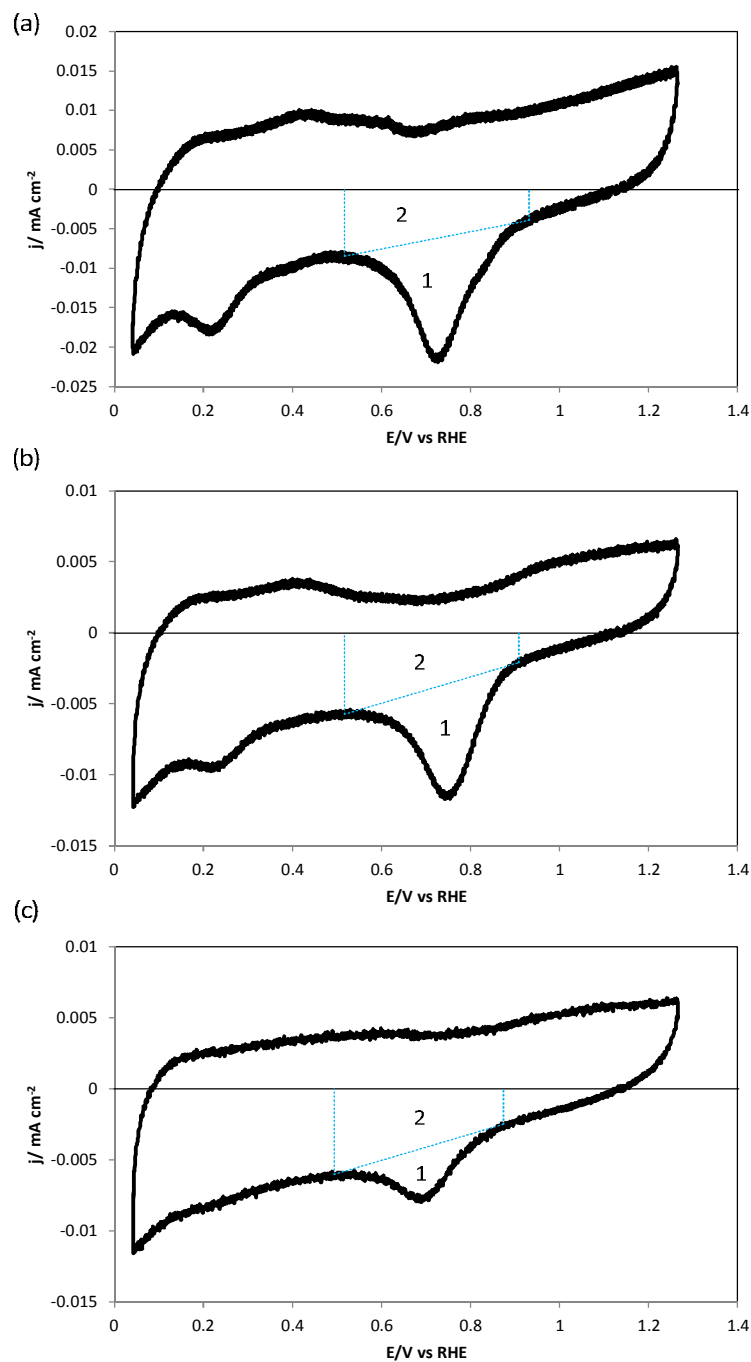
Figure 6.8. Full CV of Pd-B (a), Pd-N$_2$H$_4$ (b) and Pd/C (c) conducted in N2-saturated 0.1 M KOH in the range of 0.04 to 1.27 V vs RHE with a scan rate of 50 mVs^{-1}. Region 1 indicates the actual reduction charge while Region 2 is the double capacitance discharge.

Table 6.2. Half-wave potentials and specific and mass activities of Pd and Pt catalysts[a]

Catalyst	Half-wave potential (V)	Specific activity (mA cm^{-2})	Mass activity (mA µg^{-1})
Pd-B	0.86	4.13	2.38
Pd-N$_2$H$_4$	0.83	2.87	1.33
Pd/C	0.83	1.58	0.17

[a]Specific and mass activities were calculated as described elsewhere. The current was measured at 0.85 V vs. RHE at a rotational speed of 1600 rpm. The values are averaged from several experiments [60, 140].

6.4.3: Durability Test

The high catalytic activity of Pd-B is also maintained over a long time. In the durability test, Pd-B maintained over 75% of its initial catalytic activity, whereas the catalytic activity of Pd-N$_2$H$_4$ and Pd/C rapidly reduced to 53% and 47%, respectively, within 10000 s (Figure 6.9). Therefore, the synthesized pure Pd has higher durability than the commercial Pd and the durability can be enhanced by doping B to the Pd nanoparticles.
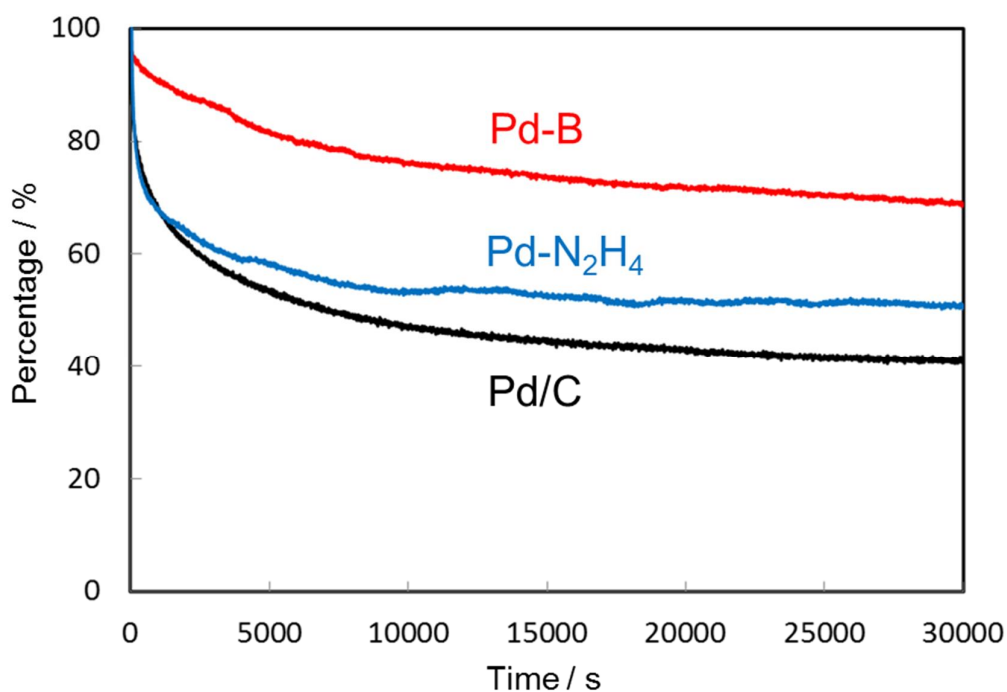
Figure 6.9. Chronoamperometry responses were evaluated as percentage of initial current density. The measurements were performed in 0.1 M O_2-saturated KOH solution at a potential of 0.67 V vs. RHE. Rotational speed: 200 rpm.

6.5:   Discussions and Conclusions

A B-doped Pd catalyst is successfully developed, which not only has superior catalytic activity to undoped Pd catalysts but also exhibits significant enhancement of catalytic activity compared with the commercial Pd/C catalyst. The catalytic activity of B-doped Pd nanoparticles is in the same level of amorphous Pd-P synthesized using the same method [144]. However, the mechanisms for catalytic activity improvement are different. In amorphous Pd-P, the enhancement of catalytic activity should be contributed by the low coordinate sites (defects, kinks, and edges) in amorphous structure [144]. Doping B on the Pd surface does not disorder the crystalline structure of Pd but reduces the binding strengths of the ORR intermediates that caused the

enhancement in ORR activity of the B-doped Pd due to the large site dependence of the binding energy. In terms of the half-wave potential, specific and mass activities and durability, the catalytic activity of the synthesized Pd-B nanoparticles is also superior to the pure Pd and commercial Pd/C.

The stepwise electroless deposition (by which we synthesized Pd-B and Pd-N_2H_4) is remarkably facile, requires no harsh conditions (high temperature and vacuum) and is completed within a short time (less than 5 min in this study). In addition, various pure metal and alloy catalysts with different microstructures can be synthesized by changing the metal ion source and reducing agent. The stepwise electroless deposition is suitable for rational tailoring and design of catalyst materials.

Chapter 7 : Conclusion and Future Works

7.1:   Conclusion

7.1.1: New approach for study insect flight

The flight muscles and its articulations are the key components for insect flight control. The insect itself has a complex metabolic process to convert the chemical energy to drive these muscles and combine their activation for achieving the expected motion of the wing. The traditional approach for study insect flight does not completely reflect the function of the individual muscles. It remains as a barrier to prevent the further development of cyborg flying insect that required more knowledge about the effect of these muscles not only in the tethered condition but also in free flight experiment.

This dissertation presented the new approach for studying the function of the flight muscles was developed by recording and stimulating them in tethered and untethered conditions. While the experiments in tethered conditions help to build the hypothesis of the flight muscle function, the free flight experiment was used for validating such hypothesis. Thus, the new approach helped to define the function of the muscle more precisely. Moreover, this approach would give surprising results when applying on the small flight muscles, which might have little effect on tethered flight but might have a key function in free flight.

7.1.2: Key function of 3Ax muscle and graded left/ right turning in flight

The 3Ax muscle in beetle is well-known to have the function of folding the hind wing and thought to have the key role in wing folding process. However, 3Ax muscle was found to have the key function in flight steering instead of wing folding. The 3Ax muscle was activated in a tetanic manner and lead to the graded

reduction of wing beat amplitude in the ipsilateral turn. As a result, stimulating 3Ax muscles in free flight helped to achieve the first graded turning of the beetle flight which is a significant contribution for insect flight control. The results not only reveal the real function of 3Ax muscle of the beetle but also showed the feasibility of the new approach for studying insect flight.

7.1.3: The function of subalar muscle in braking

The subalar muscle of the beetle connects to the trailing edge of the wing via the subalar sclerite. The function of subalar muscle in flight is still unclear since it was neglected for century. This dissertation showed that subalar muscle the activation of subalar muscle occured when the beetle flight upward and caused the increment in wing rotation angle. Moreover, stimulating the subalar muscle in free flight induced the deceleration in horizontal flight speed or braking behavior in flight. This braking control of beetle flight would open a new realm of insect flight control when more controllable insect platforms such as moth and bee are used. More complicated insect flight maneuvers (hovering, landing) would be then succeeded.

7.1.4: B-doped Pd nanoparticle catalyst exhibited superior catalytic activity to the pure Pd and commercial Pd/C catalyst.

The stepwise electroless deposition is remarkably facile and fast as compared to the existing methods. The synthesis process is efficient as it produces less waste and has good nanoparticle distribution on the electrode surface. Even the synthesized pure Pd catalyst has higher catalytic activity than the commercial Pd/C.

The Pd-B nanoparticles have higher catalytic activity than pure Pd nanoparticles. The B-doping enhanced the lattice size of the particle and reduced the binding

energy in Pd-B nanoparticles that lead to the higher reaction rate in ORR. Various materials can be used for doping Pd nanoparticles to improve the electrocatalytic activity.

7.2: Future Works

The advantage of current experimental platform provides us a strong tool to develop the insect-machine hybrid system. However, the requirement of fulfill understanding the functions of the individual muscle still remains and cannot be neglected. The combination of the activation of the muscles is needed to completely control the beetle. Lacking the orientation of the beetle in free flight makes it hard to fully control the beetle maneuver. Thus, the following issues are set as recommendation for future works for this study:

- Evaluate the performance of the other flight muscles in both tethered and untethered conditions to obtain their real functions in flight. While the basalar muscle was demonstrated to have the ability to make turn in the contralateral turn [22], the dorso-ventral muscles and dorsal longitudinal muscles were only reported as the power generator for the flapping wings but they might have other functions [14, 16, 95]. Thus, further study of these muscles would help to define their functions more precisely. The target motions will be initiation/cessation of flight, roll, pitch, yaw and hovering maneuver in free flight.

- Improve the hardware or experiment setup to obtain the orientation of the beetle in free flight. The current free flight data of the beetle just includes the positions of the single marker that lacks of the orientations. The increase

in number of markers would provide the orientations of the insect but it would affect the flight when facing the increase in mass and restriction[147]. The implementation of the MEMS gyroscope sensor would be a potential solution [148].

- Construct the aerodynamics and dynamics models of the insect-machine hybrid system. The aerodynamics model will be built based on the kinematics and aerodynamics of the flapping wing recorded when the muscle is stimulated. The free flight data of the stimulation will be used for develop the dynamics model [147]. The controller for the insect-machine hybrid system will then be built based on these models.

- Develop a control protocol for the insect-machine hybrid system based on the stimulation of multiple muscles. This protocol would solve the problem of flight stabilization during the stimulation as well as achieve complicated flight maneuver like hovering.

The development of electrocatalyst using stepwise electroless deposition has significant advancements. However, there are many possibilities to enhance the catalytic activity of the electrocatalyst along with developing the anode side for constructing the complete fuel cell that can be used for insect-machine hybrid system.

- A new catalyst is needed for boosting the oxygen reduction reaction in biofuel. It can be achieved by changing the metal ion source and reducing agent when using the stepwise electroless deposition. A variety of pure metal and alloy catalysts can be synthesized with different microstructures, loading and substrate to improve the catalytic activity. In the other hand,

multicopper oxidases such as enzymes laccase, and bilirubin oxidase can also be embedded to the cathode.

- Boosting the reaction rate at anode would also help to improve the performance of the biofuel cell. Thus, an enzymatic catalyst with high catalytic activity is required for biofuel oxidation (glucose, trehalose) in the anode. While glucose oxidase and NAD^+-dependent glucose dehydrogenase [149, 150] can be used for glucose oxidation, trehalase| glucose oxidase can be used for trehalose fuel [151, 152].

- Combine the cathode and anode for full biofuel cell operation is important as it shows the real performance of the fuel cell. The biofuel inside the living insect will be extract to use as the fuel for operating the prototype biofuel cell [149, 151-153].

- Integrate biofuel cell into the insect-machine hybrid system will enable the self-powering function of the system. The biofuel cell needs to be miniaturized so that the insect can carry. However, miniaturization will reduce the surface area of the electrodes, which is a critical problem in fuel cell [154, 155]. To overcome such problem, the electrode roughness can be increased by modifying its morphology and structure to increase the active surface such as needle array electrode or using the materials with high active surfaces such as multiwall carbon nanotube [151, 155, 156]. Besides, the amount of body fluid (hemolymph) inside the body of the insect is important as it define the lifetime of the biofuel cell. The fuel source for biofuel cell from the beetle would be enough for operating the fuel cell as the beetle size is comparable with the recent living biofuel cell such as cockroach [151,

153], snail[150] and claim[156]. The biofuel content can be improved and recharged by feeding the insect using reach trehalose and glucose food. As the biofuel cell power can be low in the order of 100 µW and voltage around 0.3 to 0.6 V [155, 157], a booster circuit is required for boosting up the voltage to 4V in order to charge the primary battery.

List of Publication

Journal papers

[1] **T.T Vo Doan**, H. Sato, "Insect-Machine Hybrid Robot: Remote Radio Control of a Freely Flying Insect", *Journal of Visualized Experiments*, (2016), (**Q2**, **IF = 1.325**), **In Press**.

[2] **T.T. Vo Doan**[*], J. Wang[*], K. C. Poon, D. C. L. Tan, B. Kehezri, R. D. Webster, H. Su, H. Sato, "Theoretical Modelling and Facile Synthesis of Highly Active B-doped Pd Catalyst for Oxygen Reduction Reaction", *Angewandte Chemie International Edition, 55(24)*, 6842-6847, (2016), (**Q1**, **IF = 11.261, Frontispiece, * equal contribution**).

[3] H. Sato, **T.T. Vo Doan**, S. Kolev, N. A. Huynh, C. Zhang, T. L. Massey, J. van Kleef, K. Ikeda, P. Abbeel, M. M. Maharbiz, "Deciphering the Role of a Coleopteran Steering Muscle via Free Flight Stimulation", *Current Biology, 25(6)*, 798-803, (2015), (**Q1**, **IF = 9.571**).

[4] F.Cao, C. Zhang, **T. T. Vo Doan**, Y. Li, D. H. Sangi, J. S. Koh, N. A. Huynh, M. F. Bin Aziz, H. Y. Choo, K. Ikeda, P. Abbeel, M. M. Maharbiz, H. Sato, "A Biological Micro Actuator: Graded and Closed-Loop Control of Insect Leg Motion by Electrical Stimulation of Muscles", *PLoS ONE, 9(8)*, e105389, (2014), (**Q1**, **IF = 3.234**).

[5] K. C. Poon*, D. C. L. Tan*, **T.T. Vo Doan***, B. Khezri, H. Su, R. D. Webster and H. Sato, "Newly Developed Stepwise Electroless Deposition Enables a Remarkably Facile Synthesis of Highly Active and Stable Amorphous Pd Nanoparticle Electrocatalysts for Oxygen Reduction Reaction", *Journal of the American Chemical Society, 136*(14), 5217, (2014), (**Q1**, **IF = 12.113, * equal contribution**).

International Conferences

[1] **T. T. Vo Doan**, Y. Li, F. Cao, H. Sato, "Cyborg beetle: Thrust control of free flying beetle via a miniature wireless neuromuscular stimulator", *28th IEEE International Conference on Micro Electro Mechanical Systems (MEMS)*, pp. 1048–1050, Estorial, (2015), (**Acceptance Rate = 41 %**).

[2] **T. T. Vo Doan**, S. Kolev, N. A. Huynh, T. L. Massey, P. Abbeel, M. M. Maharbiz, H. Sato, "Insect-machine hybrid system", *35th Annual International Conference of the IEEE in Engineering in Medicine and Biology Society (EMBC)*, pp.2816-2819, Osaka, (2013), (**Invited Talk**).

References

[1] D. J. Pines and F. Bohorquez, "Challenges Facing Future Micro-Air-Vehicle Development," *Journal of Aircraft,* vol. 43, pp. 290-305, 2006 2006.

[2] R. J. Wood, B. Finio, M. Karpelson, K. Ma, N. O. Pérez-Arancibia, P. S. Sreetharan*, et al.*, "Progress on 'pico' air vehicles," *The International Journal of Robotics Research,* vol. 31, pp. 1292-1302, 2012/09/01/ 2012.

[3] T. J. Mueller, *Fixed and Flapping Wing Aerodynamics for Micro Air Vehicle Applications*: AIAA, 2001.

[4] C. P. Ellington, "The novel aerodynamics of insect flight: applications to micro-air vehicles," *Journal of Experimental Biology,* vol. 202, pp. 3439-3448, 1999-12-01 00:00:00 1999.

[5] K. Y. Ma, P. Chirarattananon, S. B. Fuller, and R. J. Wood, "Controlled Flight of a Biologically Inspired, Insect-Scale Robot," *Science,* vol. 340, pp. 603-607, 2013/05/03/ 2013.

[6] T. N. Pornsin-Sirirak, S. W. Lee, H. Nassef, J. Grasmeyer, Y. C. Tai, C. M. Ho*, et al.*, "MEMS wing technology for a battery-powered ornithopter," in *The Thirteenth Annual International Conference on Micro Electro Mechanical Systems, 2000. MEMS 2000*, 2000, pp. 799-804.

[7] R. J. Wood, "Liftoff of a 60mg flapping-wing MAV," in *IEEE/RSJ International Conference on Intelligent Robots and Systems, 2007. IROS 2007*, 2007, pp. 1889-1894.

[8] R. J. Wood, "The First Takeoff of a Biologically Inspired At-Scale Robotic Insect," *IEEE Transactions on Robotics,* vol. 24, pp. 341-347, 2008/04// 2008.

[9] H. Fischer, H. Kautz, and W. Kutsch, "A Radiotelemetric 2-Channel Unit for Transmission of Muscle Potentials During Free Flight of the Desert Locust, Schistocerca Gregaria," *Journal of Neuroscience Methods,* vol. 64, pp. 39-45, 1996.

[10] W. Kutsch, G. Schwarz, H. Fischer, and H. Kautz, "Wireless Transmission of Muscle Potentials During Free Flight of a Locus," *Journal of Experimental Biology,* vol. 185, pp. 367-373, 1993.

[11] M. M. Maharbiz and H. Sato, "Cyborg Beetles," *Scientific American,* vol. 303, pp. 94-99, 2010.

[12] A. Bozkurt, A. Paul, S. Pulla, A. Ramkumar, B. Blossey, J. Ewer*, et al.*, "Microprobe Microsystem Platform Inserted During Early Metamorphosis to Actuate Insect Flight Muscle," in *IEEE 20th International Conference on Micro Electro Mechanical Systems, 2007. MEMS.*, 2007, pp. 405-408.

[13] R. Dudley, *The biomechanics of insect flight: form, function, evolution*: Princeton University Press, 2002.

[14] J. W. S. Pringle, *Insect Flight* vol. 9: Cambridge University Press, 1957.

[15] R. F. Chapman, S. J. Simpson, and A. E. Douglas, *The Insects: Structure and Function*: Cambridge University Press, 2012.

[16] R. E. Snodgrass, *Principles of Insect Morphology*, 1935.

[17] J. A. Miyan and A. W. Ewing, "How Diptera Move Their Wings: A Re-Examination of the Wing Base Articulation and Muscle Systems Concerned

with Flight," *Philosophical Transactions of the Royal Society of London. B, Biological Sciences,* vol. 311, pp. 271-302, 1985.

[18]   M. H. Dickinson and M. S. Tu, "The Function of Dipteran Flight Muscle," *Comparative Biochemistry and Physiology Part A: Physiology,* vol. 116, pp. 223-238, 1997.

[19]   R. Elson and H.-J. Pflüger, "The Activity of a Steering Muscle in Flying Locusts," *Journal of Experimental Biology,* vol. 120, pp. 421-441, 1986.

[20]   M. S. Tu and M. H. Dickinson, "The Control of Wing Kinematics by Two Steering Muscles of the Blowfly (Calliphora Vicina)," *Journal of Comparative Physiology A Sensory Neural and Behavioral Physiology,* vol. 178, pp. 813-830, 1996.

[21]   S. P. Sane and M. H. Dickinson, "The control of flight force by a flapping wing: lift and drag production," *Journal of Experimental Biology,* vol. 204, pp. 2607-2626, 2001.

[22]   A. J. Burton, "Directional Change in a Flying Beetle," *Journal of Experimental Biology,* vol. 54, pp. 575-585, 1971.

[23]   C. N. Balint and M. H. Dickinson, "The Correlation Between Wing Kinematics and Steering Muscle Activity in the Blowfly Calliphora Vicina," *Journal of Experimental Biology,* vol. 204, pp. 4213-4226, 2001.

[24]   S. N. Fry, R. Sayaman, and M. Dickinson, "The Aerodynamics of Free-Flight Maneuvers in Drosophila," *Science,* vol. 300, pp. 495-498, 2003 2003.

[25]   M. H. Dickinson, F. O. Lehmann, and S. P. Sane, "Wing Rotation and the Aerodynamic Basis of Insect Flight," *Science,* 1997 1997.

[26]   R. Wootton, "Aerodynamics: How flies fly," *Nature,* vol. 400, pp. 112-113, 1999.

[27]   A. L. R. Thomas, G. K. Taylor, R. B. Srygley, R. L. Nudds, and R. J. Bomphrey, "Dragonfly flight: free-flight and tethered flow visualizations reveal a diverse array of unsteady lift-generating mechanisms, controlled primarily via angle of attack," *Journal of Experimental Biology,* vol. 207, pp. 4299-4323, 2004/11/15/ 2004.

[28]   S. P. Sane, "The aerodynamics of insect flight," *The Journal of Experimental Biology,* vol. 206, pp. 4191-4208, 2003/12/01/ 2003.

[29]   Z. J. Wang, "Dissecting Insect Flight," *Annual Review of Fluid Mechanics,* vol. 37, pp. 183-210, 2005 2005.

[30]   C. P. Ellington, C. van den Berg, A. P. Willmott, and A. L. R. Thomas, "Leading-edge vortices in insect flight," *Nature,* vol. 384, pp. 626-630, 1996/12/26/ 1996.

[31]   S. N. Fry, R. Sayaman, and M. H. Dickinson, "The aerodynamics of hovering flight in Drosophila," *Journal of Experimental Biology,* vol. 208, pp. 2303-2318, 2005/06/15/ 2005.

[32]   R. J. Bomphrey, N. J. Lawson, N. J. Harding, G. K. Taylor, and A. L. R. Thomas, "The aerodynamics of Manduca sexta: digital particle image velocimetry analysis of the leading-edge vortex," *Journal of Experimental Biology,* vol. 208, pp. 1079-1094, 2005/03/15/ 2005.

[33]   C. N. Balint and M. H. Dickinson, "Neuromuscular control of aerodynamic forces and moments in the blowfly, Calliphora vicina," *Journal of Experimental Biology,* vol. 207, pp. 3813-3838, 2004/10/15/ 2004.

[34]   S. P. Sane and M. H. Dickinson, "The aerodynamic effects of wing rotation and a revised quasi-steady model of flapping flight," *Journal of Experimental Biology,* vol. 205, pp. 1087-1096, 2002/04/15/ 2002.

[35]   A. D. Straw, K. Branson, T. R. Neumann, and M. H. Dickinson, "Multi-camera real-time three-dimensional tracking of multiple flying animals," *Journal of The Royal Society Interface,* vol. 8, pp. 395-409, 2011/03/06/ 2011.

[36]   M. B. Reiser and M. H. Dickinson, "Drosophila fly straight by fixating objects in the face of expanding optic flow," *The Journal of Experimental Biology,* vol. 213, pp. 1771-1781, 2010/05/15/ 2010.

[37]   M. Mronz and F.-O. Lehmann, "The free-flight response of Drosophila to motion of the visual environment," *Journal of Experimental Biology,* vol. 211, pp. 2026-2045, 2008.

[38]   T. Hesselberg and F.-O. Lehmann, "The role of experience in flight behaviour of Drosophila," *Journal of Experimental Biology,* vol. 212, pp. 3377-3386, 2009/10/15/ 2009.

[39]   S. N. Fry, N. Rohrseitz, A. D. Straw, and M. H. Dickinson, "Visual control of flight speed in Drosophila melanogaster," *Journal of Experimental Biology,* vol. 212, pp. 1120-1130, 2009/04/15/ 2009.

[40]   F. v. Breugel and M. H. Dickinson, "The visual control of landing and obstacle avoidance in the fruit fly Drosophila melanogaster," *The Journal of Experimental Biology,* vol. 215, pp. 1783-1798, 2012/06/01/ 2012.

[41]   J. A. Bender and M. H. Dickinson, "Visual stimulation of saccades in magnetically tethered Drosophila," *The Journal of Experimental Biology,* vol. 209, pp. 3170-3182, 2006/08/15/ 2006.

[42]   M. S. Tu and M. H. Dickinson, "The control of wing kinematics by two steering muscles of the blowfly (Calliphora vicina)," *Journal of Comparative Physiology A-neuroethology Sensory Neural and Behavioral Physiology,* vol. 178, pp. 813-830, 1996 1996.

[43]   M. H. Dickinson, "The Initiation and Control of Rapid Flight Maneuvers in Fruit Flies," *Integrative and Comparative Biology,* vol. 45, pp. 274-281, 2005/04/01/ 2005.

[44]   P. T. Weir and M. H. Dickinson, "Flying Drosophila Orient to Sky Polarization," *Current Biology,* vol. 22, pp. 21-27, 2012/01/10/ 2012.

[45]   L. F. Tammero and M. H. Dickinson, "The influence of visual landscape on the free flight behavior of the fruit fly Drosophila melanogaster," 2002 2002.

[46]   H. Sato, C. W. Berry, Y. Peeri, E. Baghoomian, B. E. Casey, G. Lavella*, et al.*, "Remote Radio Control of Insect Flight," *Frontiers in Integrative Neuroscience,* vol. 3, 2009.

[47]   T. Tien Van, B. Doyoung, L. Laura Corley, J. E. Douglas, P. Hoon Cheol, and K. Min Jun, "Flight behavior of the rhinoceros beetle Trypoxylus dichotomus during electrical nerve stimulation," *Bioinspiration & Biomimetics,* vol. 7, p. 036021, 2012.

[48]   W. M. Tsang, A. L. Stone, Z. N. Aldworth, J. G. Hildebrand, T. L. Daniel, A. I. Akinwande*, et al.*, "Flexible Split-Ring Electrode for Insect Flight Biasing Using Multisite Neural Stimulation," *IEEE Transactions on Biomedical Engineering,* vol. 57, pp. 1757-1764, 2010.

[49]   A. Bozkurt, R. Gilmour, D. Stern, and A. Lal, "MEMS based bioelectronic neuromuscular interfaces for insect cyborg flight control," in *Micro Electro Mechanical Systems, 2008. MEMS 2008. IEEE 21st International Conference on*, 2008, pp. 160-163.

[50]   A. J. Hinterwirth, B. Medina, J. Lockey, D. Otten, J. Voldman, J. H. Lang, *et al.*, "Wireless Stimulation of Antennal Muscles in Freely Flying Hawkmoths Leads to Flight Path Changes," *PloS ONE,* vol. 7, 2012.

[51]   H. Sato, C. W. Berry, and M. M. Maharbiz, "Flight control of 10 gram insects by implanted neural stimulators," in *Solid State Sensor Actuator Workshop*, 2008, pp. 90-91.

[52]   S. J. Thomas, R. R. Harrison, A. Leonardo, and M. S. Reynolds, "A Battery-Free Multichannel Digital Neural/EMG Telemetry System for Flying Insects," *IEEE Transactions on Biomedical Circuits and Systems,* vol. 6, pp. 424-436, 2012.

[53]   N. Ando and R. Kanzaki, "Changing Motor Patterns of the 3rd Axillary Muscle Activities Associated with Longitudinal Control in Freely Flying Hawkmoths," *Zoological Science,* vol. 21, pp. 123-130, 2004/02/01 2004.

[54]   A. Bozkurt, R. F. Gilmour, and A. Lal, "Balloon-Assisted Flight of Radio-Controlled Insect Biobots," *IEEE Transactions on Biomedical Engineering,* vol. 56, pp. 2304-2307, 2009.

[55]   X.-Z. Yuan and H. Wang, "PEM Fuel Cell Fundamentals," in *PEM Fuel Cell Electrocatalysts and Catalyst Layers*, J. Zhang, Ed., ed: Springer London, 2008, pp. 1-87.

[56]   C. Song and J. Zhang, "Electrocatalytic Oxygen Reduction Reaction," in *PEM Fuel Cell Electrocatalysts and Catalyst Layers*, J. Zhang, Ed., ed: Springer London, 2008, pp. 89-134.

[57]   A. J. Bard and L. R. Faulkner, *Electrochemical methods: fundamentals and applications* vol. 2: Wiley New York, 1980.

[58]   A. Kongkanand, S. Kuwabata, G. Girishkumar, and P. Kamat, "Single-wall carbon nanotubes supported platinum nanoparticles with improved electrocatalytic activity for oxygen reduction reaction," *Langmuir,* vol. 22, pp. 2392-2396, 2006.

[59]   V. Nallathambi, J.-W. Lee, S. P. Kumaraguru, G. Wu, and B. N. Popov, "Development of high performance carbon composite catalyst for oxygen reduction reaction in PEM proton exchange membrane fuel cells," *Journal of Power Sources,* vol. 183, pp. 34-42, 2008.

[60]   M. H. Seo, S. M. Choi, H. J. Kim, and W. B. Kim, "The graphene-supported Pd and Pt catalysts for highly active oxygen reduction reaction in an alkaline condition," *Electrochemistry Communications,* vol. 13, pp. 182-185, 2// 2011.

[61]   B. Lim, M. Jiang, P. H. Camargo, E. C. Cho, J. Tao, X. Lu, *et al.*, "Pd-Pt bimetallic nanodendrites with high activity for oxygen reduction," *science,* vol. 324, pp. 1302-1305, 2009.

[62]   Z. Chen, D. Higgins, H. Tao, R. S. Hsu, and Z. Chen, "Highly active nitrogen-doped carbon nanotubes for oxygen reduction reaction in fuel cell applications," *The Journal of Physical Chemistry C,* vol. 113, pp. 21008-21013, 2009.

[63] V. Komanicky, H. Iddir, K.-C. Chang, A. Menzel, G. Karapetrov, D. Hennessy*, et al.*, "Shape-dependent activity of platinum array catalyst," *Journal of the American Chemical Society,* vol. 131, pp. 5732-5733, 2009.

[64] N. M. Marković, R. R. Adžić, B. D. Cahan, and E. B. Yeager, "Structural effects in electrocatalysis: oxygen reduction on platinum low index single-crystal surfaces in perchloric acid solutions," *Journal of Electroanalytical Chemistry,* vol. 377, pp. 249-259, 1994/10/31 1994.

[65] C. Wang, H. Daimon, Y. Lee, J. Kim, and S. Sun, "Synthesis of monodisperse Pt nanocubes and their enhanced catalysis for oxygen reduction," *Journal of the American Chemical Society,* vol. 129, pp. 6974-6975, 2007.

[66] N. Elezovic, B. Babic, V. Radmilovic, L. M. Vracar, and N. Krstajic, "Nb–TiO 2 supported platinum nanocatalyst for oxygen reduction reaction in alkaline solutions," *Electrochimica Acta,* vol. 56, pp. 9020-9026, 2011.

[67] M. Oezaslan, F. Hasché, and P. Strasser, "PtCu3, PtCu and Pt3Cu alloy nanoparticle electrocatalysts for oxygen reduction reaction in alkaline and acidic media," *Journal of The Electrochemical Society,* vol. 159, pp. B444-B454, 2012.

[68] Z. Chen, M. Waje, W. Li, and Y. Yan, "Supportless Pt and PtPd Nanotubes as Electrocatalysts for Oxygen-Reduction Reactions," *Angewandte Chemie International Edition,* vol. 46, pp. 4060-4063, 2007.

[69] L. Jiang, A. Hsu, D. Chu, and R. Chen, "Size-Dependent Activity of Palladium Nanoparticles for Oxygen Electroreduction in Alkaline Solutions," *Journal of The Electrochemical Society,* vol. 156, pp. B643-B649, May 1, 2009 2009.

[70] S. Mentus, A. Abu Rabi, and D. Jašin, "Oxygen reduction on potentiodynamically formed Pd/TiO2 composite electrodes," *Electrochimica Acta,* vol. 69, pp. 174-180, 5/1/ 2012.

[71] H. Erikson, A. Sarapuu, N. Alexeyeva, K. Tammeveski, J. Solla-Gullón, and J. M. Feliu, "Electrochemical reduction of oxygen on palladium nanocubes in acid and alkaline solutions," *Electrochimica Acta,* vol. 59, pp. 329-335, 1/1/ 2012.

[72] E. Antolini, "Palladium in fuel cell catalysis," *Energy & Environmental Science,* vol. 2, pp. 915-931, 2009.

[73] A. Budniok and J. Kupka, "The evolution of oxygen on amorphous Ni☐ Co ☐ P alloys," *Electrochimica Acta,* vol. 34, pp. 871-873, 1989.

[74] S. Maheswari, P. Sridhar, and S. Pitchumani, "Pd–TiO 2/C as a methanol tolerant catalyst for oxygen reduction reaction in alkaline medium," *Electrochemistry Communications,* vol. 26, pp. 97-100, 2013.

[75] M. Shao, T. Yu, J. H. Odell, M. Jin, and Y. Xia, "Structural dependence of oxygen reduction reaction on palladium nanocrystals," *Chemical Communications,* vol. 47, pp. 6566-6568, 2011.

[76] L. Xiao, L. Zhuang, Y. Liu, J. Lu, and H. D. Abruña, "Activating Pd by Morphology Tailoring for Oxygen Reduction," *Journal of the American Chemical Society,* vol. 131, pp. 602-608, 2009/01/21 2009.

[77] S. Maheswari, P. Sridhar, and S. Pitchumani, "Pd–TiO2/C as a methanol tolerant catalyst for oxygen reduction reaction in alkaline medium," *Electrochemistry Communications,* vol. 26, pp. 97-100, 1// 2013.

[78] M. Neergat, V. Gunasekar, and R. Rahul, "Carbon-supported Pd–Fe electrocatalysts for oxygen reduction reaction (ORR) and their methanol tolerance," *Journal of Electroanalytical Chemistry,* vol. 658, pp. 25-32, 7/15/ 2011.

[79] J. Podestá and R. Piatti, "Amorphous Pd-P, Au-P and Co-P alloys as cathode materials in alkaline solution for oxygen reduction," *International journal of hydrogen energy,* vol. 22, pp. 753-758, 1997.

[80] P. H. Matter, L. Zhang, and U. S. Ozkan, "The role of nanostructure in nitrogen-containing carbon catalysts for the oxygen reduction reaction," *Journal of Catalysis,* vol. 239, pp. 83-96, 2006.

[81] F. Cheng, Y. Su, J. Liang, Z. Tao, and J. Chen, "MnO2-Based Nanostructures as Catalysts for Electrochemical Oxygen Reduction in Alkaline Media†," *Chemistry of Materials,* vol. 22, pp. 898-905, 2009.

[82] J. Yang and J. J. Xu, "Nanoporous amorphous manganese oxide as electrocatalyst for oxygen reduction in alkaline solutions," *Electrochemistry communications,* vol. 5, pp. 306-311, 2003.

[83] F.-O. Lehmann, "The Limits of Turning Control in Flying Insects," in *Flying Insects and Robots*, D. Floreano, J.-C. Zufferey, M. V. Srinivasan, and C. Ellington, Eds., ed Berlin, Heidelberg: Springer Berlin Heidelberg, 2009, pp. 231-246.

[84] H. C. Ohanian and J. T. Markert, *Physics for Engineers and Scientists: Motion, Force, and Energy, Oscillations, Waves, and Fluids, Temperature, Heat, and Thermodynamics*, 3rd ed.: W. W. Norton, 2007.

[85] M. H. Dickinson, C. T. Farley, R. J. Full, M. A. R. Koehl, R. Kram, and S. Lehman, "How Animals Move: An Integrative View," *Science,* vol. 288, pp. 100-106, 2000.

[86] N. Ando, I. Shimoyama, and R. Kanzaki, "A Dual-Channel FM Transmitter for Acquisition of Flight Muscle Activities from the Freely Flying Hawkmoth, Agrius Convolvuli," *Journal of Neuroscience Methods,* vol. 115, pp. 181-187, 2002.

[87] D. C. Daly, P. P. Mercier, M. Bhardwaj, A. L. Stone, Z. N. Aldworth, T. L. Daniel*, et al.*, "A Pulsed UWB Receiver SoC for Insect Motion Control," *IEEE Journal of Solid-State Circuits,* vol. 45, pp. 153-166, 2010.

[88] J. Krause, A. F. T. Winfield, and J.-L. Deneubourg, "Interactive Robots in Experimental Biology," *Trends in Ecology & Evolution,* vol. 26, pp. 369-375, 2011.

[89] S. P. Sane, A. Dieudonné, M. A. Willis, and T. L. Daniel, "Antennal Mechanosensors Mediate Flight Control in Moths," *Science,* vol. 315, pp. 863-866, 2007.

[90] A. Bozkurt, R. F. Gilmour, A. Sinha, D. Stern, and A. Lal, "Insect–Machine Interface Based Neurocybernetics," *IEEE Transactions on Biomedical Engineering,* vol. 56, pp. 1727-1733, 2009.

[91] N. T. George, T. C. Irving, C. D. Williams, and T. L. Daniel, "The Cross-Bridge Spring: Can Cool Muscles Store Elastic Energy?," *Science,* vol. 340, pp. 1217-1220, 2013.

[92] D. Springthorpe, M. J. Fernández, and T. L. Hedrick, "Neuromuscular control of free-flight yaw turns in the hawkmoth Manduca sexta," *The Journal of Experimental Biology,* vol. 215, pp. 1766-1774, 2012.

[93] M. B. Rheuben and A. E. Kammer, "Structure and Innervation of the Third Axillary Muscle of Manduca Relative to Its Role in Turning Flight," *Journal of Experimental Biology,* vol. 131, pp. 373-402, 1987.

[94] H. Straus-Durckheim, *Considérations générales sur l'Anatomie comparée des animaux articulés: auxquelles on a joint l'anatomie descriptive du Melolontha Vulgaris (Hanneton), donnée comme exemple de l'organisation des Coléoptères* vol. 1: Levrault, 1828.

[95] R. E. Snodgrass, *The Thorax of Insects and the Articulation of the Wings* vol. 36: U.S. Government Printing Office, 1909.

[96] A. J. Burton, "Nervous Control of Flight Orientation in a Beetle," *Nature,* vol. 204, pp. 1333-1333, 1964.

[97] A. E. Kammer, "The Motor Output During Turning Flight in a Hawkmoth, Manduca Sexta," *Journal of Insect Physiology,* vol. 17, pp. 1073-1086, 1971.

[98] C. H. F. Rowell, "Central Control of an Insect Segmental Reflex: I. Inhibition by Different Parts of the Central Nervous System," *Journal of Experimental Biology,* vol. 41, pp. 559-572, 1964/09/01/ 1964.

[99] A. Philippides, N. H. d. Ibarra, O. Riabinina, and T. S. Collett, "Bumblebee calligraphy: the design and control of flight motifs in the learning and return flights of Bombus terrestris," *The Journal of Experimental Biology,* vol. 216, pp. 1093-1104, 2013/03/15/ 2013.

[100] P. F. MacNeilage, "The Evolution of Handedness in Primates," in *Duality and Unity of the Brain*, D. Ottoson, Ed., ed: Springer US, 1987, pp. 100-113.

[101] S. M. Walker, A. L. R. Thomas, and G. K. Taylor, "Operation of the alula as an indicator of gear change in hoverflies," *Journal of The Royal Society Interface,* vol. 9, pp. 1194-1207, 2012.

[102] T. E. Moore, S. B. Crary, D. E. Koditschek, and T. A. Conklin, "Directed locomotion in cockroaches: biobots," *Acta entomologica slovenica,* vol. 6, pp. 71-78, 1998.

[103] H. Fischer and E. Ebert, "Tegula Function During Free Locust Flight in Relation to Motor Pattern, Flight Speed and Aerodynamic Output," *Journal of Experimental Biology,* vol. 202, pp. 711-721, 1999.

[104] P. Mohseni, K. Nagarajan, B. Ziaie, K. Najafi, and S. B. Crary, "An Ultralight Biotelemetry Backpack for Recording EMG Signals in Moths," *IEEE Transactions on Biomedical Engineering,* vol. 48, pp. 734-737, 2001.

[105] W. Kutsch, "Transmission of Muscle Potentials During Free Flight of Locusts," *Computers and Electronics in Agriculture,* vol. 35, pp. 181-199, 2002.

[106] W. Kutsch, S. Berger, and H. Kautz, "Turning Manoeuvres in Free-Flying Locusts: Two-Channel Radio-Telemetric Transmission of Muscle Activity," *Journal of Experimental Zoology Part A: Comparative Experimental Biology,* vol. 299, pp. 139-150, 2003.

[107] W. M. Tsang, A. Stone, Z. Aldworth, D. Otten, A. I. Akinwande, T. Daniel*, et al.*, "Remote control of a cyborg moth using carbon nanotube-enhanced flexible neuroprosthetic probe," in *Micro Electro Mechanical Systems (MEMS), 2010 IEEE 23rd International Conference on*, 2010, pp. 39-42.

[108] H. Sato, Tat T. Vo Doan, S. Kolev, Ngoc A. Huynh, C. Zhang, Travis L. Massey*, et al.*, "Deciphering the Role of a Coleopteran Steering Muscle via Free Flight Stimulation," *Current Biology,* vol. 25, pp. 798-803, 2015.

[109] E. Whitmire, T. Latif, and A. Bozkurt, "Kinect-based system for automated control of terrestrial insect biobots," in *Engineering in Medicine and Biology Society (EMBC), 2013 35th Annual International Conference of the IEEE*, 2013, pp. 1470-1473.

[110] C. Feng, Z. Chao, C. Hao Yu, and H. Sato, "Insect-machine hybrid robot: Insect walking control by sequential electrical stimulation of leg muscles," in *Robotics and Automation (ICRA), 2015 IEEE International Conference on*, 2015, pp. 4576-4582.

[111] F. Cao, C. Zhang, T. T. Vo Doan, Y. Li, D. H. Sangi, J. S. Koh*, et al.*, "A Biological Micro Actuator: Graded and Closed-Loop Control of Insect Leg Motion by Electrical Stimulation of Muscles," *PLoS ONE,* vol. 9, p. e105389, 2014.

[112] H. Sato and M. M. Maharbiz, "Recent developments in the remote radio control of insect flight," *Frontiers in neuroscience,* vol. 4, 2010.

[113] F. Stellwaag, "Der Flugapparat der Lamellicornier," in *Zeitschrift für wissenschaftliche Zoologie*, A. v. K. Karl Theodor Ernst von Seibold, Ernst Heinrich Ehlers, Ed., ed: Wilhelm Engelmann, 1914.

[114] F. W. Darwin and J. W. S. Pringle, "The Physiology of Insect Fibrillar Muscle. I. Anatomy and Innervation of the Basalar Muscle of Lamellicorn Beetles," *Proceedings of the Royal Society of London. Series B. Biological Sciences,* vol. 151, pp. 194-203, 1959.

[115] D. M. WILSON and T. WEIS-FOGH, "Patterned Activity of Co-Ordinated Motor Units, Studied in Flying Locusts," *Journal of Experimental Biology,* vol. 39, pp. 643-667, 1962-12-01 00:00:00 1962.

[116] F. C. Rind, "The Role of an Identified Brain Neurone in Mediating Optomotor Movements in a Moth," *Journal of Experimental Biology,* vol. 102, pp. 273-284, 1983-01-01 00:00:00 1983.

[117] A. Wisser and W. Nachtigall, "Functional-morphological investigations on the flight muscles and their insertion points in the blowfly Calliphora erythrocephala (Insecta, Diptera)," *Zoomorphology,* vol. 104, pp. 188-195, 1984/05/01 1984.

[118] F. T. Muijres, M. J. Elzinga, J. M. Melis, and M. H. Dickinson, "Flies Evade Looming Targets by Executing Rapid Visually Directed Banked Turns," *Science,* vol. 344, pp. 172-177, April 11, 2014 2014.

[119] C. P. Ellington, "The Aerodynamics of Hovering Insect Flight. III. Kinematics," *Philosophical Transactions of the Royal Society of London B: Biological Sciences,* vol. 305, pp. 41-78, 1984-02-24 00:00:00 1984.

[120] A. P. Willmott and C. P. Ellington, "The mechanics of flight in the hawkmoth Manduca sexta. I. Kinematics of hovering and forward flight," *Journal of Experimental Biology,* vol. 200, pp. 2705-2722, 1997-11-01 00:00:00 1997.

[121] M. J. Fernández, D. Springthorpe, and T. L. Hedrick, "Neuromuscular and biomechanical compensation for wing asymmetry in insect hovering flight," *Journal of Experimental Biology,* vol. 215, pp. 3631-3638, 2012-10-15 00:00:00 2012.

[122] N. J. Cowan, M. M. Ankarali, J. P. Dyhr, M. S. Madhav, E. Roth, S. Sefati, *et al.*, "Feedback Control as a Framework for Understanding Tradeoffs in Biology," *Integrative and Comparative Biology,* June 3, 2014 2014.

[123] S. Sponberg and T. L. Daniel, "Abdicating power for control: a precision timing strategy to modulate function of flight power muscles," *Proceedings of the Royal Society of London B: Biological Sciences,* 2012-07-25 08:20:39 2012.

[124] N. M. Marković, T. J. Schmidt, V. Stamenković, and P. N. Ross, "Oxygen Reduction Reaction on Pt and Pt Bimetallic Surfaces: A Selective Review," *Fuel Cells,* vol. 1, pp. 105-116, 2001.

[125] H. A. Gasteiger, S. S. Kocha, B. Sompalli, and F. T. Wagner, "Activity benchmarks and requirements for Pt, Pt-alloy, and non-Pt oxygen reduction catalysts for PEMFCs," *Applied Catalysis B: Environmental,* vol. 56, pp. 9-35, 2005.

[126] A. A. Gewirth and M. S. Thorum, "Electroreduction of Dioxygen for Fuel-Cell Applications: Materials and Challenges," *Inorganic Chemistry,* vol. 49, pp. 3557-3566, 2010/04/19 2010.

[127] J. K. Nørskov, J. Rossmeisl, A. Logadottir, L. Lindqvist, J. R. Kitchin, T. Bligaard, *et al.*, "Origin of the Overpotential for Oxygen Reduction at a Fuel-Cell Cathode," *The Journal of Physical Chemistry B,* vol. 108, pp. 17886-17892, 2004/11/01 2004.

[128] GreeleyJ, I. E. L. Stephens, A. S. Bondarenko, T. P. Johansson, H. A. Hansen, T. F. Jaramillo, *et al.*, "Alloys of platinum and early transition metals as oxygen reduction electrocatalysts," *Nature Chemistry,* vol. 1, pp. 552-556, 10//print 2009.

[129] V. R. Stamenkovic, B. S. Mun, M. Arenz, K. J. J. Mayrhofer, C. A. Lucas, G. Wang, *et al.*, "Trends in electrocatalysis on extended and nanoscale Pt-bimetallic alloy surfaces," *Nature Materials,* vol. 6, pp. 241-247, 03//print 2007.

[130] V. Stamenkovic, B. S. Mun, K. J. J. Mayrhofer, P. N. Ross, N. M. Markovic, J. Rossmeisl, *et al.*, "Changing the Activity of Electrocatalysts for Oxygen Reduction by Tuning the Surface Electronic Structure," *Angewandte Chemie International Edition,* vol. 45, pp. 2897-2901, 2006.

[131] V. R. Stamenkovic, B. Fowler, B. S. Mun, G. Wang, P. N. Ross, C. A. Lucas, *et al.*, "Improved Oxygen Reduction Activity on Pt3Ni(111) via Increased Surface Site Availability," *Science,* vol. 315, pp. 493-497, January 26, 2007 2007.

[132] Y. Suo, L. Zhuang, and J. Lu, "First-Principles Considerations in the Design of Pd-Alloy Catalysts for Oxygen Reduction," *Angewandte Chemie International Edition,* vol. 46, pp. 2862-2864, 2007.

[133] M. Shao, P. Liu, J. Zhang, and R. Adzic, "Origin of Enhanced Activity in Palladium Alloy Electrocatalysts for Oxygen Reduction Reaction†," *The Journal of Physical Chemistry B,* vol. 111, pp. 6772-6775, 2007/06/01 2007.

[134] Y. Liang, Y. Li, H. Wang, J. Zhou, J. Wang, T. Regier, *et al.*, "Co3O4 nanocrystals on graphene as a synergistic catalyst for oxygen reduction reaction," *Nature Materials,* vol. 10, pp. 780-786, 2011.

[135] Y. Li, W. Zhou, H. Wang, L. Xie, Y. Liang, F. Wei*, et al.*, "An oxygen reduction electrocatalyst based on carbon nanotube-graphene complexes," *Nature Nanotechnology,* vol. 7, pp. 394-400, 2012.

[136] J. L. Fernández, D. A. Walsh, and A. J. Bard, "Thermodynamic guidelines for the design of bimetallic catalysts for oxygen electroreduction and rapid screening by scanning electrochemical microscopy. M−Co (M: Pd, Ag, Au)," *Journal of the American Chemical Society,* vol. 127, pp. 357-365, 2005/01/01 2005.

[137] T. E. Springer, T. A. Zawodzinski, and S. Gottesfeld, "Polymer Electrolyte Fuel Cell Model," *Journal of The Electrochemical Society,* vol. 138, pp. 2334-2342, August 1, 1991 1991.

[138] Y. Lee, A. Loew, and S. Sun, "Surface- and Structure-Dependent Catalytic Activity of Au Nanoparticles for Oxygen Reduction Reaction," *Chemistry of Materials,* vol. 22, pp. 755-761, 2010/02/09 2010.

[139] D. Li, C. Wang, D. Tripkovic, S. Sun, N. M. Markovic, and V. R. Stamenkovic, "Surfactant Removal for Colloidal Nanoparticles from Solution Synthesis: The Effect on Catalytic Performance," *ACS Catalysis,* vol. 2, pp. 1358-1362, 2012/07/06 2012.

[140] K. C. Poon, D. C. L. Tan, T. T. Vo Doan, B. Khezri, H. Su, R. D. Webster*, et al.*, "Newly Developed Stepwise Electroless Deposition Enables a Remarkably Facile Synthesis of Highly Active and Stable Amorphous Pd Nanoparticle Electrocatalysts for Oxygen Reduction Reaction," *Journal of the American Chemical Society,* vol. 136, pp. 5217-5220, 2014/04/09 2014.

[141] L. Qu, Y. Liu, J.-B. Baek, and L. Dai, "Nitrogen-Doped Graphene as Efficient Metal-Free Electrocatalyst for Oxygen Reduction in Fuel Cells," *ACS Nano,* vol. 4, pp. 1321-1326, 2010/03/23 2010.

[142] J. C. Bertolini, P. Delichere, B. C. Khanra, J. Massardier, C. Noupa, and B. Tardy, "Electronic properties of supported Pd aggregates in relation with their reactivity for 1,3-butadiene hydrogenation," *Catalysis Letters,* vol. 6, pp. 215-223, 1990/03/01 1990.

[143] K. Noack, H. Zbinden, and R. Schlögl, "Identification of the state of palladium in various hydrogenation catalysts by XPS," *Catalysis Letters,* vol. 4, pp. 145-155, 1990/03/01 1990.

[144] W. Zhou, M. Li, O. L. Ding, S. H. Chan, L. Zhang, and Y. Xue, "Pd particle size effects on oxygen electrochemical reduction," *International Journal of Hydrogen Energy,* vol. 39, pp. 6433-6442, 4/15/ 2014.

[145] U. Paulus, T. Schmidt, H. Gasteiger, and R. Behm, "Oxygen reduction on a high-surface area Pt/Vulcan carbon catalyst: a thin-film rotating ring-disk electrode study," *Journal of Electroanalytical Chemistry,* vol. 495, pp. 134-145, 2001.

[146] S. Guo, S. Zhang, L. Wu, and S. Sun, "Co/CoO Nanoparticles Assembled on Graphene for Electrochemical Reduction of Oxygen," *Angewandte Chemie International Edition,* vol. 51, pp. 11770-11773, 2012.

[147] M. Mischiati, H.-T. Lin, P. Herold, E. Imler, R. Olberg, and A. Leonardo, "Internal models direct dragonfly interception steering," *Nature,* vol. 517, pp. 333-338, 01/15/print 2015.

[148] R. R. Harrison, R. J. Kier, A. Leonardo, H. Fotowat, R. Chan, and F. Gabbiani, "A wireless neural/EMG telemetry system for freely moving

insects," in *Proceedings of 2010 IEEE International Symposium on Circuits and Systems*, 2010, pp. 2940-2943.

[149] T. Miyake, K. Haneda, N. Nagai, Y. Yatagawa, H. Onami, S. Yoshino*, et al.*, "Enzymatic biofuel cells designed for direct power generation from biofluids in living organisms," *Energy & Environmental Science,* vol. 4, pp. 5008-5012, 2011.

[150] L. Halámková, J. Halámek, V. Bocharova, A. Szczupak, L. Alfonta, and E. Katz, "Implanted Biofuel Cell Operating in a Living Snail," *Journal of the American Chemical Society,* vol. 134, pp. 5040-5043, 2012/03/21 2012.

[151] M. Rasmussen, R. E. Ritzmann, I. Lee, A. J. Pollack, and D. Scherson, "An Implantable Biofuel Cell for a Live Insect," *Journal of the American Chemical Society,* vol. 134, pp. 1458-1460, 2012/01/25 2012.

[152] K. Shoji, Y. Akiyama, M. Suzuki, T. Hoshino, N. Nakamura, H. Ohno*, et al.*, "Insect biofuel cells using trehalose included in insect hemolymph leading to an insect-mountable biofuel cell," *Biomedical Microdevices,* vol. 14, pp. 1063-1068, 2012.

[153] K. Shoji, M. Suzuki, Y. Akiyama, T. Hoshino, N. Nakamura, H. Ohno*, et al.*, "Biofuel cells with trehalose leading to an insect-implanted power source," in *2011 16th International Solid-State Sensors, Actuators and Microsystems Conference*, 2011, pp. 2762-2765.

[154] A. Heller, "Miniature biofuel cells," *Physical Chemistry Chemical Physics,* vol. 6, pp. 209-216, 2004.

[155] E. Katz and K. MacVittie, "Implanted biofuel cells operating in vivo - methods, applications and perspectives - feature article," *Energy & Environmental Science,* vol. 6, pp. 2791-2803, 2013.

[156] A. Szczupak, J. Halamek, L. Halamkova, V. Bocharova, L. Alfonta, and E. Katz, "Living battery - biofuel cells operating in vivo in clams," *Energy & Environmental Science,* vol. 5, pp. 8891-8895, 2012.

[157] K. Shoji, Y. Akiyama, M. Suzuki, N. Nakamura, H. Ohno, and K. Morishima, "Biofuel cell backpacked insect and its application to wireless sensing," *Biosensors and Bioelectronics,* vol. 78, pp. 390-395, 4/15/ 2016.